The Dissertation Committee for Alexander Gary Fay certifies that this is the approved version of the following dissertation:

Characterization of Sources of Radioargon in a Research Reactor

Committee:

Steven Biegalski, Supervisor

Derek Haas

Sheldon Landsberger

Joshua Peterson

Erich Schneider

Characterization of Sources of Radioargon in a Research Reactor

by

Alexander Gary Fay, B.S.; M.S.E.

Dissertation

Presented to the Faculty of the Graduate School of

The University of Texas at Austin

in Partial Fulfillment

of the Requirements

for the Degree of

Doctor of Philosophy

The University of Texas at Austin

May 2014

Dedication

For my family.

Acknowledgements

The author would like to acknowledge Dr. Steven Biegalski for his invaluable guidance and support throughout this project, the members of the Dissertation Committee for their time and input, and the staff of the Nuclear Engineering Teaching Laboratory at the University of Texas at Austin.

The author would like to acknowledge the assistance of former University of Texas at Austin colleagues who all made tangible contributions to the progress of this research: Kenneth Dayman, James Armstrong, Robert Flanagan, Franziska Klingberg, Joseph Graham, and Christopher van der Hoeven.

The author would also like to acknowledge the persistent support of colleagues in the Office of Nonproliferation Research and Development at the National Nuclear Security Administration.

The author gratefully acknowledges the NOAA Air Resources Laboratory for the provision of the HYSPLIT transport and dispersion model, along with Los Alamos National Laboratory for the provision of the Monte Carlo N-Particle radiation transport model, both of which were used in this publication.

This research was performed, in part, under appointment to the U.S. Department of Energy Nuclear Nonproliferation International Safeguards Graduate Fellowship Program sponsored by the National Nuclear Security Administration's Office of Nonproliferation and International Security.

Characterization of Sources of Radioargon in a Research Reactor

Alexander Gary Fay, Ph.D.

The University of Texas at Austin, 2014

Supervisor: Steven Biegalski

On Site Inspection is the final measure for verifying compliance of Member States with the Comprehensive Nuclear-Test-Ban Treaty. In order to enable the use of ^{37}Ar as a radiotracer for On Site Inspection, the sources of radioargon background must be characterized and quantified. A radiation transport model of the University of Texas at Austin Nuclear Engineering Teaching Laboratory (NETL) TRIGA reactor was developed to simulate the neutron flux in various regions of the reactor. An activation and depletion code was written to calculate production of ^{37}Ar in the facility based on the results of the radiation transport model.

Results showed ^{37}Ar production rates of $(6.567 \pm 0.31) \times 10^2$ Bq·kWh^{-1} in the reactor pool and the air-filled irradiation facilities, and $(5.811 \pm 0.40) \times 10^4$ Bq·kWh^{-1} in the biological shield. Although ^{40}Ca activation in the biological shield was found to dominate the total radioargon inventory, the contribution to the effluent release rate would be diminished by the immobility of Ar generated in the concrete matrix

and the long diffusion path of mobile radioargon. Diffusion of radioargon out of the reactor pool was found to limit the release rate but would not significantly affect the integrated release activity. The integrated ^{37}Ar release for an 8 hour operation at 950 kW was calculated to be (1.05$\pm$0.8)$\times$10^{7} Bq, with pool emissions continuing for days and biological shield emissions continuing for tens of days following the operation.

Sensitivity analyses showed that estimates for the time-dependent concentrations of ^{37}Ar in the NETL TRIGA could be made with the calculated buildup coefficients or through analytical solution of the activation equations for only (n, γ) reactions in stable argon or (n, α) reactions in ^{40}Ca. Analyses also indicated that, for a generalized system, the integrated thermal flux can be used to calculate the buildup due to air activation and the integrated fast flux can be used to calculate the buildup due to calcium activation.

Based on the results of the NETL TRIGA, an estimate of the global research reactor source term for ^{37}Ar and an estimate of ground-level ^{37}Ar concentrations near a facility were produced.

Table of Contents

List of Figures

List of Tables

1 | Introduction

The Comprehensive Nuclear-Test-Ban Treaty (CTBT), signed in 1996 and awaiting entry into force, is the most recent in a line of treaties to curtail the testing of nuclear weapons by the nuclear weapons states [1]. Test ban treaties like the Limited Test Ban Treaty (LTBT) and Threshold Test Ban Treaty (TTBT) have narrowed the list of acceptable test environments to one venue: underground test sites. Arms control agreements like the Strategic Arms Limitation Treaties and Strategic Arms Reduction Treaties have significantly reduced the global stockpile. Non-weapons states have even concluded their own agreements to abstain from the development or acquisition of weapons or related technology. Often lost among the myriad political and diplomatic challenges that have been overcome to advance the state of arms control are the developments in verification and monitoring capabilities that are necessary to support test bans and arms control agreements. The ability or inability of states to verify proposed agreements has played a significant role in the history of arms control.

As the United States and Soviet Union achieved increasing yields in the atmospheric testing of their thermonuclear weapons, concern about the health effects of the cumulative fallout motivated the international community to prod the superpowers to discontinue testing. The objections from the international community emerged in 1955 but were initially fruitless as a result of disagreement between the United States and Soviet Union about the role of disarmament in a weapon testing treaty and the perceived capacity of each country to verify a test ban treaty.

When the two countries, along with the United Kingdom, finally entered formal negotiations for a nuclear weapon test ban treaty the global and public opposition to testing resulted in a protracted process. Negotiations started in mid-July of 1963 and concluded only 10 days later. The Limited Test Ban Treaty (LTBT, also known as the Partial Nuclear Test Ban Treaty or the Test Ban Treaty of 1963) was signed by the "Original Parties" on 5 August 1963 and opened for international signature shortly thereafter. The treaty was ratified in the United States in September 1963 and entered into force in October 1963.

Much of the debate about the viability of a test ban treaty (prior to the formal LTBT negotiations in July 1963) centered on the necessity of a dedicated system of verification. Initially the USSR believed that neither they nor the US would be able to keep secret any type of weapons test and that bilateral monitoring, neutral monitoring, or global detection stations were unnecessary. The US and UK both believed that a treaty without verification would be a "mirage" and subsequent multilateral meetings explored the scale of monitoring necessary to adequately verify a comprehensive test ban.

Reliable verification required not only the exchange of sensitive national security information by both sides but also the development of new technologies and techniques to assure compliance. Discussions included the role of on-site inspection to verify that a seismic event was nuclear in nature, however the US and USSR disagreed on the necessary frequency of such inspections. Rather than allow verification to stand as a roadblock to the treaty as a whole, the countries agreed to exclude underground testing from the treaty and relegate verification to "national technical means," the independent capabilities of each state rather than a mutually developed regime. Although the significance of verification in the conclusion of a test ban treaty was never formalized in the LTBT text, the political prologue to the

first test ban illustrated the difficulty of verifying such a treaty [2].

The next verification challenge came in the form of the dual treaties of 1974: the Threshold Test Ban Treaty (TTBT) and the Peaceful Nuclear Explosions Treaty (PNET). Both the US and USSR maintained interest in pursuing a comprehensive nuclear test ban to fill the gap left by the LTBT's lack of restrictions on underground tests. The "threshold" defined in the TTBT prohibits the testing of weapons with yield greater than 150 kT. Although the treaty still left open the possibility of low-yield testing, the 150 kT limit served to both reduce the health effects of fallout from the megaton range testing that had gone on during the 1960s and to symbolize a step away from the development of first strike capable, high-yield weapons. In order to prevent either country from testing above the 150 kT limit under the guise of a "peaceful nuclear explosion," the PNET was negotiated and placed similar yield restrictions on non-military uses of nuclear weapons.

As with the LTBT, the primary verification structure for the TTBT and PNET was expected to be the national technical means of the two countries. In order to facilitate the calculation of weapon yield from seismic data (and not just the presence of the explosion), the verification protocol included exchanges of data, including geological assessments of test sites and yield data of previously detected tests in each country. This data exchange was intended to allow the countries to properly calibrate their seismic data analyses for yield verification of future tests. Concerns from both sides about the sensitivity of such data exchanges left the two treaties signed but unratified, although both countries adhered to the restrictions of the TTBT and PNET. In 1990, sixteen years after the negotiation and signing of the treaties, the US and USSR agreed to a new verification protocol that enabled entry-into-force.

The revised protocol identified the locations at which the US and USSR could

test weapons and the specific verification measures available to both countries. These measures included much of the data exchange originally proposed along with in-country seismic monitoring, in-country hydrodynamic monitoring, and on-site inspections that all expanded the regime beyond national technical means. Much of the revised protocol outlined the procedures and technical capabilities of inspectors in an on-site inspection, including samples to be collected, data to be shared, and equipment to be used. Although it took a decade and a half to develop the verification structure necessary to see US and Soviet ratification of the TTBT and PNET, the process highlighted the role of on-site measurement and inspection as a key verification measure [3].

Despite the technological advancements that occurred from the time of the LTBT, TTBT, and PNET to the initial work on the Comprehensive Nuclear-Test-Ban Treaty (CTBT), verification of a multilateral treaty that included underground testing detection posed a formidable challenge. Doubts about the reliability of a regime capable of verifying the CTBT contributed to the failure of the US to ratify the treaty when it was first sent to the Senate in 1999. In the time since this initial ratification attempt, development and testing of the CTBT verification regime has continued.

The Preparatory Commission for the Comprehensive Nuclear-Test-Ban Treaty Organization (CTBTO) directs research on the portfolio of verification measures that will be employed when the treaty enters into force [1]. The core of this verification regime, the International Monitoring System (IMS), is composed of a number of detection technologies that are designed to detect and locate an underground nuclear explosion.

The seismic network of the IMS will be composed of 170 monitoring stations: 50 primary stations and 120 auxiliary stations. At the time of this publication, 146 of the planned seismic stations were installed and certified [4]. Seismic stations are

ground-level seismometers which can distinguish between the S-waves that travel along the Earth's surface after a seismic event, and the P-waves which travel through the body of the Earth. Comparison of arrival times of each phase to the global array of seismometers enables the location of the source of the seismic signal with respect to both latitude/longitude and depth. Amplitude information, in concert with location data, provides insight on the magnitude of the source of the signal [5].

The hydroacoustic monitoring network will be composed of 11 stations, 10 of which are complete at the time of this publication. The network relies on the waveform energy propagated through the ocean from atmospheric, underwater, or near-ocean underground tests. T-Phase stations consist of seismometers which detect the seismic signal created from the transfer of hydroacoustic energy at the land-sea interface. Hydrophone stations detect acoustic signals directly in the ocean, and are arranged as arrays of individual sensors to give directional information about the signal (similar to seismometer arrays). The relatively long propagation distances of hydroacoustic signals allow for global coverage with a network of only 11 stations [6].

The infrasound monitoring network relies on similar acoustic waveform analysis as the hydroacoustic network. Infrasound stations, however, detect acoustic signals propagating in the atmosphere for the purpose of detecting atmospheric tests. The network, when complete, will consist of 60 stations [7].

Although the waveform technologies have proven to be effective at detecting explosions, they are mostly blind to the nature of the explosion, nuclear or otherwise. It is crucial, then, to include radionuclide monitoring techniques to distinguish large scale non-nuclear events from actual nuclear weapon tests. Radionuclide monitoring stations collect and purify particulate matter and/or xenon samples from bulk air, then measure the activity of radioactive species in the sample. Of the 80 total

radionuclide monitoring stations, only 40 are currently planned have radioxenon monitoring capabilities. Sample collection and measurement is automated at all stations. Data from the stations is sent to the International Data Centre (IDC) where it is gathered and prepared for distribution at the request of the States Parties.

In the case of the detection of an event by the IMS, a member state could request an On Site Inspection (OSI) to characterize the event. In an OSI scenario, a battery of experiments would be conducted at the suspected test site over the course of 60-130 days to gather data that can be used by the States Parties to "establish whether or not a nuclear explosion has been carried out" [4]. In this sense, OSI is the final measure available to verify compliance or non-compliance with the Treaty.

The access to the suspected test site provided by OSI allows various types of environmental sampling which are more intrusive than IMS techniques. Among these sampling techniques is subsurface noble gas collection. The detection of subsurface radioargon would provide strong evidence of a nuclear explosion. The neutron flux of an explosion would activate calcium in soil to produce ^{37}Ar, which could be transported sufficiently close to the surface to be collected during an OSI. Although research has shown this technique to be a promising and potentially important part of the OSI portfolio, work remains to be done to show that ^{37}Ar can be detected with sufficient reliability. Among the issues that must be resolved is that of the ^{37}Ar background. Although there are few ^{37}Ar production pathways and the likelihood of these pathways producing field-measurable concentrations is low, these sources are, for the most part, not thoroughly researched and understood. The research undertaken and described in this document is intended to support the development of ^{37}Ar monitoring as a verification technique for OSI.

1.1 Scope of the Research

To facilitate the use of radioargon in an OSI scenario as a tracer for a nuclear explosion, a complete description of radioargon background sources must be constructed. Natural sources of background, primarily calcium activation in soil by cosmic radiation, have been subject to some research and the global concentration from this mechanism has been estimated. Anthropogenic sources, on the other hand, have received less attention and estimates of the anthropogenic background are coarse. As a result, this work intends to bolster the knowledge and understanding of anthropogenic radioargon sources by achieving the following goals:

1. Model the physics of the various facilities and regions of the University of Texas at Austin NETL TRIGA reactor using a radiation transport code such as MCNP. Validate the model using experimental results produced at the reactor.

2. Characterize contributions to the total radioargon production rate from individual production mechanisms, including activation of air in irradiation facilities and pool water and activation of calcium in reactor materials.

3. Quantify the total release rate of radioargon isotopes from the NETL TRIGA reactor based on the results of Tasks 2 and 3.

4. Determine the sensitivity of the total radioargon emission inventory to variation in the relevant physical and operational parameters. Determine the sensitivity of the results to changes in methodology.

5. To the extent possible, generalize the results to describe radioargon releases from other research reactor facilities.

6. Use an atmospheric transport model such as NOAA's HYSPLIT to model the dispersion of radioargon isotopes from a reactor facility. Identify distances over which the ground-level concentration of ^{37}Ar exceeds the minimum detectable concentration for a ^{37}Ar measurement system.

The primary isotope of interest for OSI measurements, ^{37}Ar, is the focus of this project. The isotopes ^{39}Ar and ^{41}Ar are included in discussions and results to the extent possible.

1.2 Overview

Chapter 1 introduced test ban treaty verification, provided historical and institutional context to the work that was undertaken for this project, and detailed the specific goals guiding the research. Chapter 2 reviews the literature on OSI, radioargon production and detection, and sources of radioargon background. Chapter 3 describes the methodological framework of the research with specific attention paid to relevant computational and mathematical techniques. Chapter 4 describes the efforts to validate the reactor model and other computational tools used in the project, and Chapter 5 presents the results of the individual project tasks. Chapter 6 extends the results to describe general cases. Chapter 7 analyzes the sensitivity of the results to a number of operational and methodological parameters. Chapter 8 provides a condensed summary of the results and offers conclusions and suggestions for future work to strengthen the body of knowledge on radioargon emissions and background. Source code for the reactor model and data processing are provided in the Appendices.

2 | Literature Review

2.1 On Site Inspection

OSI, as part of the verification regime for the CTBT, provides the opportunity for field science at the site of a suspected nuclear weapon test. In an OSI scenario, a battery of experiments would be conducted to acquire data that may be useful to States Parties in determining whether a nuclear explosion occurred. As with the IMS, another branch of CTBT verification, the detection of radioactive noble gas in an OSI scenario can be a strong indication that an underground nuclear explosion (UNE) has taken place.

Early development of OSI techniques for a comprehensive test ban treaty (prior to formal proposal of the CTBT) identified ^{37}Ar as an attractive potential tracer due its abundance as an activation product and to the fact that, unlike the fission product noble gases, the entire ^{37}Ar inventory is produced instantly and simultaneously by the neutron flux of the explosion [8]. Later OSI development (now in the context of the CTBT) acknowledged the usefulness of ^{37}Ar as a tracer due to the low global background and half-life sufficiently long to allow detection following the the slow diffusion process to the surface from a well contained UNE [9]. A thorough discussion of noble gas measurements for CTBT verification estimated the ^{37}Ar background to be on the order of mBq·m^{-3} and dominated by natural sources [10].

Calculations of ^{37}Ar production rates in various geologies as a result of a typical UNE showed that detectable quantities of ^{37}Ar would be produced [11] even in low

calcium environments. This result supported the conclusions originally presented by Carrigan *et al.* [12] which indicate that, even in the case of a well contained UNE at a modest 1 kT yield, barometric pumping in the soil would produce detectable concentrations of surface level ^{37}Ar.

Taken as a whole, the literature provides strong evidence that ^{37}Ar is a viable tracer for detection of an UNE in an OSI scenario however a more comprehensive understanding of ^{37}Ar background is encouraged for the eventual implementation of radioargon field detection and measurement systems.

2.2 Argon as a Reactor Effluent

Early work identified ^{37}Ar as a useful radiotracer for atmospheric studies [13]. Production of radioargon in the troposphere via the ^{36}Ar(n,γ)^{37}Ar reaction was the initial focus of the work. Global monitoring of ^{37}Ar levels was expected to provide information on atmospheric circulation as well the behavior of cosmic radiation. Subsequent results showed fluctuations in ^{37}Ar levels spanning three orders of magnitude and concentrations inconsistent with tropospheric production models, leading to the investigation of additional radioargon production pathways [14]. Measurements given by Loosli *et al.* [14] showed dramatic increases in argon levels at times loosely correlated with announced underground nuclear weapons tests. The venting of ^{37}Ar produced via the ^{40}Ca(n,α)^{37}Ar reaction was suspected as the primary culprit, establishing early evidence of radioargon's viability as a tracer for underground nuclear explosions. It was also noted that, in addition to production by cosmic radiation and underground nuclear explosions, production and release by nuclear reactors could contribute to the highly variable measurements [13].

Initial work to experimentally quantify ^{37}Ar production in reactors, for the pur-

poses of assessing reactor operation's effect on atmospheric mixing research using ^{37}Ar, found that the isotope was produced in sufficient quantities to affect nearby atmospheric measurements, depending on specific reactor design and operation [15]. Annual releases were estimated between 6×10^{9} and 3×10^{11} Bq·yr^{-1} for light water moderated power reactors.

Measurements also found that the observed ^{37}Ar/^{39}Ar concentration ratio in light water reactor samples was inconsistent with values predicted for air activation alone. Neutron interactions with calcium impurities in reactor materials were suggested as an additional production pathway, but a complete picture of radioargon production mechanisms in a reactor was deemed a "matter of conjecture" [15].

Further work supported the claim that ^{40}Ca(n,α)^{37}Ar was a significant production pathway in a reactor environment. In the work by Qaim et al. [16], ^{41}Ar concentrations in were measured for typical high-temperature gas reactor operation and found to be too small (compared to ^{37}Ar concentrations) to be attributed to activation of natural argon alone. Calculations for low cross-section reactions, such as ^{39}K(n,t)^{37}Ar, showed that even the inclusion of these pathways did not predict the observed ^{37}Ar concentrations. Estimates suggested that, neglecting other production mechanisms, Ca impurities in fuel elements, control rods, and moderator on the order of 1 parts per million (ppm) would give ^{37}Ar concentrations on the same order of magnitude as the observations [16]. Diffusion of the radioargon out of the matrix in which it was created was not explicitly included in this estimate.

Work to characterize ^{37}Ar production mechanisms and quantify the total radioargon output was born out of interest in the effect of these radioactive effluents on atmospheric tracer experiments. With advancements in atmospheric transport modeling, research on radioargon effluents stalled and interest in the field has been renewed only recently with the development of radioactive noble gas monitoring

techniques for treaty verification. Importantly for this project, minimal work has been done in the area since the development of modern radiation transport and atmospheric transport software packages, so these tools have not yet been meaningfully employed in the investigation of anthropogenic radioargon sources.

2.3 Natural Sources of Radioargon Background

In addition to the anthropogenic sources of radioargon explored in this project, there are natural, terrestrial production mechanisms that contribute to the global radioargon background. Cosmic ray activation of argon in the air and of calcium in the soil have both been investigated as radioargon production pathways. The large majority of the work has focused on tropospheric production due to the usefulness of ^{37}Ar as a tracer for atmospheric mixing. As a result of the high energy cosmic radiation, the predominant mechanism for ^{37}Ar in the atmosphere is the ^{40}Ar(n,4n)^{37}Ar spallation reaction. Simple activation via ^{36}Ar(n,γ)^{37}Ar accounts for roughly 15% of atmospheric ^{37}Ar production [13]. Measurements found an average background concentration of 1.2 mBq·m^{-3}, although sampling had to contend with large spikes in the concentration due to the venting of underground nuclear weapon tests [14]. The minimum ground level concentration was found to be 0.4 mBq m^{-3}, which "may represent the cosmic ray produced activity found at ground level" without the interference of nuclear facilities or weapons tests [17]. Reactor effluents were identified as the reason for "minor fluctuations" in measurements not otherwise attributable to a specific nuclear explosion.

Research on cosmic ray activation of calcium in soil is more limited. The earliest studies used proxy isotopes, such as ^{22}Na, to estimate the production rate of ^{37}Ar in various rock types [18]. The first measurements of equilibrium concentrations of

^{37}Ar have only been presented very recently [19]. Soil samples from ten international locations were collected, the soil gas was pumped out, argon was purified out of the bulk gas, and the radioargon was measured using an underground internal gas-proportional counter. It was found that the ^{37}Ar concentration for depths less than 1.5 m were commensurate with estimates of ground level atmospheric levels. In an example depth profile taken from one of the samples, the highest soil concentrations were on the order of 10^2 mBq·m^{-3} and were found at depths of 1.5 m - 2.5 m. Concentrations exceeded the theoretical MDC of a field argon measurement system for depths less than 8 m.

Soil activation modeling associated conducted by Riedmann *et al.* [19] showed good agreement with the experimental results, however more geologically rigorous modeling suggests that the inclusion of barometric pumping in the model could appreciably affect the results. Most notably, barometric pumping could shift the depth of peak ^{37}Ar concentration well below the $\sim$2 m range suggested by Riedmann *et al.* [19], effectively reducing the cosmic ray-induced ^{37}Ar background for OSI purposes [20].

2.4 Radioargon Production and Measurement

2.4.1 Laboratory Production

Many biological and environmental applications of ^{37}Ar detection rely on the collection of samples *in vivo* or from bulk air. The interest in laboratory-based production of ^{37}Ar was a result of the need to further investigate the physics of ^{37}Ar decay [21] and to calibrate proportional counters used for environmental sampling [22, 23]. Production techniques for these purposes typically use the same

mechanisms relevant to this project: activation of air via ^{36}Ar(n,γ)^{37}Ar and irradiation of calcium samples to exploit the ^{40}Ca(n,α)^{37}Ar reaction. Results showed comparable production rates for the two mechanisms, given identical flux profiles for a ^{36}Ar-enriched air target and high-purity Ca metal target [24].

2.4.2 Detection and Measurement

Early measurement of radioargon effluents from various power reactor designs was accomplished with simple gamma spectrometry using a Ge(Li) detector, however the low-energy decay scheme of ^{37}Ar required development of internal gas-proportional counting techniques [15]. These proportional counters became the industry-standard for ^{37}Ar measurements and found use in a number of applications [17]. The use of these detectors, combined with active shielding and pulse discrimination techniques [25], achieved sensitivity equivalent to a minimum detectable concentration of roughly 20 Bq·m^{-3} [26]. It should be noted that these measurements benefitted from the use of purified argon standards rather than environmental samples collected from bulk air. Environmental sampling is subject to limits on argon extraction efficiency. Accounting for an extraction efficiency of 40%, as quoted by Aalseth et al. [23], the equivalent MDC of these systems for a bulk air sample (for the purposes of comparison to modern systems, which are typically characterized by their MDC for bulk air samples) was likely closer to 50 Bq·m^{-3}.

The motivation to use ^{37}Ar as a radiotracer for OSI has spurred a new wave of research on detection and measurement systems. Work on laboratory measurement systems has focused on the development of more sophisticated internal source gas proportional counters. Construction of the detectors with high purity, low background materials has reduced the MDC for a laboratory system to 45 mBq m^{-3}

bulk air [23]. Beyond the laboratory, a portable field detector with consolidated radioargon purification and measurement systems has been reported with an MDC of 500 mBq m^{-3} bulk air. Estimates of the lower limit on the MDC of ^{37}Ar are 0.02 mBq·m^{-3} and 20 mBq·m^{-3} bulk air for a laboratory system and a field system, respectively [11].

2.4.3 Inner Bremsstrahlung

In order to circumvent the challenges of counting the 2.6 keV X-rays produced by electron capture in ^{37}Ar, some work investigated the measurement of the inner bremsstrahlung, or braking radiation of the captured electron. The relatively low intensity of this decay scheme restricted measurement to high activity samples. After the initial work to describe inner bremsstrahlung (IB) a mechanism in certain decay modes, research focused on characterizing the IB spectrum for a variety of individual species including, ^{37}Ar [21]. The experimental work of Anderson calculated an endpoint energy for the spectrum at 815 $\pm$ 15 keV, and simultaneous theoretical projects produced the same value.

Later work reconciled the theoretical IB spectrum with the pulse height spectrum seen on the proportional counting systems [27]. The observed spectra were decomposed into the individual mechanisms to isolate the IB spectrum and estimate the ^{37}Ar source activity. The work in Refs. [21] and [27] served as the foundation of the treatment of ^{37}Ar in later research that gave a comprehensive survey of IB work-to-date at the time (1977) and presented much of the physics responsible for the mechanism [28]. The integrated intensity across the IB spectrum for ^{37}Ar was calculated at 52 $\pm$ 13$\times 10^{-5}$ per K-shell X-ray. This value has endured in the literature since its publication [24, 29, 30].

Although the measurement of the IB spectrum has been shown a valid technique for calculating the activity of a ^{37}Ar source, the challenges posed by the relatively low intensity have returned the state of the art to internal source proportional counting.

2.4.4 Ternary Fission

A variety of nuclear engineering and science applications require high precision calculations of the instantaneous and cumulative yield of binary fission products, with the familiar double-peaked fission product yield curve used to visualize the mass number distribution for various fissile species. Significantly less effort is spent characterizing those fission events that produce three, instead of two, fission products, although the phenomenon was investigated experimentally as early as 1947 [31, 32].

Among the 0.2 - 0.4% of fission events that produce three fission products, the large majority result in the creation of ^{4}He nuclei, tritons, or other lights elements. Ternary fission events are a consideration in reactor safety calculations where the buildup of helium and tritium, as ternary fission products, in fuel elements can be an engineering and environmental concern [33, 34]. As a result, experiments and simulations have focused on light-element yields from ternary fission events.

A limited set of experimentalists have attempted to quantify the yield of ternary fission products in the $Z > 4$ range and fewer still included measurements of ^{37}Ar. The first experiments, conducted by Stoenner [35], relied on radiochemical separation of the noble gases from irradiated ^{235}U samples dissolved in acid. The isotopes ^{41}Ar and ^{42}Ar were measured directly using a G-M counter. Following beta counting to measure the ^{39}Ar yield, re-measurement in an internal source proportional

counter allowed calculation of the ^{37}Ar yield. The indirect measurement resulted in high uncertainty, with an estimated yield of $8\pm2\times10^{-10}$ atoms of ^{37}Ar per binary fission (ternary fission yields are often reported normalized per binary fission event to fold the ternary fission probability into the result).

Later work by Kugler [36] exploited the higher sensitivity of mass spectrometric measurements. ^{235}U samples were irradiated under a thermal flux, then heated to leach the individual gases of interest from the sample. Although the measurements by Kugler did not face the same challenge of measuring the low energy X-ray of ^{37}Ar decay, the purity requirements for mass spectroscopy limited the precision of the measurements. The resulting maximum ternary fission yield was found to be 2.2×10^{-9} atoms of ^{37}Ar per binary fission, with an uncertainty estimated at 10%. It should be noted that isotopic analysis of all argon species present in the samples suggested that there was some contribution to the ^{37}Ar inventory from activation of air in the sample vial after the experiment, and neutron interaction with calcium impurities in the quartz vial. This effect precluded the calculation of the ternary fission yield directly, however the upper limit on the yield was calculated. Isotopic ratios were used to make similar estimates for the maximum ternary fission yields of ^{36}Ar, ^{38}Ar, ^{39}Ar, ^{40}Ar, and ^{42}Ar.

3 | Methodology

The following sections describe the physical, mathematical, computational, and experimental techniques employed in this research. Particular attention is paid to the computational techniques which are responsible for producing the key results of the project, though more fundamental considerations are also discussed. Specific input files and source codes are included in the Appendix.

3.1 Radioargon Basics

Natural argon is composed of the three stable isotopes ^{36}Ar, ^{38}Ar, and ^{40}Ar with abundances of 0.3365%, 0.0632%, and 99.6003%, respectively. Notably, it is the third most significant constituent of air at a volume fraction of 0.933%. Radioargon isotopes also exist in detectable concentrations in the environment due to the production mechanisms described in Section 2: activation of air by cosmic radiation, activation of calcium in soil by cosmic radiation, and activation of air by anthropogenic neutron sources such as reactors. In the case of ^{37}Ar, activation of soil by the neutron flux of an underground nuclear explosion is an additional production pathway.

^{37}Ar is an unstable isotope with a half-life of 35.04 days. It has a single decay mode, electron capture to the daughter ^{37}Cl:

$$^{37}\text{Ar} + e^- \rightarrow {}^{37}\text{Cl} + \nu_e$$

The 813.9 keV of decay energy is typically monopolized by neutrino emission but the occasional decay shares a measureable portion of the decay energy with bremsstrahlung radiation from the captured electron, known as inner bremsstrahlung [21]. As the vacancy of the captured K-shell electron is filled, a 2.6 keV X-ray is emitted.

At such low energy, this K-shell X-ray is easily absorbed in even low-Z materials, making measurement by an enclosed high-purity germanium (HPGe) detector difficult. Instead, ^{37}Ar measurement is typically done using internal gas-proportional counters. Although the inner bremsstrahlung continuum is measurable, the bremsstrahlung emission intensity is on the order of 1×10^{-4}, so K-shell X-ray measurement is still the preferred detection technique.

The decay modes and half-lives of the major radioargon isotopes are given in Table 3.1. The radioargon isotopes with A < 36 and A > 42 are generally short-lived and were not included as tracked isotopes for the purposes of this project.

Table 3.1: Decay data for the primary radioargon isotopes [37].

Isotope	Half-Life	Decay Mode	Comments
^{37}Ar	35.04 d	EC	2.6 keV X-ray
^{39}Ar	269 y	β	565 keV endpoint
^{41}Ar	109 min.	β	1.294 MeV γ
^{42}Ar	32.9 y	β	600 keV endpoint

3.1.1 Air Activation

The activity of radioargon in a sample of argon subject to a neutron flux can be calculated explicitly through the solution of the equations of buildup and decay. For some elemental sample subject to a neutron flux ϕ, the time-dependent

concentration of a specific isotope, M_A, can be expressed as:

$$\frac{dM_A}{dt} = -\lambda_{M_A} M_A - \sigma_{a,M}\phi M + \sigma_{c,M_{A-1}}\phi M_{A-1} + \sigma_{(n,2n),M_{A+1}}\phi M_{A+1} + \dots \quad (3.1)$$

where λ represents the decay constant, σ_a represents the absorption cross-section, σ_c represents the radiative capture cross-section, $\sigma_{(n,2n)}$ represents the cross-section for the $(n, 2n)$ reaction, ϕ represents the flux, and other terms are not shown for readibility. The terms represent loss by decay, loss by absorption, and buildup by an array of reactions in the other isotopes of M in the sample, respectively. The microscopic group cross-sections σ are weighted according to the energy profile of the flux. The time-dependent concentrations of all the isotopes in the sample can be found by simultaneous solution of the system of equations:

$$\begin{aligned}
&\vdots \\
\frac{dM_{A-1}}{dt} &= -\lambda_{M_{A-1}} M_{A-1} - \sigma_{a,M_{A-1}}\phi M_{A-1} + \sigma_{c,M_{A-2}}\phi M_{A-2} + \sigma_{(n,2n),M_A}\phi M_A + \dots \\
\frac{dM_A}{dt} &= -\lambda_{M_A}\phi M_A - \sigma_{a,M_A}\phi M_A + \sigma_{c,M_{A-1}}\phi M_{A-1} + \sigma_{(n,2n),M_{A+1}}\phi M_{A+1} + \dots \\
\frac{dM_{A+1}}{dt} &= -\lambda_{M_{A+1}}\phi M_{A+1} - \sigma_{a,M_{A+1}}\phi M_{A+1} + \sigma_{c,M_A}\phi M_A + \sigma_{(n,2n),M_{A+2}}\phi M_{A+2} + \dots \\
&\vdots
\end{aligned} \quad (3.2)$$

Analytical solution of this system quickly becomes intractable as the number of isotopes in the sample increases and as the full set of reactions are accounted for. Lower probability reactions and lower concentration isotopes are often neglected in calculations in the interest of producing an analytical solution. Matrix algebra, on the other hand, provides relatively easy access to numerical solutions of the system. Let Equations (3.2) represent the concentrations of an arbitrarily large set of isotopes of some species M. Then M_A is the concentration of the isotope with

mass number A. In matrix notation the system can be expressed as:

$$[\boldsymbol{M'}] = [C]\,[\boldsymbol{M}] \tag{3.3}$$

where $[\boldsymbol{M'}]$ is a vector of the values dM_A/dt, $[C]$ is the matrix of coefficients in the system given by Equation (3.2), and $[\boldsymbol{M}]$ is a vector of the concentrations of the isotopes of M. Following the method of Moral [38], the concentration vector can be found through the decomposition of the coefficient matrix $[C]$:

$$[\boldsymbol{M}] = [V]\,[\Lambda]\,[V]^{-1}\,[\boldsymbol{M_o}] \tag{3.4}$$

where $[V]$ is the matrix of eigenvectors of $[C]$, $[\boldsymbol{M_o}]$ is a vector of the initial concentration of the isotopes of M, and $[\Lambda]$ is defined as:

$$[\Lambda] = \begin{pmatrix} e^{\Lambda_1 t_i} & 0 & 0 & \dots & 0 \\ 0 & e^{\Lambda_2 t_i} & 0 & \dots & 0 \\ \vdots & \vdots & \vdots & \ddots & 0 \\ 0 & 0 & 0 & 0 & e^{\Lambda_n t_i} \end{pmatrix} \tag{3.5}$$

In Equation (3.5), Λ_n represents the eigenvalues of $[C]$ and t_i denotes the irradiation time. The matrix $[C]$ must be carefully constructed: if the n isotopes in the system are assigned indices 1 through n, any off-diagonal term (i, j) in the matrix $[C]$ must represent the coefficient for the reactions that produce isotope i from isotope j. The diagonal terms (i, i) then represent the decay and loss by absorption in isotope i, and the matrix is indexed to be lower-diagonal. The decomposition of $[C]$ by the form of Equation (3.4) introduces numerical imprecision in the calculation of the matrix exponential $[\Lambda]$ [39]. This imprecision is small relative to other uncer-

tainties in the actual calculations, however the inclusion of a large set of isotopes in the calculation can result in a form of $[C]$ without an invertible matrix of eigenvectors $[V]$. The condition number of $[V]$ can be used to estimate the maximum uncertainty incurred by this imprecision.

The concentration of all the isotopes in the sample are contained in the vector $[\boldsymbol{M}]$ which can be calculated for an arbitrary irradiation time t_i, and the activity of any isotope after some decay time following irradiation can be trivially calculated from this vector.

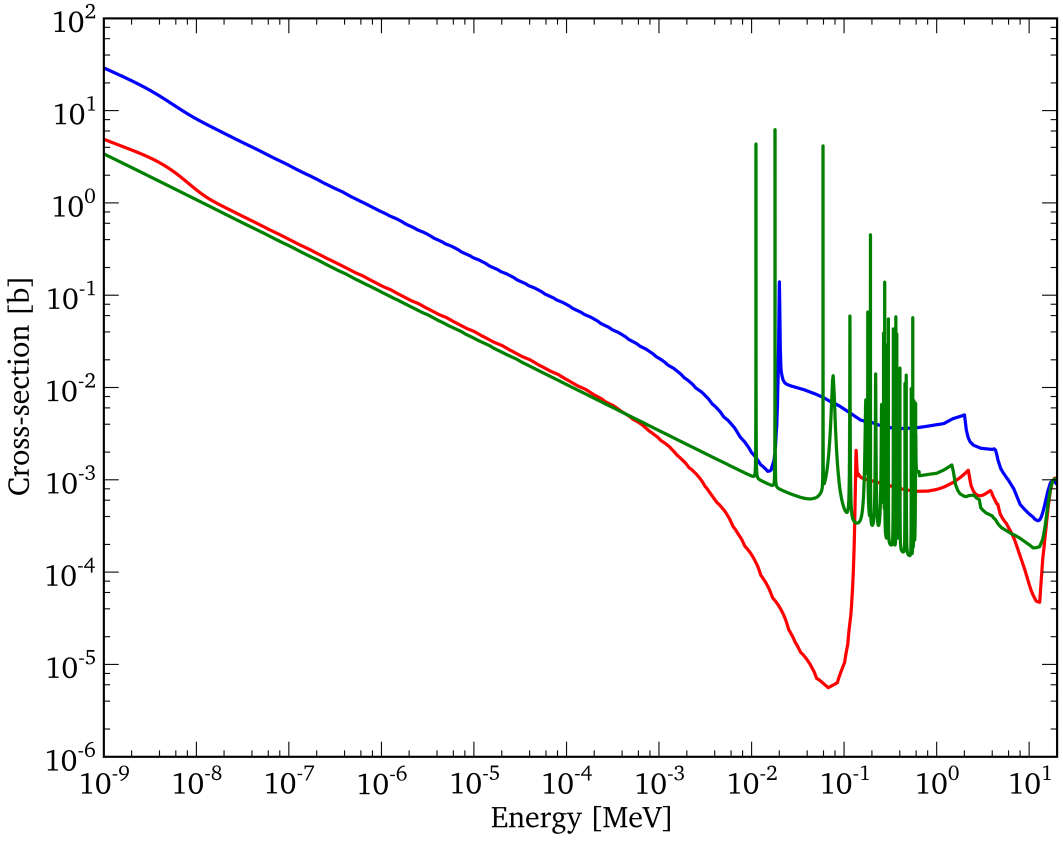

Figure 3.1: Cross-section for ^{36}Ar(n,γ)^{37}Ar (in blue), for ^{38}Ar(n,γ)^{39}Ar (in red), and for ^{40}Ar(n,γ)^{41}Ar (in green) [37].

One distinct advantage of this approach is that accounting for the comprehensive set of reactions for each isotope only requires that those coefficients be included in the matrix $[C]$. A multielement system could be solved identically. Using this method, along with a flux profile generated by radiation transport modeling, reaction cross-sections from nuclear data sets, and isotopic composition of the target material, the radioargon concentration produced in various regions of a reactor can be calculated.

The (n, γ) reactions in the stable Ar isotopes is likely the dominant reaction for production of the radioargon isotopes in the activation of air. The ENDF/B-VII.1 cross-sections for the (n,γ) reactions in the stable argon isotopes are shown in Figure 3.1. Smaller contributions may come from $(n, 2n)$ reactions ^{38}Ar and other, multi-reaction chains during irradiation. The effects of these lower-probability pathways are accounted for in the numerical solution to Equations (3.2) and their relative contributions are explored in the discussion of the results in Chapter 7.

3.1.2 Calcium Activation

Neutron irradiation of ^{40}Ca will produce ^{37}Ar as a result of the ^{40}Ca$(n, \alpha)^{37}$Ar reaction. The method outlined in Subsection 3.1.1 can be used, with the appropriate cross-sections, to calculate the production of ^{37}Ar by irradiation of calcium. The intricacies of the calcium activation case lie in the fact that the ^{37}Ar is being produced in a matrix that it must diffuse out of and that the concentration of target nuclei is not necessarily known (neither of which is true for the air activation case). These issues are discussed in greater detail in Section 3.4. For reference, the ENDF/B-VII.1 cross-section data for the ^{40}Ca(n,α)^{37}Ar reaction is shown in Figure 3.2.

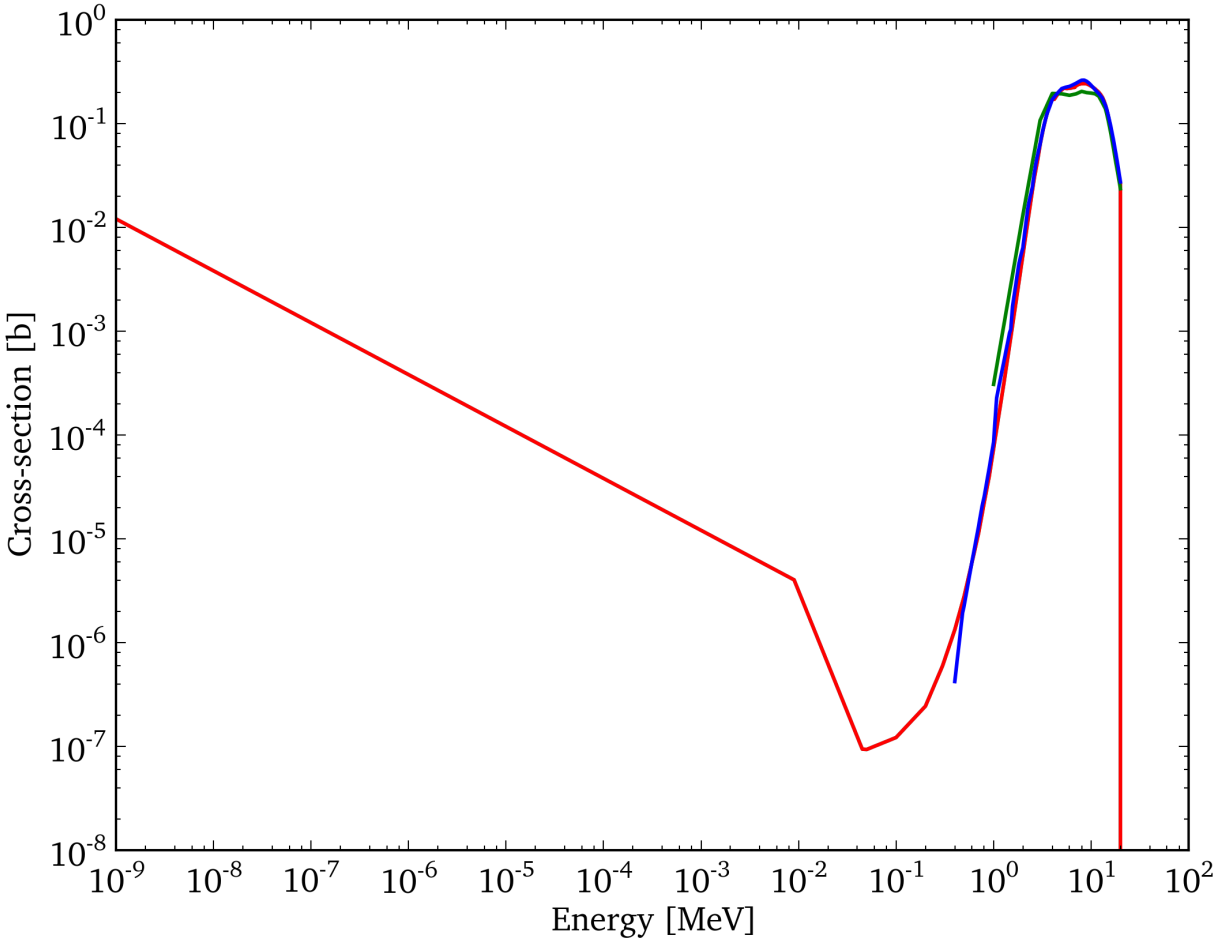

Figure 3.2: Cross-section for ^{40}Ca(n,α)^{37}Ar. Data from ENDF/B-VII (cyan), JEFF/ROSFOND (red), JENDL-3.3 (green), and JENDL-4.0 (blue) are shown [37].

It should be noted that the low energy region (< 1 keV) is populated with extrapolated data assuming $1/v$ behavior of the cross-section. Experimental data exists only in the energy range greater than 1 keV for most data sets. The effect of substituting ^{40}Ca(n, α) cross-section data from different nuclear data sets is explored in greater detail in Section 5.

3.2 Radiation Transport

The radiation transport model of the University of Texas Nuclear Engineering Teaching Laboratory's (NETL) TRIGA reactor was created using version 2.7.0 of the Los Alamos National Laboratory Monte Carlo N-Particle X (MCNPX) software package. MCNP is a common tool in applications of physics, nuclear science, and nuclear engineering and has undergone extensive validation across its versions.

The model of the NETL TRIGA was constructed using the engineering plans of the reactor and fully represents the operational set up of the reactor core with few exceptions. Fuel elements are modeled according to specified fuel type and composition, and the core fuel arrangement in the model matches that of the real core in its configuration as of December 2012. The exact geometry of the flutes on either end of the fuel elements is not modeled, though the approximate geometry is modeled and the effect on the radiation transport results is expected to be negligible. Fuel burnup, and the associated isotopic composition of the major fission products in the fuel, is beyond the scope of the work and not included. The rest of the core superstructure, including grid plates, reflector, reflector shrouds, control rods, in-core irradiation facilities, beamports, and water coolant are also included in the model. Vertical and lateral cross-sectional views of the reactor core in its MCNPX geometry are shown in Figures 3.3 and 3.4, respectively. For the purposes of modeling full-power physics, the fuel temperature was set at 600 K/326 C (MCNPX material data for ZrH is limited to table data for 294 K, 400 K, 600 K, 800 K, 1000 K, and 1200 K).

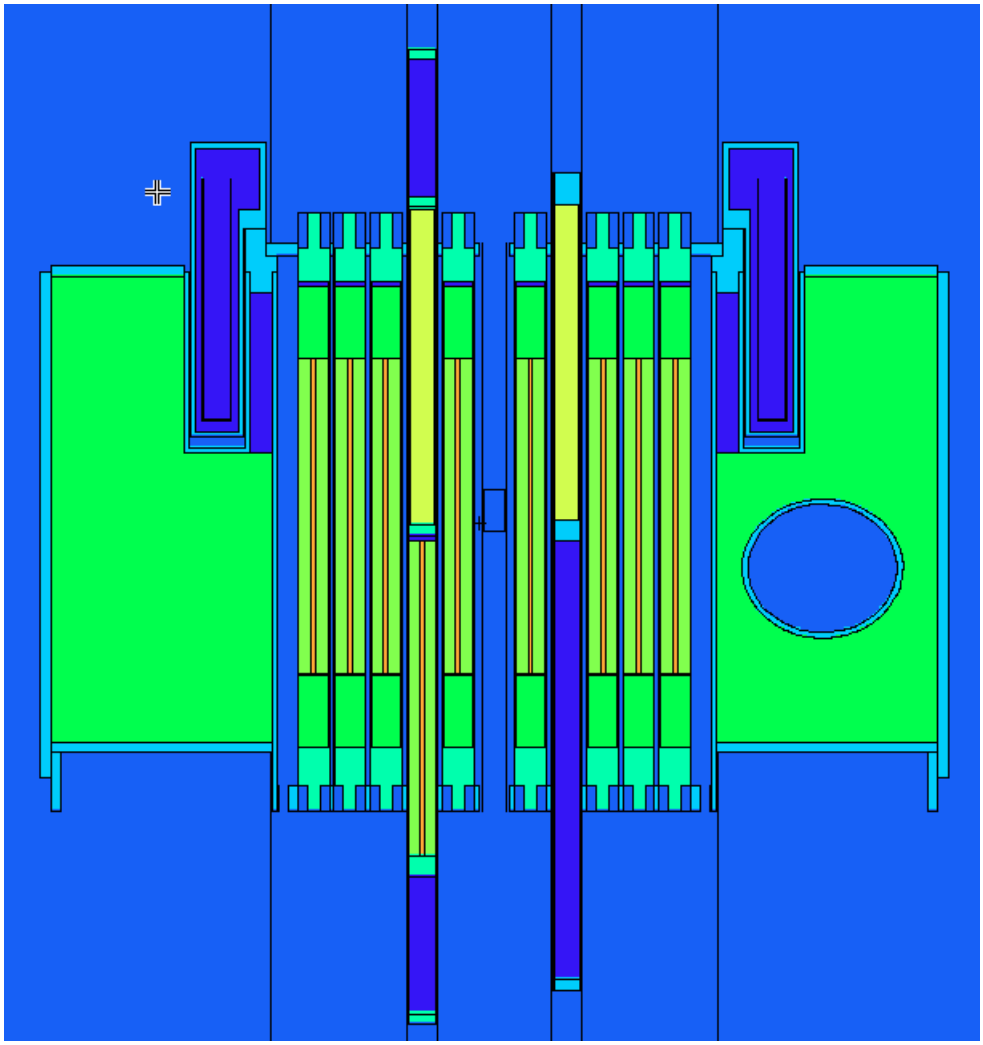

Figure 3.3: Vertical cross-section view of the TRIGA core modeled in MCNPX. Colors indicate different materials. The throughport for BP1/5 is visible on the right.

The concrete biological shield and full pool volume are included in the model, but are generally excluded from the problem geometry for calculations in which those regions are irrelevant, such as in-core neutron flux tallies. The significant increase in computational expense to calculate neutron transport in a highly scattering material (such as water) makes it prudent to include the complete geometry

only when absolutely necessary.

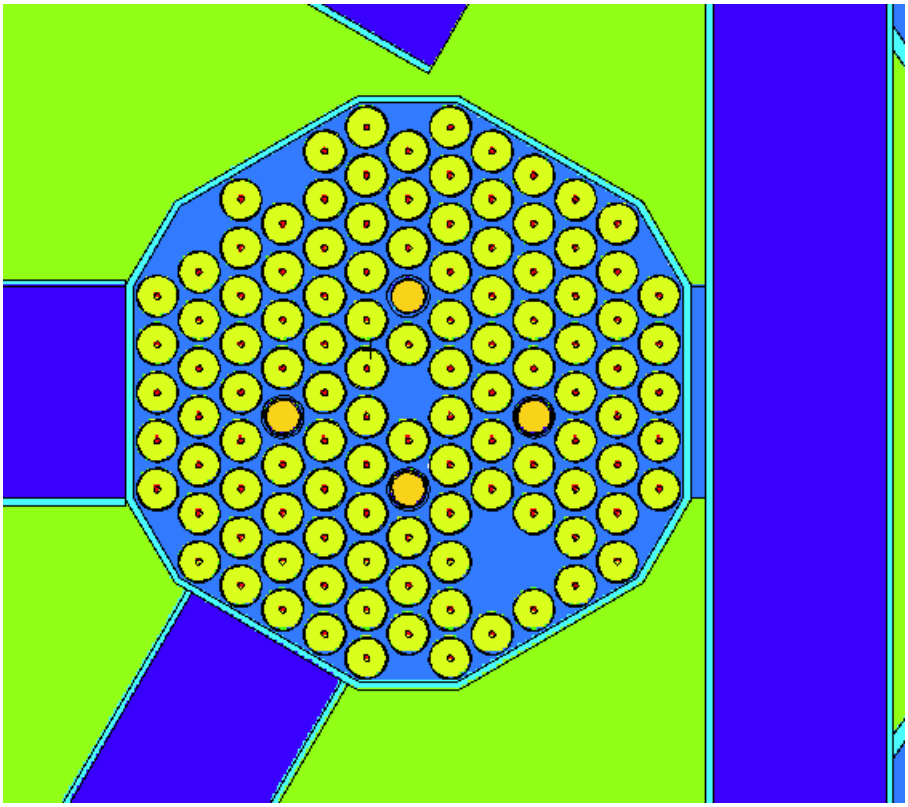

Figure 3.4: Lateral cross-section view of the TRIGA core modeled in MCNPX. Colors indicate different materials. The 3L irradiation canister is not shown.

Modeling of the beamport facilities was enabled using details found in previous publications and theses based on work completed at the University of Texas at Austin. Each beamport, in reality, is designed with a number of radiation filters, beam collimators, and other pieces of equipment to produce the desired beam characteristics at the point of the sample. Each arrangement has an effect on the interaction of the neutron flux of the beamport with the air and other surrounding materials. Complete characterization of each beamport facility was beyond the scope of this project, however each facility was represented with a reasonable level

of fidelity based on available information. The accurate geometry of each beam tube from the core to the outside surface of the biological shield was included. A cross-sectional view of the full reactor, including the core, pool, biological shield, and beamports, is shown in Figure 3.5. Details for BP2 were taken from the work of Whitney [40, 41] and Saglam [42], BP3 from the work of Alvarez [43], and BP5 from the work of Cao [44] and Doron [45]. Beamports 1 and 4 were empty at the time of this project.

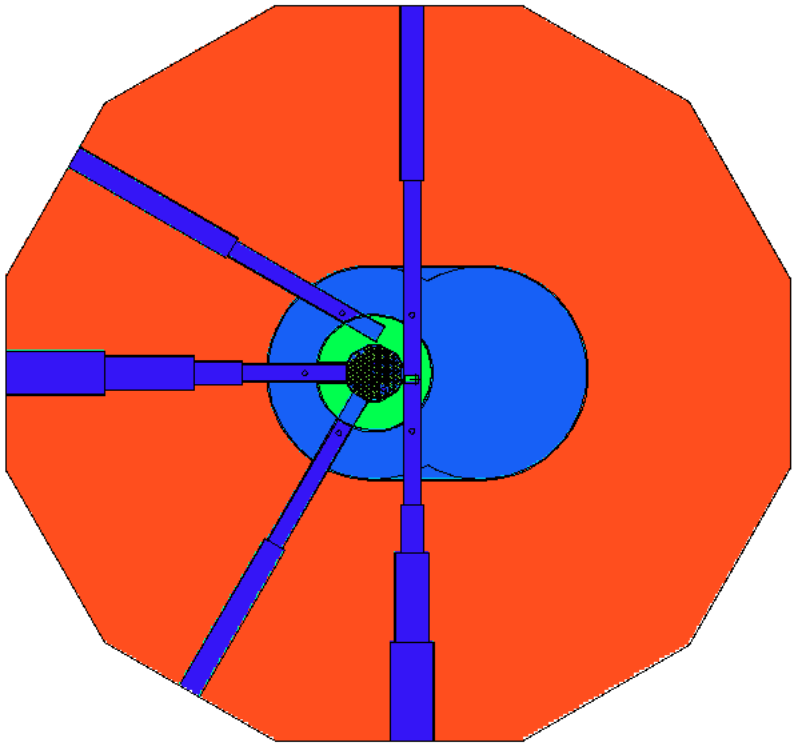

Figure 3.5: Lateral cross-section view of the TRIGA reactor modeled in MCNPX. Colors indicate different materials.

The number of particle histories necessary for good statistics and the format of individual tally calculations varied depending on the result of interest and often the

quality of statistics was limited by access to sufficient computing time. The details on the approach to tallying can be found in the following sections. The general MCNPX input file used to produce the radiation transport results can be found in Appendix A.

3.2.1 Flux Tallying

The fundamental use of MCNPX in this project is the calculation of the neutron flux in the radiaorgon-producing regions of the reactor. A specific measurement in an MCNPX model is referred to as a tally. Typical tallies in MCNPX track the transport of a particular particle type in some specified region. This region can be a surface or volume in the problem geometry, among other, more advanced tally options. For most tally methods, the result calculated by MCNPX is given in dimensions of particles $\cdot$ cm^{-2} $\cdot$ SP^{-1} where, by default, all MCNPX tallies are normalized per source particle (SP) history. There are a number of methods, both manual and automated in the software, by which this value can be used to calculate the group constants needed to solve the depletion problem.

If the model can be benchmarked against empirical data such that the energy-dependent flux profile produced in MCNPX matches that of the actual reactor system, experimental data can be used to calculate a conversion factor from dimensions of particles $\cdot$ cm^{-2} $\cdot$ SP^{-1} to typical flux dimensions of n $\cdot$ cm^{-2} $\cdot$ s^{-1}. With the energy-dependent flux calculated, published cross-section data can be used to calculate the group constants.

Although the default output dimensions are particles $\cdot$ cm^{-2} $\cdot$ SP^{-1}, the normalization changes if the tally is run in conjunction with a KCODE criticality calculation. In a KCODE simulation an initial, user-defined source distribution is transported to

determine where fission events are happening. Each cycle updates the source distribution to better represent the fissionable material in the problem. When the source distribution has converged, KCODE uses this distribution to calculate the k-value of the problem, along with any tallies that may be included in the input file.

Because KCODE sources are actually modified by the simulation itself, tallies in KCODE runs are normalized per fission neutron (FN) rather than per initial source particle. The typical flux tally integrated over a volume, the F4 tally, then has output dimensions of particles $\cdot$ cm^{-2} $\cdot$ FN^{-1} when run with a KCODE calculation. This new normalization scheme is important because it allows for conversion to usable units n $\cdot$ cm^{-2} $\cdot$ s^{-1} without the need for benchmarking data from experiments. In order to convert to the desired dimensions of flux, the following constants and unit conversions are needed:

$$\left[\nu \, \frac{\text{fission neutrons}}{\text{fission}}\right] \cdot \left[\frac{1}{E_f} \frac{\text{fission}}{\text{MeV}}\right] \cdot \left[E \, \frac{\text{MeV}}{\text{J}}\right] \cdot [P \text{ W}]$$

where ν is known for a given fissile material, E is a defined physical quantity, and P is the given power of the system being modeled. When the MCNPX F4 tally output is multiplied by this quantity, the resulting dimensions are particles $\cdot$ cm^{-2} $\cdot$ s^{-1} at a given power level P. The value $E_f = 200$ MeV was used, however actual values of E_f in a reactor are subject to reactor type, reactor design, and fuel burnup [46]. A rigorous method for calculating E_f is presented in Ref. [46].

The tally functionality can be extended further to calculate the rate of a particular reaction in the materials in the problem using the tally modification (FM) card. For an energy-dependent response function $R(E)$ that is defined in MCNPX,

the tally modifier can be used to calculate the value:

$$C \int_E \phi(E) R(E)\, dE$$

where $\phi(E)$ is the standard F4-calculated flux and C is some user-defined constant. The general form of a reaction rate is given by:

$$RR = \int_E \phi(E) N \sigma(E)\, dE$$

where N is the number density of the target material and $\sigma(E)$ is the energy-dependent reaction. If $R(E)$ is chosen to be the cross-section of the reaction of interest and C is chosen as the number density of the target material, the result of Equation 3.2.1 will be a reaction rate density. Cross-sections accessible to MCNPX are available to use as response functions.

The dimensions of each term in Equation 3.2.1 are

$$C \left[\frac{\#}{\text{cm}^3} \right] \cdot \phi \left[\frac{\text{particles}}{\text{cm}^2 \cdot \ \text{FN}} \right] \cdot \sigma \text{ [b]}$$

It is important to note that ENDF cross-sections are defined in barns (as opposed to cm^2), so consolidation of dimensions requires the conversion factor 1×10^{-24} $\text{cm}^2 \cdot \text{b}^{-1}$. After consolidating to cm, the dimensions of the FM modified quantity are reactions $\cdot$ $\text{cm}^{-3} \cdot \text{FN}^{-1}$ which can be converted to reactions $\cdot$ $\text{cm}^{-3} \cdot \text{s}^{-1}$ at a given power level by following the steps detailed above. Multiplication by the volume of the region containing the target material gives the total reaction rate for that region. This value can also be divided by the constant C and the group flux, as calculated by MCNPX, to provide the group cross-section for the reaction of interest.

The manipulations and calculations described in this section can be employed to calculate the group constants necessary to construct the depletion coefficient matrix described in Section 3.1.1 and solve the depletion problem using the code described in Section 3.2.3. The group constants can also be calculated using the depletion code developed for this work, described in Section 3.2.3.

3.2.2 Variance Reduction and Statistics

The statistical quality of a tally in MCNPX is dependent primarily on the number of particles scoring for that tally: the more particle histories that contribute to the tally of interest, the better the convergence of the tally result to the actual physical quantity of interest. In the case of an F4 or other volumetric tally, the more particles passing through the tallied volume, the lower the error for that particular tally. For tallies in or near the core, errors can be reduced below the 1% threshold with reasonable computational expense by increasing the number of particle histories that are simulated. This is a result of the relatively high probability of an in-core tally region being transected by source particles. For tallies outside the core where the probability of a particle reaching the region of interest is low (especially if separated from the core by water or other highly scattering media), achieving acceptable statistics is more difficult.

In order to reduce the variance and improve the statistics of such tallies, a number of native techniques can be implemented in MCNPX. These variance reduction techniques often represent non-physical behavior of source particles or secondary particles such that less computation time is spent on particle histories that will not contribute to the tally. The physical integrity of the model is maintained by scaling the results of the tally to account for the bias introduced by the variance reduction.

For the TRIGA reactor model, the primary computation challenge is transport of source neutrons through the highly scattering water moderator/coolant to score on tallies in the outer beamport regions, at the biological shield, or in the water itself. Two variance reduction techniques were employed in the model to mitigate the expense of tallying in these regions: weight windowing and point detector tallies.

Included in the definition of any geometric region (or cell) in an MCNPX model is the assignment of the "importance" of that cell. The importance dictates how MCNPX treats particles as they move from cell to cell. Each source particle in a MCNPX run is created with an assigned "weight" of 1. If this full-weight particle reaches a scored tally region, it will be counted as a full particle for the purposes of the tally. However, in order to make particle transport more efficient, MCNPX will split and recombine particles as they move through the cells of the problem. If a particle is split into 4 new particles, each new particle has a weight of 0.25. Throughout the problem, the weight of particles is conserved to maintain the physical integrity of the model. Weight windows are assigned upper and lower limits on the weight of particles. If a particle's weight falls below the lower limit, a probabilistic calculation is run to either end the particle's history or to reassign the weight above the limit. If a particle's weight goes above the upper limit, it is split into multiple lower-weight particles. MCNPX calculates these limits on a cell-by-cell basis for a given tally to optimize the transport of particles that likely to contribute to that tally. In practice, weight windows enable the transport of more particles (at lower weights) through highly scattering media to improve the statistics of tallies. Without weight windows, the statistics would only be improved by running a very large number of particle histories.

Weight windows will be used for full reactor model to calculate tallies in the reactor pool, the biological shield, and in the regions of the beamports at the edges

of the biological shield.

The other variance reduction technique used is the point detector (F5) tally. Typical flux tallies in MCNPX score particles as they transect a surface or a volume; particle histories that do not cross tally surface or enter the tally volume are not scored. The F5 tally scores the contributions of all particles as they move through their history. The differential contribution to the tally at each scattering location or each cell crossing is calculated according to:

$$\delta\Phi = \frac{W\mu(E,\theta_s)}{\mu(E)r^2}e^{-\mu(E)r}$$

where $\delta\Phi$ is the contribution to the total tally Φ, W is the weight of the particle, r is the distance between the particle and the location of the F5 tally, μ is the linear attenuation coefficient, and the term $\mu(E,\theta_s)/\mu(E)$ represents the probability at the time of the calculation that the particle scatters towards the point detector. The advantage of the F5 tally is that all events in the history of all particles contribute to the total tally. The larger number of contributions serves to reduce the variance of the result.

F5 tallies are defined by a position in the problem geometry and by an exclusion radius. The exclusion radius sets a region around the point of the tally for which particles and events will be ignored. Without the exclusion radius, scattering events very near the detector would produce very large contributions to the tally and increase the variance. Exclusion radii are typically small for low-scattering media, and must be made larger for highly-scattering media.

F5 tallies are used to calculate the neutron flux in the outer regions of the reactor pool and biological shield where individual particles are unlikely to directly score in a volume tally due to the distance from the reactor core where they are produced.

3.2.3 Depletion Calculations

There are a number of depletion codes available to track the concentration of a set of isotopes that are subject to a neutron flux. The Oak Ridge Isotope Generation code (ORIGEN), part of the SCALE reactor modeling package, is publicly available and commonly used for tracking isotopics in typical power reactor environments. ORIGEN includes tabled multigroup data calculated for various power reactor assemblies at various levels of burnup, and arbitrary systems of isotopes can either be tracked during reactor operation or during an independent irradiation. The VESTA and MONTEBURNS codes both interface with MCNPX to generate flux profiles, calculate burnup and depletion, and iterate over new flux calculations. Other codes offer similar capabilities, or specifically focus on a small, fixed set of isotopes.

In general, these codes are designed for power reactor burnup calculations and are relatively inflexible with regards to the input parameters from the user. ORIGEN-ARP restricts calculations to the pre-calculated multigroup constants for power reactor assemblies with only the magnitude of the thermal flux adjustable by the user. MONTEBURNS relies on 63-group cross-sections from the CINDER90 package (which are automatically weighted by a typical LWR flux profile and include mixed data even within specific reactions) or relies on the same cross-section tables used by ORIGEN.

The problem of interest for this project does not involve an extensive set of fission products which must be tracked through the burnup of reactor fuel, but instead focuses on the production of a limited set radioargon isotopes (and other isotopes with similar A and Z to argon which may contribute to radioargon production). In order to exploit the need to track only these few isotopes, a custom depletion code was written. The purpose of the code is to allow flexibility with regards to the flux

profile, isotopes tracked, reactions included, choice of cross-sections, and treatment of group constants. This flexibility enables analysis of the sensitivity of radioargon production to individual isotopes, reactions, and changes in flux profile.

The core of the depletion code is the numerical solution of the buildup and decay equations following the method described in Section 3.1.1. The code reads user-created input files specifying the isotopes to be tracked, the initial concentration of the each isotope, and the flux distribution. Multigroup constants are calculated for the flux profile, and collapsed to a single group, then the depletion calculation is run for a user-specified amount of time. The isotopic vector of the tracked isotopes is written to a file for analysis.

The code includes other routines for processing of input files, automated preparation of group cross-sections using NJOY99, and formatting of output. The depletion routines were written in the Python programming language. The complete source for the routines, along with descriptions of the individual subroutines, is included in Appendix B.

3.2.4 Cross-Section Data

A key consideration for both the flux calculations in MCNPX and the depletion calculations is the cross-section data used. There is an array of nuclear data sets available that each calculate reaction cross-sections using different experimental techniques, use different energy ranges and resolutions, focus on different incident particle types, and rely on different sets of model or table data for filling in missing cross-sections. For the neutron interactions of interest in this project, data sets include the Evaluated Nuclear Data File (ENDF) from Brookhaven National Laboratory [47], the Joint Evaluated Fission and Fusion File (JEFF) from the OECD's

Nuclear Energy Agency [48], and the Japanese Evaluated Nuclear Data Library (JENDL) from the Japan Atomic Energy Agency [49], the Russian File of Evaluated Nuclear Data (RUSFOND) [50], among others.

For commonly investigated target isotopes (fuel materials, shielding materials, detector materials) and reactions with specific applications, the cross-section data is typically high resolution and consistent across the evaluated data libraries. For less commonly investigated reactions (including many neutron interactions with the argon isotopes or other light nuclei) results produced by radiation transport modeling can vary (sometimes significantly) depending on the data set used for the calculation. Further, for many of the data sets that do exist for these reactions which are of particular importance in this project, the energy resolution is low and some energy regions are populated with interpolated, extrapolated, or model-generated data.

Flux results derived directly from the reactor model relied on the default MCNPX cross-section libraries. As mentioned in Subsection 3.2.3, the flexible nature of the depletion code allowed for use of any ENDF-formatted data set on a reaction-by-reaction basis. ENDF/B-VII data was used where available, however JENDL, JEFF, EAF, and ROSFOND data were all used in specific cases where ENDF/B-VII data was not available. Sensitivity of the results to the use of different data sets is discussed in Chapter 5, however the majority of the calculations in the depletion code were done using the following mixed data set, arranged to show which data set was used for each isotope included in the typical depletion calculation:

- **ENDF/B-VII.1:** ^{36}Ar, ^{38}Ar, ^{40}Ar, ^{40}Ca, ^{42}Ca, ^{35}Cl, ^{37}Cl, ^{40}K, ^{31}P, ^{32}S, ^{33}S, ^{34}S, ^{36}S
- **JENDL4.0:** ^{39}K, ^{41}K
- **JEFF3.1:** ^{42}K

- **ROSFOND:** ^{37}Ar, ^{39}Ar, ^{42}Ar, ^{41}Ca, ^{36}Cl, ^{32}P, ^{33}P, ^{35}S
- **EAF-2010:** ^{41}Ar

Though the source of different cross-section data differs, as shown above, most files were collected from the NNDC ENDF repository [47]. All reactions available in each cross-section file were accounted for in the depletion calculation with the exception of scattering and other interactions that do not change the A or Z value of the target nuclide. As mentioned in Subsection 3.2.3, the flexible nature of the depletion code allowed for the exclusion of any individual reaction in the depletion calculation. The relative contributions of the various buildup pathways was explored by selectively excluding specific reactions and observing the effects on the result. This sensitivity is described in Chapter 7.

3.3 Air Content of Water

The TRIGA design of the NETL reactor relies on an open water pool for cooling and moderation of the reactor. For the NETL reactor, the pool is 8.2169 m deep and is formed as the union of two cylinders of diameter 1.9812 m axially separated by 1.9812 m. The orientation of the core in the pool and the biological shield is shown in Figure 3.5. Accounting for the displacement of the core structure and the beamport sleeves, the water volume of the pool is 39.7468 m^3 for a water level of 8.179 m. As a result of the open pool design of the reactor, there is a degree of interaction between the water at the pool surface and the bulk air of the facility that will produce some equilibrium level of saturation with atmospheric gases, including stable argon.

The solubility of a gas in a liquid is generally given as constant in units of mass

or volume of solute gas per unit mass/volume of unit solvent liquid. Although the solubility is given as a scalar constant, it is dependent on both the composition of the solute and solvent, as well as the temperature and salinity of the solvent.

Henry's Law states that the solubility of a gas in liquid is directly proportional to the pressure of the gas above the liquid. Henry's Law can be expressed as:

$$c_{aq} = \frac{p}{k_H} \tag{3.6}$$

where c_{aq} is the concentration of the solute in the solvent, p is the pressure of the solute in equilibrium with the solvent, and k_H is a scalar constant describing the solubility. The value k_H is often called the Henry coefficient. The value of k_H has been calculated for many solvent-solute pairs and is characteristic only for a given equilibrium temperature. In the practical case of atmospheric argon (as a part of the air mixture) interfacing with water, the partial pressure of argon must be used:

$$c_{aq} = \frac{p_p}{k_H} \tag{3.7}$$

Partial pressure is a measure of the pressure contribution of one component of a mixture to the total pressure of the mixture. For argon at a volume fraction of 0.93% of air at STP, the partial pressure is 9.3×10^{-3} atm.

For air solute at 1 atm and water solvent at 23C, $c = 1.3175\times10^{-8}$ mol $\cdot$ cm^{-3} [51]. The volumetric conversion of this value, $c = 0.294$ mL $\cdot$ L^{-1} is consistent with the findings of early experimental work on argon solubility in water and more recent confirmations [52, 53, 54]. These values are used to calculate the number density of argon isotopes in the water of the NETL TRIGA reactor pool.

To determine whether the diffusion rate of radioargon out of the pool is signif-

icant relative to the half-life of the various radioargon isotopes, a simplified model of gas-water exchange can be used to describe the exchange of argon across the pool-air interface. The model considers steady-state diffusion at the boundary:

$$J = -D\nabla\varphi \tag{3.8}$$

where J is the gas flux across the boundary, D is the diffusivity of the gas, and φ is the concentration of the gas. If a constant concentration of gas is assumed across the surface area of the boundary, Equation (3.8) reduces to:

$$J = -D \cdot A \cdot \frac{(\varphi_S - \varphi_B)}{\delta z} \tag{3.9}$$

where φ_S is the equilibrium concentration at the boundary, φ_B is the concentration in the bulk liquid, A is the surface area of the boundary and J has dimensions of concentration per unit time. The value δz is the stagnant boundary layer in the liquid where the concentration gradient exists. The value $D/\delta z$ is known as the "transfer coefficient" or "piston velocity" and is empirically determined for a specific gas-liquid pair for a given set of temperature and salinity conditions. For argon gas in fresh water with relatively stable conditions in the air above the liquid, the transfer coefficient has been calculated at $(3.139\pm0.27)\times10^{-3}$ cm·s^{-1} [55]. This value equates to an exchange rate of 0.113 m·h^{-1}. Considering empirical values of the diffusivity of argon gas dissolved in water, $(2.0\pm0.2)\times10^{-5}$ cm^2·s^{-1} for similar conditions [56], the thickness of the exchange layer at the boundary can be estimated at $(6.371\pm0.27)\times10^{-3}$ cm. Typical boundary layers range between 1×10^{-4} and 1×10^{-3} cm, depending on the gas, liquid, and atmospheric conditions.

This exchange rate and boundary layer thickness will be used to estimate the

concentration flux of radioargon out of the reactor pool given the buildup calculated in Section 5.3.2.

3.4 Diffusion for Ca-Generated Argon

The method detailed in Section 3.1.2 is used to calculate the radioargon source term in a calcium matrix. This source term provides the radioargon concentration as a function of position in the matrix. Using this as an initial condition, the diffusion equation can be solved for a simplified system to estimate the diffusion behavior of the radioargon out of the calcium matrix and into the surrounding medium (whether that medium is water or air or some other material).

The general diffusion equation can be expressed as:

$$\frac{\partial \psi(x,y,z,t)}{\partial t} = D_x \frac{\partial^2 \psi}{\partial x^2} + D_y \frac{\partial^2 \psi}{\partial y^2} + D_z \frac{\partial^2 \psi}{\partial z^2} \tag{3.10}$$

and for a simplified one-dimensional system:

$$\frac{\partial \psi(x,t)}{\partial t} = D \frac{\partial^2 \psi}{\partial x^2} \tag{3.11}$$

where ψ is the concentration of some specie as a function of time t and position x and D is the diffusion coefficient of that specie in the matrix. Consider the diffusion of a some specie out of a material over the interval $[0, L]$ into a medium in the

region $x > L$. The initial conditions are as follows:

$$\begin{aligned} \psi(x,0) &= f(x) \\ \psi(0,t) &= 0 \\ \frac{d\psi}{dx}(L,t) &= -\kappa\psi(L,t) \end{aligned} \tag{3.12}$$

where Equation (3.12) is known as a Robin boundary condition. This boundary condition states that the time rate-of-change of the concentration at the boundary depends on concentration at the boundary according to some scaling factor κ. Let $\psi(x,t)$ be separable such that it can be expressed as:

$$\psi(x,t) = X(x)T(t) \tag{3.13}$$

where X is only a function of the position x and T only a function of the time t. Substituting this into Equation (3.11) gives:

$$\begin{aligned} \frac{\partial}{\partial t}\left[X(x)T(t)\right] &= D\frac{\partial^2}{\partial x^2}\left[X(x)T(t)\right] \\ X(x)T'(t) &= DX''(x)T(t) \\ \frac{T'(t)}{DT(t)} &= \frac{X''(x)}{X(x)} \end{aligned} \tag{3.14}$$

In order to satisfy Equation (3.14) for all values of (x,t), each side must equal a constant. This constant will be denoted as k, leaving the following:

$$\begin{aligned} X'' - kX &= 0 \\ T' - DkT &= 0 \end{aligned} \tag{3.15}$$

Application of the boundary conditions leads to the following set of solutions for the spatial variable:

$$X_n(x) = c_n \sin \mu_n x \tag{3.16}$$

where c_n is the set of scaling coefficients and μ_n is the set of constants born from the separation in Equation 3.14 and is defined by:

$$\tan \mu L = -\frac{\mu}{\kappa} \tag{3.17}$$

Defining $\lambda = \mu\sqrt{D}$, the set of solutions for the temporal component can be expressed as:

$$T_n(t) = ce^{-\lambda_n^2 t} \tag{3.18}$$

Recalling the separation of variables:

$$\psi_n(x,t) = T_n(t)X_n(x) = c_n e^{-\lambda_n^2 t} \sin \mu_n x \tag{3.19}$$

A linear combination of solutions is also a solution, so Equation (3.19) can be generalized as:

$$\psi(x,t) = \sum_{n=1}^{\infty} c_n e^{-\lambda_n^2 t} \sin \mu_n x \tag{3.20}$$

It can be shown through the use of Fourier series solutions that the coefficients

c_n are given by:

$$c_n = \frac{\int_0^L f(x) \sin \mu_n x dx}{\int_0^L \sin \mu_n x dx} \tag{3.21}$$

where $f(x)$ is the function describing the initial concentration distribution in the medium, as specified in the boundary conditions.

Using Equation (3.20) and (3.21), $\psi(x,t)$ can be solved for the case of radioargon diffusing out of a concrete matrix with knowledge of the following:

- D, the diffusion coefficient for Ar in concrete
- L, the dimension of the concrete matrix
- μ_n, from numerical solutions to equation (3.17)
- $f(x)$, the initial concentration distribution of radioargon in the concrete
- κ, the coefficient relating the diffusion of Ar to the external Ar concentration

This calculation will illuminate whether the diffusion time for radioargon produced in concrete is significant relative to the half-life of the isotopes.

3.5 Atmospheric Transport

The diffusion of radioargon as it is released from a reactor stack can be modeled a number of ways. Although a more sophisticated tool like HYSPLIT will be used for transport modeling in this project, simplified plume models will be manually constructed to support the results of the computational model.

Let $C(x,y,x,t)$ represent the time- and space-dependent concentration of a gas released from a stack of height H at a rate of Q kg·m^{-3}·s^{-1}. Fundamentally the

time rate of change of C is given by:

$$\frac{\partial C}{\partial t} = \text{sources} \; - \; \text{losses} \tag{3.22}$$

Among the source and loss mechanisms are diffusion, transport by wind, creation by the stack, absorption in chemical species in the air, and deposition on the ground. In this simplified case, absorption and deposition are ignored and the wind is assumed to be parallel to $\hat{x}$ with velocity V. The individual contributions are then:

- diffusion, $\frac{\partial}{\partial x}\left(D\frac{\partial C}{\partial x}\right) + \frac{\partial}{\partial y}\left(D\frac{\partial C}{\partial y}\right) + \frac{\partial}{\partial z}\left(D\frac{\partial C}{\partial z}\right)$
- stack point source, $Q\delta(x)\delta(y)\delta(z-H)$
- wind, $V\frac{\partial C}{\partial x}$

so the equation describing the system is:

$$\frac{\partial C}{\partial t} = \frac{\partial}{\partial x}\left(D\frac{\partial C}{\partial x}\right) + \frac{\partial}{\partial y}\left(D\frac{\partial C}{\partial y}\right) + \frac{\partial}{\partial z}\left(D\frac{\partial C}{\partial z}\right) - V\frac{\partial C}{\partial x} + Q\delta(x)\delta(y)\delta(z-H) \tag{3.23}$$

where D is the diffusion coefficient. If it is assumed that the effect of diffusion in the $\hat{x}$ direction is small relative to the effect of wind, and that the diffusion coefficients are constant for y and z, the equation simplifies to:

$$\frac{\partial C}{\partial t} = D_y\frac{\partial^2 C}{\partial y^2} + D_z\frac{\partial^2 C}{\partial z^2} - V\frac{\partial C}{\partial x} + Q\delta(x)\delta(y)\delta(z-H) \tag{3.24}$$

Considering only the steady state solution, this becomes:

$$V\frac{\partial C}{\partial x} = D_y\frac{\partial^2 C}{\partial y^2} + D_z\frac{\partial^2 C}{\partial z^2} + Q\delta(x)\delta(y)\delta(z-H) \tag{3.25}$$

If the source point is excluded from the domain of the problem and instead including as a boundary condition, the Dirac delta functions can be left out of the differential equation:

$$V\frac{\partial C}{\partial x} = D_y\frac{\partial^2 C}{\partial y^2} + D_z\frac{\partial^2 C}{\partial z^2} \tag{3.26}$$

The boundary conditions imposed to solve Equation (3.25), along with the assumptions that the wind is parallel to $\hat{x}$ constant and that absorption and deposition are negligible, all simplify the system to an extent. The solution, given by Equation (3.27), has shown good agreement with experiment and has endured in the literature.

$$C = \frac{Q}{2\pi V\sigma_y\sigma_z}\exp\left(-\frac{1}{2}\frac{y^2}{\sigma_y^2}\right)\left[\exp\left(-\frac{1}{2}\frac{(z-H)^2}{\sigma_z^2}\right) + \exp\left(-\frac{1}{2}\frac{(z+H)^2}{\sigma_z^2}\right)\right] \tag{3.27}$$

where $\sigma_y^2 = 2xD_y/V$. For a known emission rate Q, windspeed V, and diffusion coefficients $\sigma_{y,z}$, Equation (3.27) can be solved for the ground level concentration of an effluent near a stack of height H.

Although Equation (3.27) can be used for initial calculations of the ground level ^{37}Ar concentration due to reactor releases, more sophisticated computational tools exists to provide more realistic estimates. The National Oceanic and Atmospheric Administration's (NOAA) Air Resources Laboratory developed and maintains the Hybrid Single-Particle Lagrangian Integrated Trajectory model (HYSPLIT). HYSPLIT adds a number of levels of sophistication to the simplified plume model, including

treatment of:

- atmospheric conditions such as three-dimensional wind
- plumes as hybridized particle/puff system
- absorption and dry/wet deposition

Rather than explicitly solving the diffusion-advection equation, HYSPLIT employs a hybrid treatment that independently calculates the trajectory of the puff or particle due to wind using Lagrangian mechanics and the random motion due to atmospheric turbulence through calculation of the vertical and horizontal mixing coefficients [57]. This approach can be implemented in two ways: the so-called "puff" model and the individual particle model.

In the puff model, the motion of the center of a "puff" due to advection is calculated using atmospheric data, then then expansion of the puff in x, y, and z due to diffusion is independently calculated. After a number of calculation time steps, the size of the puff will exceed the size of a grid cell on the meteorological grid used to map the motion. When this occurs, the puff will be split into multiple puffs whose trajectories are calculated separately. The total concentration is conserved among puffs. Puffs are intermittently released so that the average release rate matches the user-specified release rate.

In the particle model, the change in particle position due to advection is calculated identically to the puff method. Diffusion is treated differently, however. After the change in position due to advection is calculated for a time step, the change is position due to turbulence is calculated and simply added to the final position of the particle.

Although the puff model is computationally advantageous to explicit solution of the diffusion-advection equation, it underestimates the effects of wind shear on the

z-dependent concentration (if $\hat{z}$ is normal to the surface of the Earth). To account for this, the puff model is used to calculate diffusion in x and y, while the particle model in used for the z motion. The concentration at a location of interest within the model grid can then be requested by the user. Alternatively, a concentration contour map for a given altitude as a function of latitude and longitude can be produced.

3.6 Experiments

Validation of the MCNPX model of the NETL TRIGA relied on comparison of the model's output to results of experiments conducted both during this project and during previous work at the University of Texas. The following subsections describe the procedure for experiments conducted in the course of this project and provide details on the experiments previously conducted.

3.6.1 Flux Measurements

Flux monitor irradiation is a common technique for assessing the real neutron flux of an irradiation facility in a research reactor. A reference material of known composition is irradiated in the facility and the tracer isotopes are measured on a radiation detection system. The activation equations describing the irradiation can be solved to determine the flux necessary to produce the activity measured in the experiment. Two in-core flux mapping experiments were conducted to produce validation data: four vertically spaced cobalt wires in the 3L facility and four laterally spaced cobalt wires in the RSR facility.

The 3L facility is an in-core facility that occupies fuel positions E11, F14, and F15, indicated by the three empty elements in the lower right in Figure 3.4. Each

of four flux wires was placed in a small plastic vial and affixed to a rigid aluminum pole using Kapton tape. The vials were placed at heights of 24 cm, 32 cm, 60 cm, and 78 cm relative to the bottom of the pole. These positions correspond to heights of -6.2133 cm, 11.7867 cm, 29.7867 cm, and 47.7867 cm relative to the core midplane. Larger, empty plastic vials were affixed to the base of the aluminum pole to make the entire arrangement self-standing, and the base was inserted into a aluminum cup to prevent debris from collecting at the bottom of the 3L tube. The reactor was operated at 950 kW for 120 minutes and the irradiation facility was left for 72 hours after shutdown to allow for the decay of ^{28}Al activated in the pole. The samples were counted individually on a HPGe system. Energy and efficiency calibrations of the detector were accomplished experimentally using a liquid mixed gamma check source.

The RSR facility is a circular rack surrounding the upper part of the core. Typically the rack rotates samples around the core during irradiation to provide uniform flux to multiple samples, however the rack was kept stationary during the flux monitoring irradiation for this project. Each of four flux wires was placed in a small plastic vial (same as those used for the 3L irradiation) and the vials were placed in RSR positions 10, 20, 30, and 40. Position 40 was left directly under the RSR loading tube such that the line connecting positions 20 and 40 was parallel to BPs 1 and 5. Positions 10 and 30 were then parallel to BP3. The reactor was operated at 500 kW for 60 minutes. Samples were counted on the same HPGe detector system as the aforementioned 3L samples, and calculations relied on identical calibration and efficiency determinations.

The validation method compared the experimental flux, as determined by the activity of the irradiated wire, to the MCNPX-generated flux of the irradiation facil-

ity. The experimental flux was calculated using the standard activation equation:

$$\phi = \frac{\lambda C \left(\frac{C_r}{C_l}\right)}{(\gamma \varepsilon \sigma_\gamma N)\left(1 - e^{-\lambda t_i}\right)\left(e^{-\lambda t_d}\right)\left(1 - e^{-\lambda C_r}\right)} \tag{3.28}$$

where λ is the decay constant of ^{60}Co, C is the integrated total counts for the measurement, C_r is the real count time, C_l is the live count time, γ is the intensity of the decay mode, ε is the efficiency of the detector at the measured energy, σ_γ is the collapsed microscopic capture cross-section, N is the number of target atoms in the sample, t_i is the irradiation time, and t_d is the decay time.

More extensive flux characterization data of other reactor facilities was culled from reports of previous experiments at the NETL TRIGA and is described in detail in Section 5.

3.6.2 Concrete Irradiation

Concrete samples were prepared using NIST SRM 1888a, a powdered form of Portland Cement. As with all NIST SRMs, the elemental composition of the sample is verified in the Certificate of Analysis. The major components of the SRM (by weight percent) are given in Table 3.2. Initial experiments were conducted to determine the isotopic composition of the offgas of an irradiated SRM 1888a sample, to establish the experimental procedure, and to ensure the viability of measuring the samples using the Pacific Northwest National Laboratory (PNNL) ^{37}Ar measurement system.

For calculation of the theoretical number concentration of ^{37}Ar during the irradiation of cement/concrete, the activation matrix (see Subsection 3.1.1) accounted for the following:

- production of ^{37}Ar via (n,α) reactions in ^{40}Ca
- loss of ^{37}Ar through absorption reactions
- loss of ^{40}Ca through absorption reactions
- production of ^{37}Ar and ^{39}Ar through low-probability reactions in ^{39}K, ^{40}K, ^{41}K, and buildup in isotopes of S and Cl
- decay of all unstable species

Relevant isotopes in the matrix were chosen based on presence in Portland Cement and probability of being involved in a reaction that measurably affects the radioargon concentration. The relative contribution of activation of air in the void regions of the concrete are reported separately.

Table 3.2: Mass fraction composition of SRM 1888a, Portland Cement. Components with negligible contributions are not listed.

Component	Mass Frac. (%)
CaO	63.23±0.21
SiO_2	21.22±0.12
Al_2O_3	4.265±0.078
Fe_2O_3	3.076±0.058
MgO	2.982±0.067
SO_3	2.131±0.043
K_2O	0.526±0.010
Cl	0.0036±0.0007

A 0.202 g sample of SRM 1888a was mixed with 1 mL of water and left to set in the end cap of a Swagelok PTFE valve. After 72 hours of curing time, the end cap was re-attached to the valve which was then attached to a gas transfer manifold. Vacuum was pulled on the manifold and the valve for 24 hours until the pressure

of the system was < 5 mTorr. The valve was closed off such that vacuum was maintained in the end cap. The entire valve was irradiated in the 3L facility of the NETL TRIGA for 30 minutes at 500 kW. Following irradiation the sample was left to decay in the 3L facility for 18 hours to minimize external dose to the operators and experimenters from the relatively high specific activity Mn activation products.

A 100 cm^3 stainless steel bottle was attached to the gas transfer system and pumped down to a pressure of 5 mTorr, then removed from the manifold. Following the decay of the valve and cement sample, the valve was re-attached to the gas transfer manifold and the system was backfilled with natural-abundance stable argon gas to atmospheric pressure. The stainless steel bottle was attached to the manifold and opened to the argon filled region to allow for volumetric expansion of the cement off-gas and stable carrier gas into the bottle. Measurement of the sample was achieved by direct counting of the bottle on an HPGe system.

4 | Model and Code Validation

Validation of the reactor model relied on experimental data produced as part of this project, though a majority of high fidelity results used for validation were collected from previous experimental work conducted at the NETL TRIGA reactor. The following sections include a description of the data used for validation and the performance of the reactor model against that data. The details of the reactor model are given in Section 3.2 and the details of the validation experiments are given in Section 3.6.

Validation of the depletion code relied on analytical solutions to simplified buildup and decay equations, along with comparison against the results of the ORIGEN depletion code. The performance of the depletion code in relation to these sources of validation data is also discussed in this chapter.

4.1 Reactor Model Validation

4.1.1 Three-Element Irradiation Facility

The irradiated samples were cut to a length of 1 cm with masses from 6.3×10^{-3} g to 6.6×10^{-3} g. The reactor was operated on 1 February 2013 for 120 minutes at 950 kW and samples were removed the following day to allow for the decay of short lived aluminum isotopes. Post-irradiation activities, uncertainties, and the associated flux values for the flux monitor wires tested in the 3L facilities are given

in Table 4.1.

Table 4.1: Results of 3L irradiation of Al/Co flux wires. Positions values are on the centerline of the 3L canister relative to the core midplane.

Sample #	Position [cm]	Activity [Bq]	Total Flux ($\times 10^{12}$) [n $\cdot$ cm$^{-2} \cdot$ s^{-1}]	MCNPX Total Flux ($\times 10^{12}$) [n $\cdot$ cm$^{-2} \cdot$ s^{-1}]
1	-6.21	1073.6$\pm$16.5	11.0$\pm$0.18	17.0$\pm$0.19
2	11.79	765.6$\pm$11.5	7.84$\pm$0.13	9.89$\pm$0.15
3	29.79	168.4$\pm$2.6	1.94$\pm$0.03	1.93$\pm$0.06
4	47.79	24.5$\pm$0.45	0.277$\pm$0.006	0.28$\pm$0.02

The results of Table 4.1 show appreciable disagreement between the experimental flux and theoretical flux at the positions of samples 1 and 2. The source of this discrepancy is unknown, though it likely arose from incorrect measurement of the sample positions relative to the bottom of the 3L facility. The positions of samples 3 and 4 show agreement between the experiment and the model within 1%.

Recent experiments at the University of Texas at Austin to develop an experimental method for ^{37}Ar production through the activation of argon gas and/or ^{40}Ca included characterization of the 3L facility. Characterization was done by Egnatuk [58] using the same flux monitoring wires as were used for this project, although the wires in Egnatuk's experiment were placed lower in the 3L than the samples in this project. For that position in the Pb-lined 3L canister, the total flux was calculated to be approximately 1.3×10^{13} n $\cdot$ cm$^{-2} \cdot$ s^{-1}(flux value taken from plot of flux versus reactor power, table of exact values was not available). At the position of Egnatuk's sample, the MCNPX model calculated total flux is 1.25×10^{13} n $\cdot$ cm$^{-2} \cdot$ s^{-1}.

A more thorough characterization of the 3L facility was done by Aghara [59] in a dissertation at the University of Texas at Austin. Direct comparison data for the

950 kW irradiation using the Pb-lined 3L facility is not available in that report as the 3L facility in that project was in a different location in the reactor, the vertical flux profile and peak flux location compare favorably with the results of the MCNPX model in this work.

4.1.2 Rotary Specimen Rack

The irradiated samples were cut to a length of 1 cm with masses from 6.77×10^{-3} g to 7.71×10^{-3} g. The reactor was operated on 18 February 2013 for 60 minutes at 500 kW for the RSR irradiation, and the samples were removed from the reactor the following day to allow for decay of the short-lived aluminum isotopes. The RSR facility was held stationary during operation. The activities of the activated flux wires, along with the associated flux values for the irradiation positions, are given in Table 4.2. Sample 5, irradiated in position 10 of the RSR, was mislabeled after irradiation. Data for sample 5 is not reported.

Table 4.2: Results of RSR irradiation of Al/Co flux wires. RSR position 40 represents the region immediately below the loading tube. Position 20 is directly across the core region from position 40.

Sample #	Position RSR can #	Activity [Bq]	Flux ($\times10^{12}$) [$n \cdot cm^{-2} \cdot s^{-1}$]	MCNPX flux ($\times10^{12}$) [$n \cdot cm^{-2} \cdot s^{-1}$]
5	10	n/a	n/a	n/c
6	20	62.27±1.48	1.399±0.03	1.515±0.045
7	30	72.54±1.75	1.597±0.04	1.554±0.046
8	40	78.17±1.83	1.706±0.04	1.695±0.047

The results of the MCNPX model agree with the experimental result within a margin of 8% for position 20, within 2% for position 30, and within 1% for position 40. For the average thermal flux in the irradiation positions, the results of the model

and experiment agree within a margin of 2%.

Recent work by Graham [60] calculated the thermal and epithermal flux parameters of the NETL TRIGA reactor with a precision of 5-7% through the irradiation of flux monitor foils and wires in the RSR. The empirical results were integrated with radiation transport models of the reactor core and RSR to generate an experiment-based energy-dependent flux profile for the facility. The complete data set for the RSR flux, binned to 620 energy groups, was generously provided via personal correspondence by the author of Ref. [60]. The results were generated for a reactor power level of 950 kW and the experiments were conducted with the core in the same configuration modeled for this experiment, allowing for direct comparison of results. The group flux values are plotted in Figure 4.1. Statistical uncertainty for the calculated flux in both data sets displayed in Figure 4.1 is less than 1%.

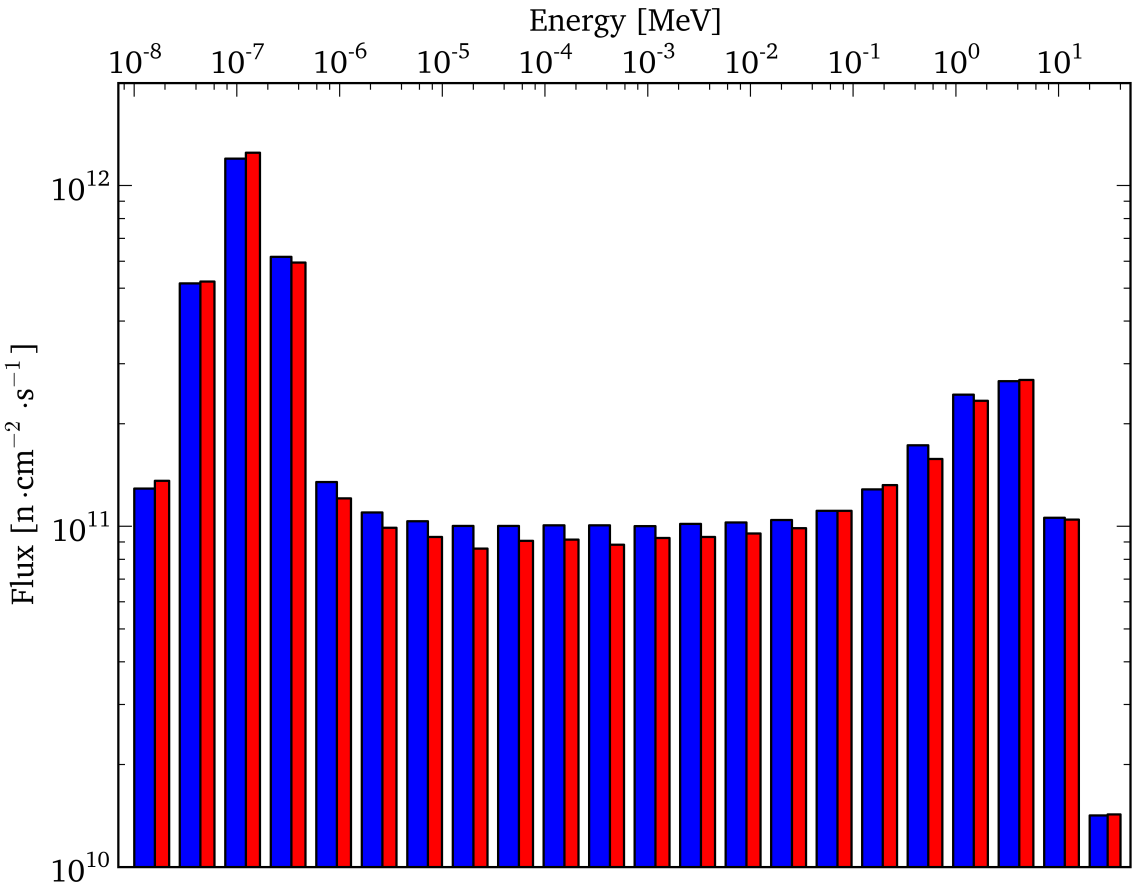

Figure 4.1: Experimental and modeled flux of the RSR facility at 950 kW. Blue indicates data from the reactor model, red indicates data from Ref. [60]. Uncertainty for both data sets is $< 1\%$ and error bars cannot be seen.

For thermal energy ranges, the modeled flux agrees with the empirical results of Graham within a margin of less than 6%. Epithermal fluxes agree within a margin of less than 15%, and fast neutron fluxes agree within 5%. The total fluxes agree within a margin of 2%.

Other previous experiments at the University of Texas included characterizations of the RSR facility which provide additional validation data. The dissertation work

of Braisted [61] empirically determined the RSR flux within the irradiation cans to be 3.44×10^{12} n $\cdot$ cm^{-2} $\cdot$ s^{-1} using flux wire irradiations. MCNPX calculations in the same report calculated a flux of 3.35×10^{12} n $\cdot$ cm^{-2} $\cdot$ s^{-1}. This experiment was conducted with the RSR rotation activated, so the flux wires were exposed to identical fluxes as a result of rotating around the reactor and represent an averaging of the flux in the stationary positions of Table 4.2. The average flux, based on the results of Table 4.2, agree with the experimental work of Braisted within a margin of 10% and with the computational work of Braisted within 7%.

4.1.3 Beamports

Experimental work for this project did not include validation measurements at the beamports. Characterization of individual beamports, including beam collimation, thermalization, gamma filtering, and other techniques employed at each facility was conducted by the previous experimenters. The flux values reported for each beamport facility were not standardized across previous projects. Some results focused on thermal profiles, others on the ratio of thermal flux to fast flux. The conditions of the individual experiments were recreated with moderate fidelity using the MCNPX model of the TRIGA. Comparison of the available results of previous experiments to those of the model are given in Table 4.3.

Experimental results for BP1 and BP4 were not found. MCNPX results for the total flux at the exit of those beamports are included in Table 4.3 for reference. Modeling of BP2 did not include the sapphire crystal of the Neutron Depth Profiling facility used to filter fast neutrons and gamma radiation. The thermal flux calculated by the model agreed with experimental results within a margin of 17%. It is likely that inclusion of the filtering apparatus of BP2 would reduce the flux calcu-

Table 4.3: Experimental and MCNPX-generated flux at the end of each beamport at 950 kW. * indicates thermal flux values.

Beamport #	Experimental Flux $n \cdot cm^{-2} \cdot s^{-1}$	Ref. #	MCNPX Flux $n \cdot cm^{-2} \cdot s^{-1}$
1	n/a	n/a	$(1.03 \pm 0.02) \times 10^{9}$
2*	1.24×10^{8}	[40]	$(1.45 \pm 0.05) \times 10^{8}$
3	n/a	n/a	n/a
4	n/a	n/a	$(2.05 \pm 0.06) \times 10^{8}$
5*	2.42×10^{6}	[44]	$(2.79 \pm 0.37) \times 10^{6}$

lated by the model and provide results closer to the experimental values. Experimental results for BP3 were only given at the sample position, requiring extensive modeling of the beam guide for which the necessary physics are not included in model. Much of the equipment for BP3 is installed permanently, so a representative flux at the end of the beamport excluding the equipment was not calculated. Modeling of BP5 included the Bi filter and the primary collimation equipment in the near-core stages of the beamport. BP5 values are calculated at the radiography sample positions 2 m outside the biological shield wall. Results for the model agree with the experimental data of Ref. [44] within 15%. More comprehensive modeling of the filtering and collimation system used for the radiography facility may have improved the agreement between model and experiment.

4.1.4 Concrete Irradiation

Measurements of the concrete sample following irradiation (but before off-gas collection) indicated that the expected long-lived activation products of the major constituents of the SRM were present, as indicated in Table 4.4.

Measurement of the off-gas sample, following the procedure detailed in Sec-

Table 4.4: Activity of the activation products in the SRM1888a sample. Only those products from the major components are reported.

Isotope	Activity [Bq]
^{24}Na	5.45×10^{4}
^{38}Cl	9.16×10^{1}
^{42}K	1.87×10^{4}
^{51}Cr	2.19×10^{4}
^{54}Mn	9.04×10^{1}
^{59}Fe	8.89×10^{2}
^{65}Zn	6.26×10^{2}

tion 3.6.2, yielded no spectral peaks above the measured background. The high-energy gamma ray of ^{41}Ar was not expected to be measured as a result of the long decay time between irradiation and counting. Other gaseous species likely to be in the original sample (radiooxygen, radionitrogen) have similarly short half-lives the preclude measurement at longer decay times. Radioactive isotopes of krypton were also not seen in the sample.

Arrangements for ^{37}Ar off-gas measurement were not made by the completion of the experiment. As a result, diffusion validation data was not available at the time of this report. Use of ^{41}Ar as a short-lived tracer for ^{37}Ar activation would be possible for an experiment with sufficiently low sample activity to allow for direct counting after irradiation.

4.2 Depletion Code Validation

Initial validation of the depletion routines was conducted by testing the response to a number of initial conditions. Validation included checks of the following responses, among others:

- No isotopes were created for a system with all isotopes at zero concentration
- No unstable species were created for a system with zero flux and only stable isotopes
- Stable isotopes did not decay
- Initial conditions were reflected in the initial time step
- All tracked isotopes were reported in the output file

Simple decay cases (at zero flux) for single isotopes were checked against analytical solutions to the time-dependent concentrations and agreed within an arbitrary level of precision. In order to test the simultaneous decay of parents and buildup of daughters, 1 Ci of the isotopes ^{37}Ar, ^{39}Ar, and ^{41}Ar were tracked along with their daughters ^{37}Cl, ^{39}K, and ^{41}K. The concentration of all six species was tracked for time steps that covered the complete decay (>7 half-lives) of ^{41}Ar, then ^{37}Ar, through to one half-life of ^{39}Ar. The concentrations calculated by the depletion code and by ORIGEN agreed within 1% for all tracked isotopes at all time steps. The highest discrepancy was 0.9%, with most differences existing at the $< 0.01\%$ level.

Direct validation of the buildup capabilities of the code using analytical solutions was not possible as a result of the intractable system of species and reactions modeled. Instead, secondary validation using ORIGEN was undertaken. The same system of stable argon isotopes as that used for the parent-daughter decay calculations, along with the radioargon isotopes, was tracked during an irradiation at constant flux using the depletion code and ORIGEN-ARP. The comparison of results could only be done semi-qualitatively. As mentioned, ORIGEN relies on pre-generated group constants for neutron flux profiles of specific LWR fuel assemblies. The flux

Table 4.5: Comparison of air activation results for an 8 h irradiation at 950 kW, as calculated by the depletion code and ORIGEN-ARP. Values are reported as the difference in number density between the two codes divided by the ORIGEN reported number density.

Isotope	δN [%]
^{36}Ar	< 0.1
^{37}Ar	7.66
^{38}Ar	< 0.1
^{39}Ar	10.6
^{40}Ar	< 0.1
^{41}Ar	4.68
^{37}Cl	7.44
^{39}K	10.6
^{41}K	4.99

profiles and group constants used in the depletion code were different than those in ORIGEN, and produced different results. The buildup and decay trends across the isotopes for both sets of codes could be compared, however, to assure that the depletion code was not generating erroneous results. Comparison results for Table 4.5 were generated using tabulated cross-sections for a 17x17 LWR fuel assembly.

Table 4.6: Computational uncertainty for a full-power irradiation in the 3L facility for 8 h. Standard deviation results represent only the variance produced by numerical methods of the depletion code.

	Mean Activity [Bq]	Std. Dev. [Bq]
^{37}Ar	1.889×10^{5}	1.903×10^{-8}
^{39}Ar	1.961×10^{0}	1.246×10^{-13}
^{41}Ar	9.312×10^{8}	8.225×10^{-5}

To flux match the codes as best as possible, the thermal flux scalar for a 17x17 LWR assembly (the only flux-related input for activation mode in ORIGEN-ARP) was adjusted until the ^{37}Ar buildup for the irradiation of a monoisotopic ^{36}Ar sample agreed with the results of the depletion code. With the flux scaled, a complete air sample was modeled in both codes. The time-dependent concentrations of the argon isotopes, ^{37}Cl, ^{39}K, and ^{41}K were tracked. The differences in output concentrations for an 8 hour irradiation are given in Table 4.5. Values for δN varied by $<$ 0.1% for results between 1 h and 24 h.

The cumulative effect of rounding errors and other computational uncertainties was determined by running the depletion code for a large number of identical cases with no variance in the input values. The standard deviation in the calculated activities of the radioargon isotopes from only these computational uncertainties are presented in Table 4.6.

5 | Results

The following sections present the results produced by the depletion calculation code in conjunction with radiation transport model. Results for the in-core sources and the ex-core sources are presented first, followed by the results for other sources identified during the course of the research. Results are presented with a focus on ^{37}Ar, however the buildup of other radioargon isotopes is calculated and presented where prudent. Following the characterization of the individual facilities are the results of sensitivity studies for a variety of operational and methodological parameters. A summary of these results is provided in Chapter 8.

The reactor model and depletion codes allowed for the calculation of radioargon buildup for an arbitrary operation regime: any variation on reactor power and reactor runtime could be explored. In the interest of standardization, most results are presented for full power (950 kW) operation over an 8 hour operating day. This approach allows for relatively simple scaling of the results for other power levels and for shorter run times. Some of these sensitivities to reactor power and operating history are discussed in Chapter 7.

5.1 Uncertainty

Variance in radiation transport results were produced by MCNPX itself and are reported directly with the associated MCNPX fluxes. The total uncertainty associated with specific experimental results or model validation were calculated based

on propagation of individual uncertainties in the following:

- Reactor power
- Sample mass
- Irradiation, decay, and count times
- Counting statistics of sample measurement
- Efficiency calibration of the detector system

Uncertainties in empirical and simulated flux values, including the sources listed above, are reportedly directly with the result. The uncertainties associated with the results of the depletion code included uncertainties in the MCNPX-generated flux profiles along with the following sources:

- Conversion of MCNPX results to dimensions of $[\text{n} \cdot \text{cm}^{-2} \cdot \text{s}^{-1}]$
- Multigroup calculations
- Initial concentration of stable isotopes
- Geometry of irradiation regions

The uncertainty in these items was calculated manually based published variances of physical constants used for conversion [62] and tolerances for the design of reactor facilities. Where no published uncertainty information was available for a particular value, conservative estimates were made.

The depletion code required a number of linear algebraic operations, as detailed in Section 3.1.1, for which there was not an analytical procedure for rigorously propagating error. In order to provide an estimate of the variance in the result due

to known uncertainties, the error in the calculations was treated empirically. For the values used in the eigenvalue decomposition described in Section 3.1.1, the known variance was used to generate a normal distribution of input values. These values were iteratively sampled by the depletion code to generate a set of output values. The standard deviation in the set of output values was considered the uncertainty for subsequent computational steps. Uncertainty values for a representative calculation of buildup in the 3L facility are given in Table 5.1.

Table 5.1: Uncertainty in modeled ^{37}Ar buildup for a full-power irradiation in the 3L facility for 8 h.

	Mean Activity [Bq]	Std. Dev. [Bq]	Std. Dev. %
^{37}Ar	1.889×10^{5}	8.42×10^{3}	4.43
^{39}Ar	1.961×10^{0}	8.316×10^{-2}	4.21
^{41}Ar	9.312×10^{8}	3.831×10^{7}	4.08

For results produced by the depletion code, there was an additional source of uncertainty that was not included in the calculation. Although uncertainty in evaluated nuclear cross-section data is often not propagated in the result of a depletion calculation, if reported at all, the Low-Fidelity Covariance Project [63] has developed estimates of the variance in evaluated nuclear data files that can be used to estimate uncertainty in cross-section data. Covariance data for the cross-sections treated in the depletion code was not published in the data sets, so the Low Fidelity data represented the only estimate of cross-section uncertainty applicable to this work. Data from this project was acquired by the author for the radiative capture reactions in the stable argon isotopes. The thermal energy range of Figure 3.1 is reproduced in Figure 5.1 with the associated uncertainties.

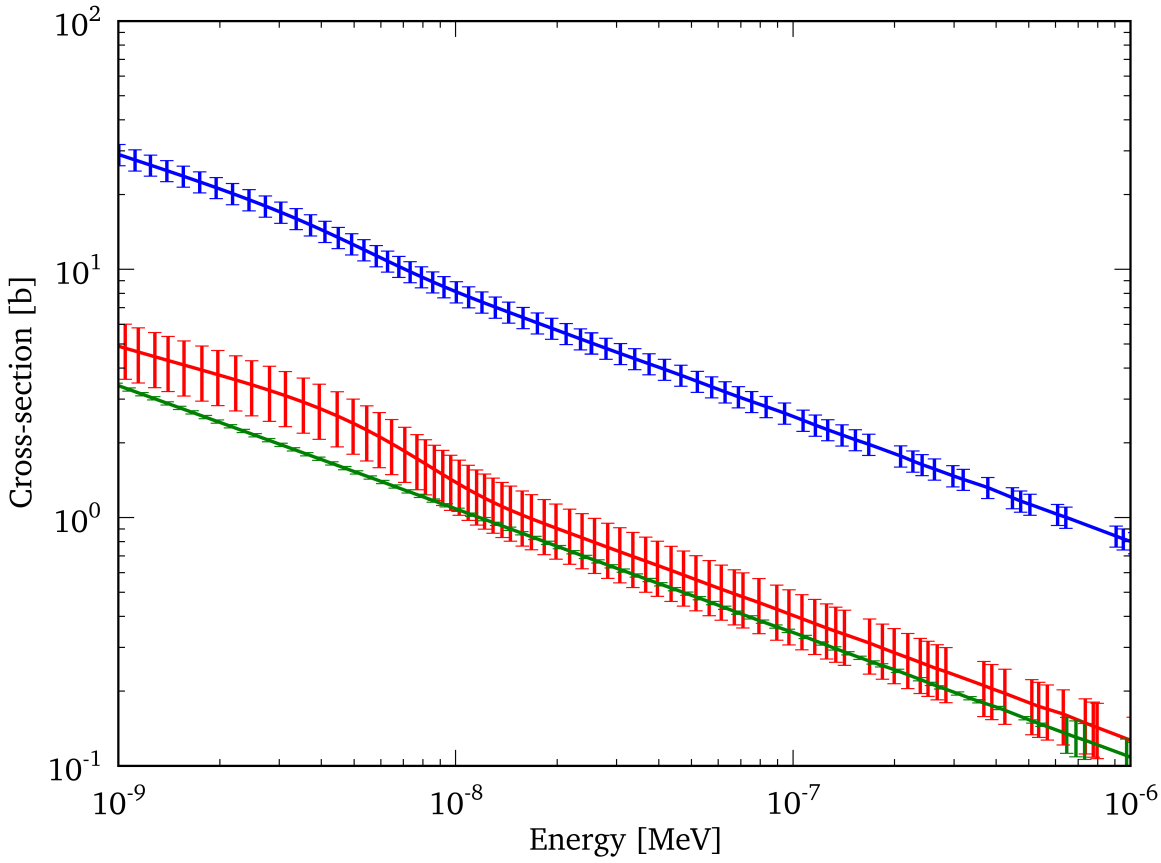

Figure 5.1: Cross-sections and associated uncertainty for ^{36}Ar(n,γ)^{37}Ar (in blue), for ^{38}Ar(n,γ)^{39}Ar (in red), and for ^{40}Ar(n,γ)^{41}Ar (in green).

5.2 In-Core Sources

5.2.1 Three-Element Facility

The 3L is backfilled with CO_2 during typical operations, so radioargon buildup in practice is negligible. These calculations are provided for completeness, but 3L is not considered as part of the cumulative buildup in the entire reactor facility.

Results were achieved using 3.29×10^7 particle histories distributed over 300 KCODE cycles with neutron weight windowing enabled. The complete volume and geometry of the 3L facility was modeled. Initial radioargon concentrations were chosen as the composition of air at STP, with the stable isotopes ^{36}Ar, ^{38}Ar, and ^{40}Ar as the only species present at the beginning of the irradiation. The activities of the unstable isotopes ^{37}Ar, ^{39}Ar, and ^{41}Ar in the 3L during an 8 hour operation at 950 kW are shown in Figure 5.2 and the values are given in Table 5.2. Uncertainties for the 8 hour activity are 4.43%, 4.21%, and 4.08% (as reported in Section 5.1), respectively.

The total calculated flux of the 3L facility was $(9.576\pm0.01)\times10^{12}$ n $\cdot$ cm$^{-2}\cdot$ s^{-1}. The energy dependent flux profile is shown in Figure 5.3.

As has been previously mentioned, the 3L facility is typically backfilled with a neutral gas (CO_2 or N_2) to avoid the buildup of ^{41}Ar that would subsequently be released to the atmosphere. As a result, the 3L activities were not accounted for when calculating the total reactor inventory. The results were produced in the interest of exploring the expected activity of radioargon isotopes in a large, air-filled, in-core irradiation facility.

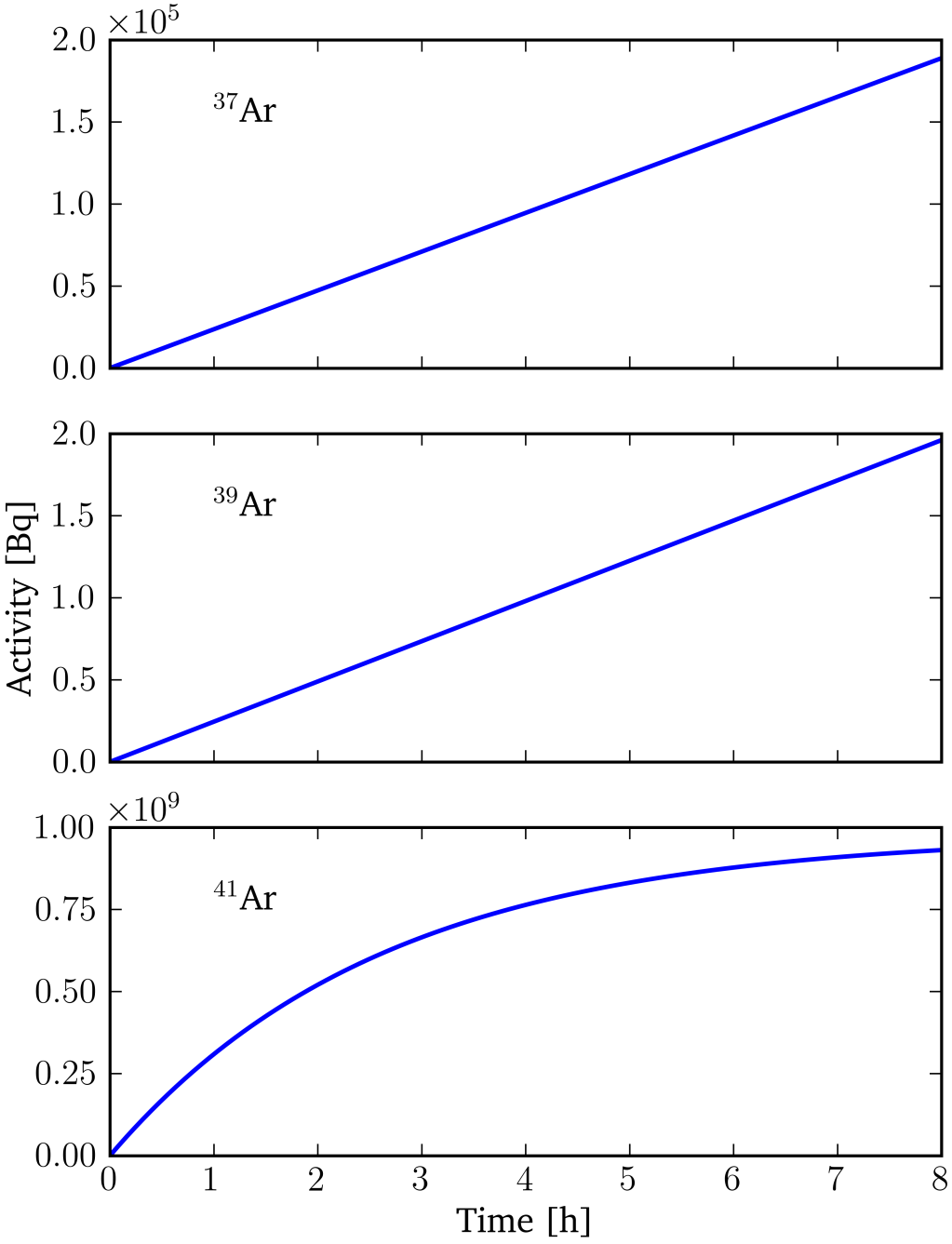

Figure 5.2: Activitiy of ^{37}Ar (top), ^{39}Ar (center), and ^{41}Ar (bottom) in the 3L facility during an 8 h irradiation at 950 kW.

It is apparent that for the longer-lived isotopes ^{37}Ar and ^{39}Ar, the buildup is roughly linear in time due to the short irradiation time and low concentration compared to the target isotope (so the nonlinear effect of loss by absorption is negligible). Considering the linear relationship between reactor power and the magnitude of the flux, it is possible to estimate buildup constants to describe the radioargon activity as a function of power and irradiation time. Linear regression on the time-dependent activity for each isotope gave the constants reported in Table 5.3.

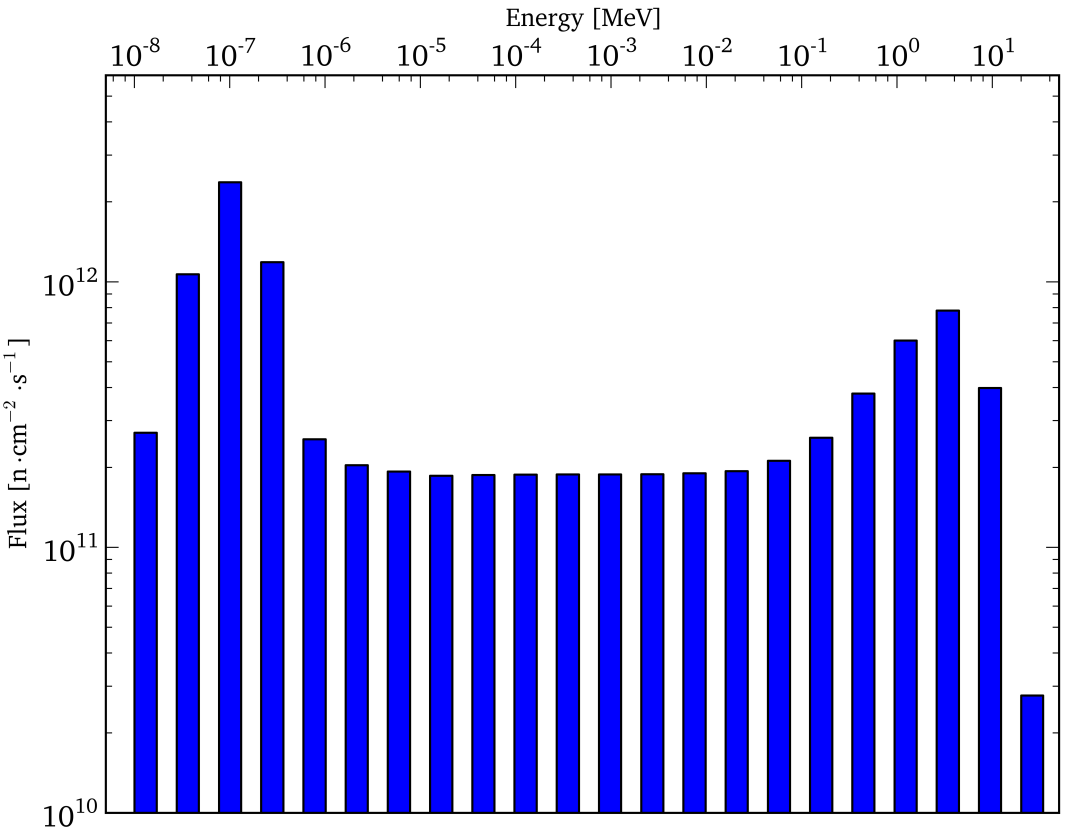

Figure 5.3: Group flux of the 3L facility at 950 kW. Uncertainty in the MCNP-generated results are too small for error bars to be legible on the figure.

Table 5.2: Activity of the radioargon isotopes in the 3L during an 8 h irradiation at 950 kW.

Time [h]	^{37}Ar $\times 10^{4}$ [Bq]	^{39}Ar $\times 10^{-1}$ [Bq]	^{41}Ar $\times 10^{8}$ [Bq]
1.0	2.368±0.10	2.451±0.10	3.094±0.13
2.0	4.734±0.21	4.903±0.21	5.209±0.21
3.0	7.098±0.31	7.354±0.31	6.655±0.27
4.0	9.460±0.42	9.805±0.41	7.643±0.31
5.0	11.82±0.52	12.26±0.52	8.319±0.34
6.0	14.18±0.63	14.71±0.62	8.781±0.36
7.0	16.53±0.73	17.16±0.72	9.097±0.37
8.0	18.89±0.84	19.61±0.83	9.312±0.38

Table 5.3: Buildup constants for radioargon in the 3L when air-filled, assuming the irradiation time is much less than the half-life for each isotope and that initial concentrations are minimal.

	^{37}Ar	^{39}Ar
Bq·kWh^{-1}	(2.4874±0.19)$\times 10^{1}$	(2.58±0.21)$\times 10^{-4}$

As a result of building through the double capture chain from ^{40}Ar, the initial buildup of ^{42}Ar is nonlinear, so no constant was estimated. The short half-life of ^{41}Ar also precluded estimating a buildup constant.

5.2.2 Rotary Specimen Rack

Results were achieved using 3.29×10^{7} particle histories distributed over 300 KCODE cycles with neutron weight windowing enabled to maximize the number of particle histories scoring in the tally region. The entire RSR geometry and volume was included in the calculation. Initial radioargon concentrations were chosen as the composition of air at STP, with the stable isotopes ^{36}Ar, ^{38}Ar, and ^{40}Ar as the only

species present at the beginning of the irradiation. The activities of the unstable isotopes ^{37}Ar, ^{39}Ar, and ^{41}Ar in the RSR during an 8 hour operation at 950 kW are shown in Figure 5.4 and the values, including and ^{42}Ar activities, are given in Table 5.4. The total calculated flux of the RSR facility was (4.45±0.003)×10^{12} $n \cdot cm^{-2} \cdot s^{-1}$. The energy dependent flux profile is shown in Figure 4.1.

Table 5.4: Activity of the radioargon isotopes in the RSR during an 8 h irradiation at 950 kW.

Time [h]	^{37}Ar ×10^{4} [Bq]	^{39}Ar ×10^{-1} [Bq]	^{41}Ar ×10^{8} [Bq]
1.0	1.15±0.05	1.19±0.05	1.50±0.06
2.0	2.30±0.10	2.37±0.11	2.53±0.10
3.0	3.44±0.15	3.56±0.16	3.23±0.13
4.0	4.59±0.20	4.74±0.21	3.71±0.15
5.0	5.73±0.25	5.93±0.27	4.04±0.17
6.0	6.87±0.30	7.12±0.32	4.26±0.18
7.0	8.02±0.35	8.30±0.37	4.41±0.18
8.0	9.16±0.40	9.49±0.42	4.52±0.19

Buildup constants for ^{37}Ar and ^{39}Ar production in the RSR, based on the same regression approach for the 3L, are given in Table 5.5.

Table 5.5: Buildup constants for radioargon in the RSR, assuming the irradiation time is much less than the half-life for each isotope and that initial concentrations are minimal.

	^{37}Ar	^{39}Ar
$Bq \cdot kWh^{-1}$	(1.20±0.05)×10^{1}	(1.25±0.06)×10^{-4}

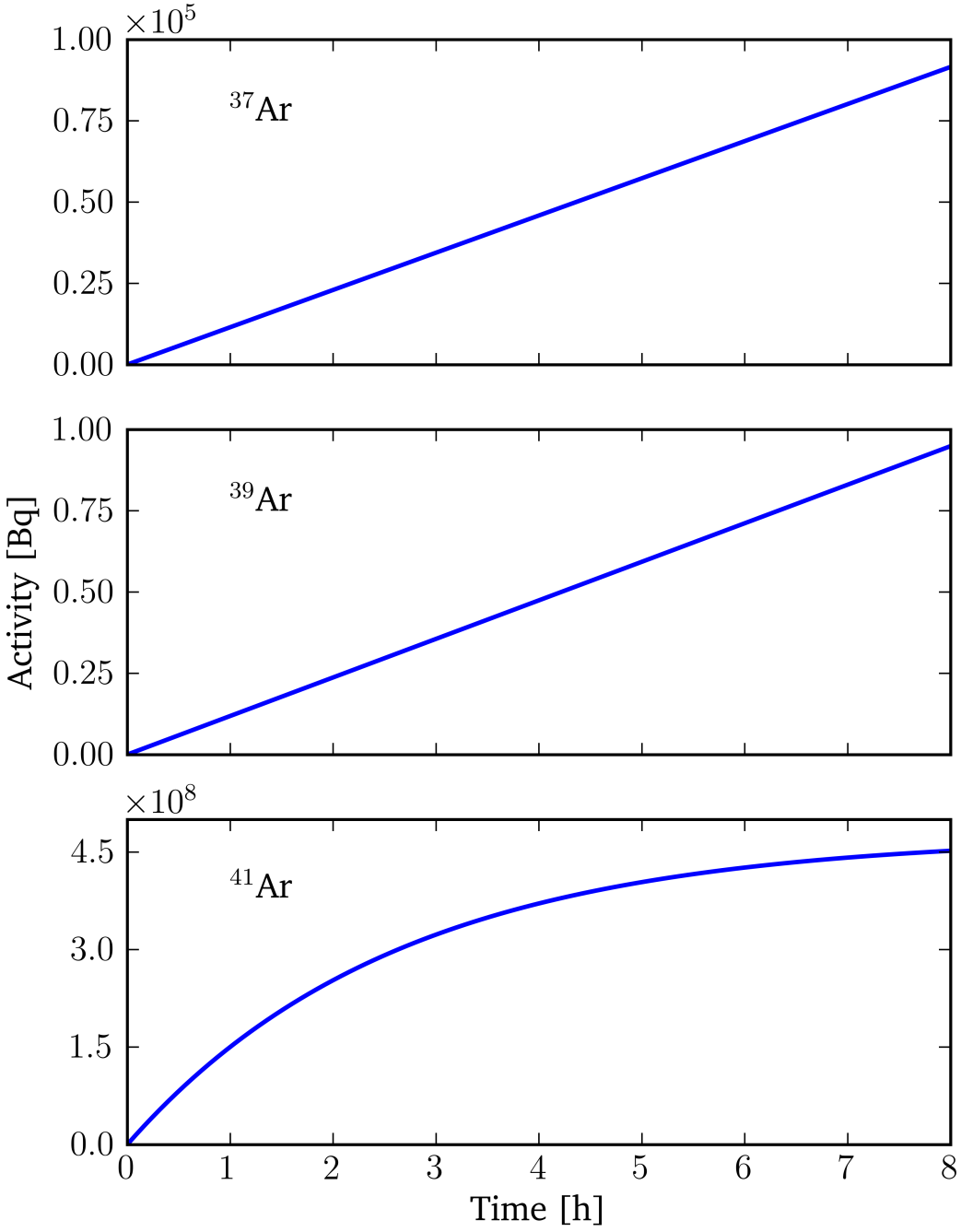

Figure 5.4: Activitiy of ^{37}Ar (top), ^{39}Ar (center), and ^{41}Ar (bottom) in the RSR facility during an 8 h irradiation at 950 kW.

5.2.3 Pneumatic Transfer System

Similar to the 3L, the 3L is backfilled with CO_2 during typical operations, so radioargon buildup in practice is negligible. These calculations are provided for completeness, but PTS is not considered as part of the cumulative buildup in the entire reactor facility.

Identical initial conditions were used for depletion calculations in the pneumatic transfer system sample tube. Results were achieved using 3.29×10^7 particle histories over 300 scored KCODE cycles. The PTS transfer tube extends a substantial distance above the reactor core into the pool where it penetrates the biological shield and runs from the reactor bay to the laboratory where PTS samples are prepared. The relatively small volume of the air-filled regions of the PTS and the volume of moderator between the upper regions of the transfer tube and the core limited the height at which the model could produce reasonable statistics in a reasonable amount of time. A cutoff height of 50 cm relative to the core midplane was chosen after confirming that inclusion of additional length of the tube had negligible effect on the calculated radioargon production rate. The group flux profiles of the PTS air cavity and air sleeve around the sample tube are shown in Figure 5.5.

One expected effects is clearly seen in Figure 5.5: the thermal flux of the air cavity is highly suppressed, relative to the air sleeve outside the sample cavity, as a result of the cadmium liner. The total flux inside the sample cavity was calculated to be $(4.237\pm0.01)\times10^{12}$ n $\cdot$ cm^{-2} $\cdot$ s^{-1}.

The activities of the unstable isotopes ^{37}Ar, ^{39}Ar, and ^{41}Ar in the PTS during an 8 hour operation at 950 kW are given in Table 5.6. Buildup constants for ^{37}Ar and ^{39}Ar production in the RSR are given in Table 5.7.

Table 5.6: Activity of the radioargon isotopes in the PTS during an 8 h irradiation at 950 kW.

Time [h]	^{37}Ar $\times 10^{3}$ [Bq]	^{39}Ar $\times 10^{-2}$ [Bq]	^{41}Ar $\times 10^{7}$ [Bq]
1.0	0.543±0.02	0.556±0.02	0.714±0.03
2.0	1.085±0.05	1.112±0.05	1.202±0.05
3.0	1.627±0.07	1.668±0.07	1.536±0.06
4.0	2.168±0.10	2.224±0.09	1.764±0.07
5.0	2.709±0.12	2.780±0.12	1.920±0.08
6.0	3.250±0.14	3.336±0.15	2.027±0.09
7.0	3.790±0.17	3.892±0.17	2.100±0.09
8.0	4.329±0.19	4.448±0.19	2.150±0.09

Table 5.7: Buildup constants for radioargon in the PTS, assuming the irradiation time is much less than the half-life for each isotope and that initial concentrations are minimal.

	^{37}Ar	^{39}Ar
Bq·kWh^{-1}	(5.69±0.12)$\times 10^{-1}$	(5.89±0.16)$\times 10^{-6}$

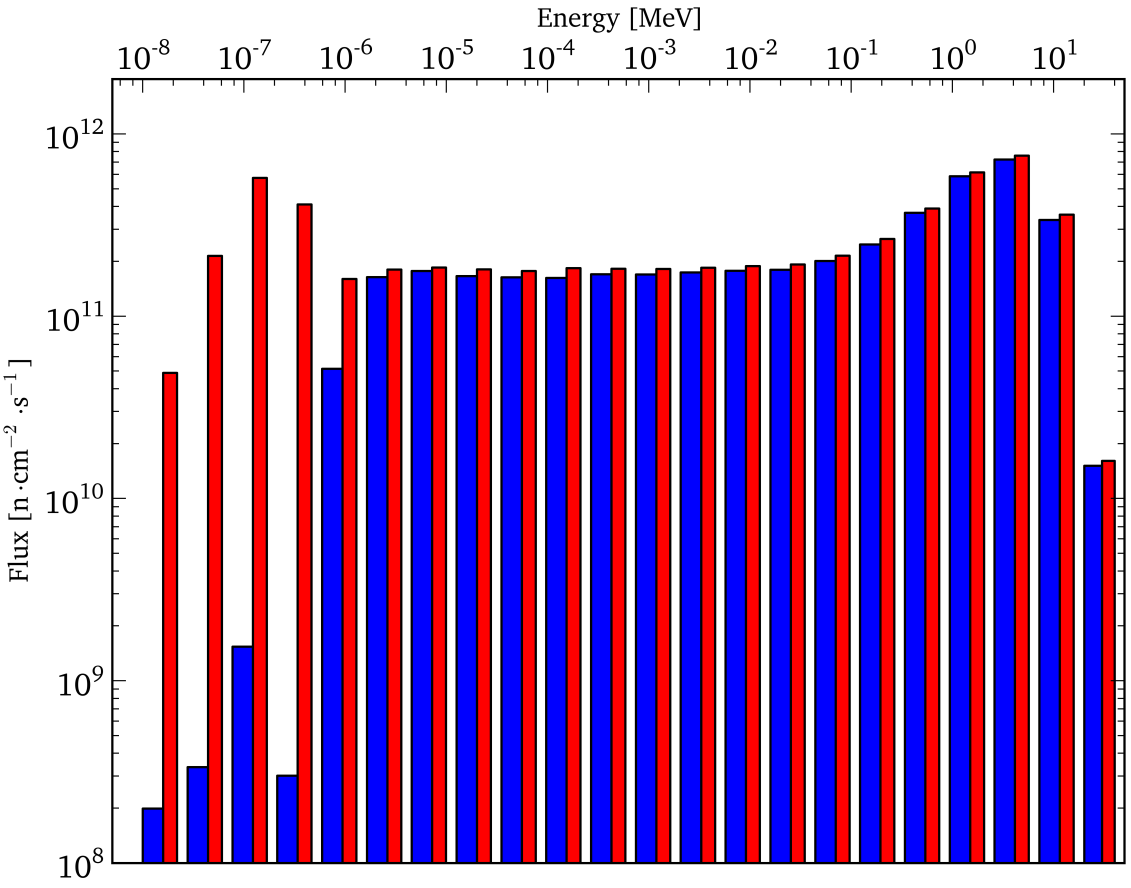

Figure 5.5: Group flux of the air-filled regions of the pneumatic transfer system (PTS) at 950 kW. Blue indicates the primary air cavity of the PTS where samples are contained, red indicates the sleeve of air between the sample tube and transfer tube. Uncertainty in the MCNP-generated results are too small for error bars to be legible on the figure.

5.3 Ex-Core Sources

5.3.1 Beamports

Results for the beamports were initially generated with each beamport modeled from core to biological shield with inclusion of only the collimation and filtering equipment that would affect the thermal neutron flux or the effective volume of air in the facilities. Volume tally results were limited by the poor statistics in modeling the entirety of the reactor geometry, so point detector tallies were used in conjunction with weight windowing where necessary. Typical results were generated with 1.5×10^7 particle histories. The buildup of radioargon was calculated for each stage of each beamport, however results consolidate the buildup for each beamport. The activity in the beamports for 8 hour operation at full power is given in Table 5.8.

Table 5.8: Activity of the radioargon isotopes in the beamports after an 8 h irradiation at 950 kW.

Beamport #	^{37}Ar $\times10^5$ [Bq]	^{39}Ar $\times10^0$ [Bq]	^{41}Ar $\times10^8$ [Bq]
1	8.95±0.60	9.28±0.70	44.2±3.00
2	1.23±0.07	1.27±0.08	6.05±0.40
3	7.73±0.33	8.02±0.31	38.2±1.70
4	1.02±0.04	1.06±0.05	5.02±0.23
5	4.99±0.22	5.18±0.24	2.47±0.11

BP1 and BP4 results modeled empty beamport tubes to reflect the state of those facilities as of December 2012. BP2 results accounted for the reduced volume of the second stage of the beamport tube as a result of beam collimation equipment. The filtering equipment in BP2 is designed to have minimal effect on the thermal flux and was not accounted for in the results [64]. BP3 results accounted for the reduced

volume of the third and fourth stage of the beam tube as a result of equipment for the Texas Cold Neutron Source. The BP5 model included the major components of the neutron radiography collimation system and BP5 results accounted for the reduced volume of the second, third, and fourth stages of the beam tube as a result of collimation equipment.

Table 5.9: Buildup constants for ^{37}Ar and ^{39}Ar in the beamport facilities.

Beamport #	^{37}Ar [Bq·kWh^{-1}]	^{39}Ar [Bq·kWh^{-1}]
1	$(1.18\pm0.08)\times10^{2}$	$(1.22\pm0.09)\times10^{-3}$
2	$(1.61\pm0.09)\times10^{1}$	$(1.68\pm0.10)\times10^{-4}$
3	$(1.02\pm0.04)\times10^{2}$	$(1.05\pm0.04)\times10^{-3}$
4	$(1.34\pm0.06)\times10^{1}$	$(1.39\pm0.07)\times10^{-4}$
5	$(6.57\pm0.28)\times10^{1}$	$(6.81\pm0.32)\times10^{-4}$

5.3.2 Pool Water

Results for radioargon buildup due to the activation of air in water relied on the initial composition calculated in Section 3.3. Initial attempts to map the pool with mesh tallies (three-dimensional tallies overlayed on the problem geometry) or with point detector tallies were unable to produce acceptable statistics. Results were ultimately produced with coarse segmenting of the pool regions in and around the reactor core. The pool was divided into the following five concentric cylindrical regions that extended along the core axis:

- The innermost region that encompassed the fuel and inner shroud
- The region between the outer shroud and the inner shroud
- Three divisions of the water between the outer shroud and the pool liner

The arrangement of the radial divisions is indicated in Figure 5.6.

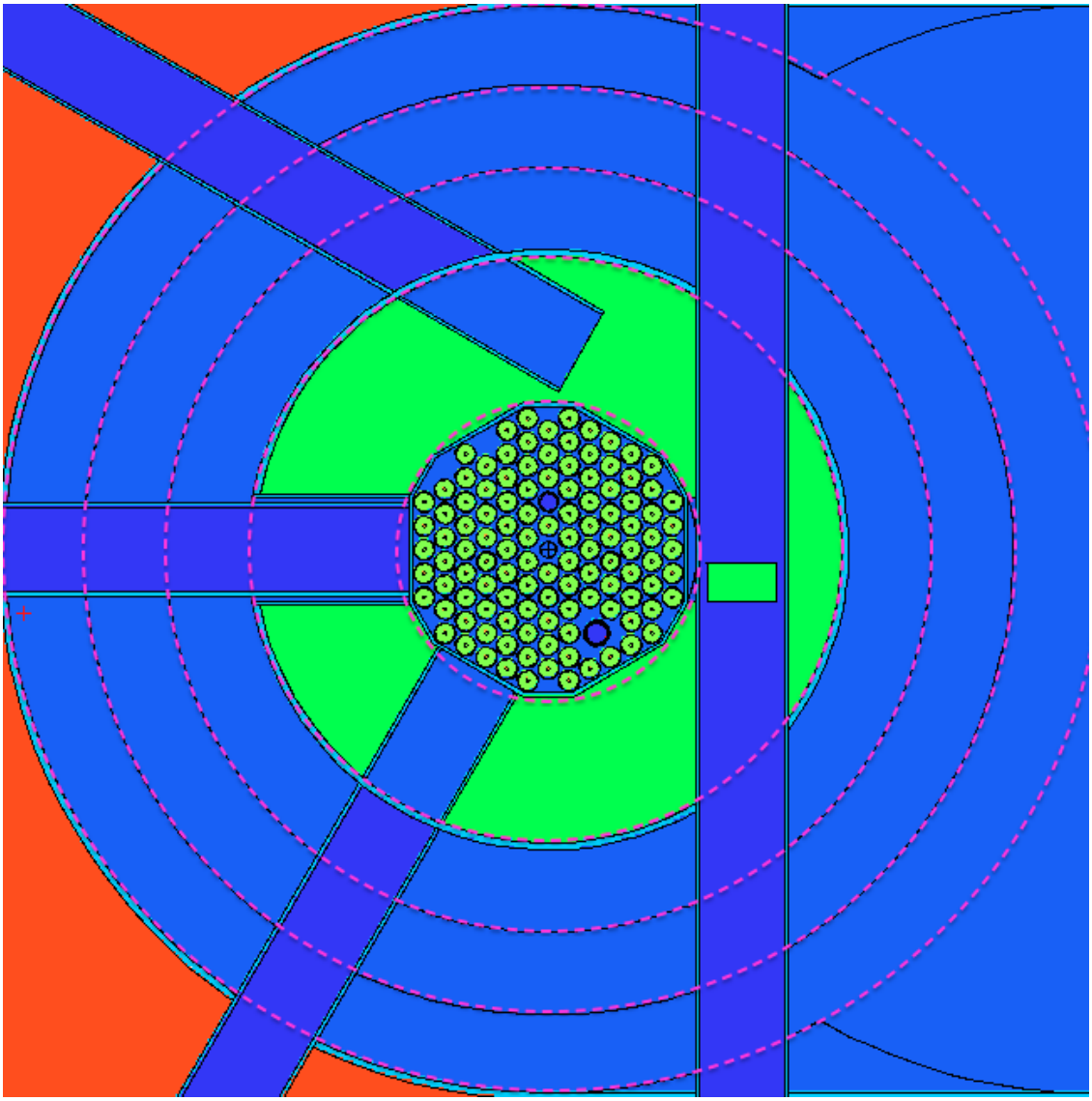

Figure 5.6: Radial segments of the reactor pool used for cell-based flux tallies. Segments are indicated by the dashed purple line and extend the full axial height of the transport model geometry.

Each cylinder was segmented into layers along the core axis for tallying. In total, the reactor pool was divided into 37 discrete regions for flux tallying. Individual

simulations were run for each region. The total buildup for the pool is shown in Figure 5.7.

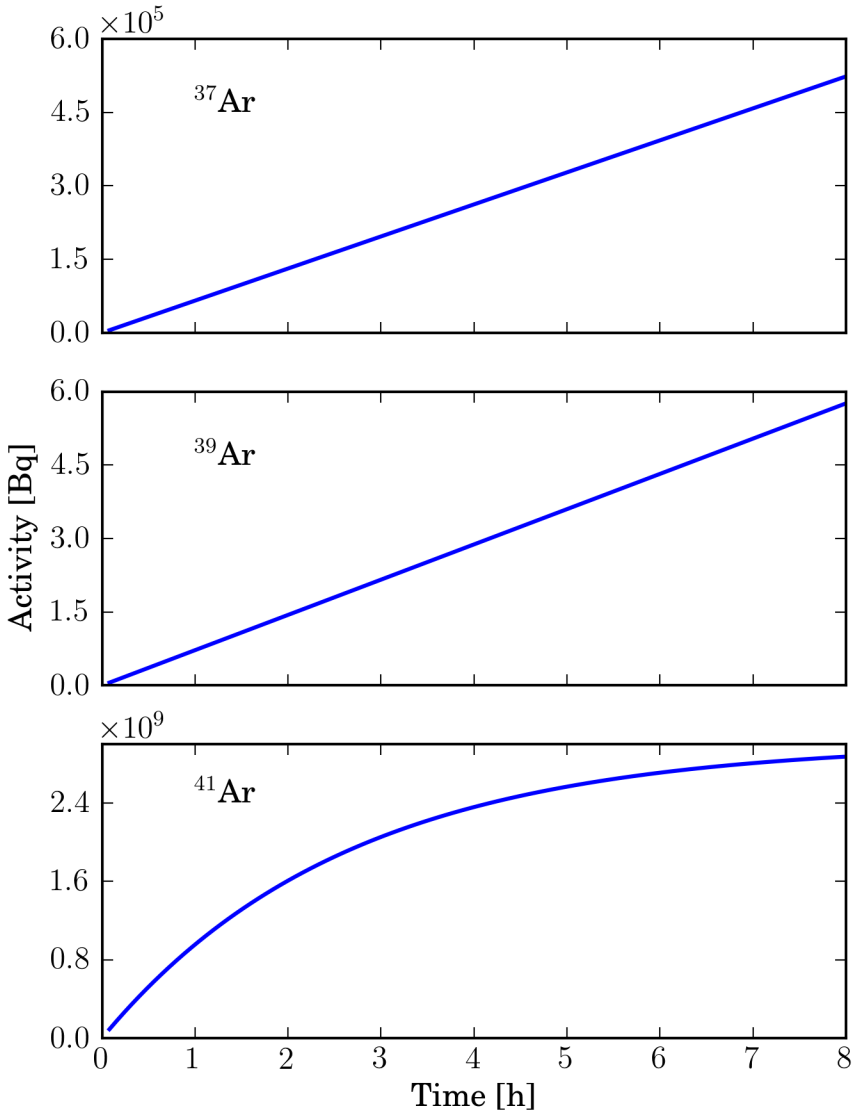

Figure 5.7: Activitiy of ^{37}Ar (top), ^{39}Ar (center), and ^{41}Ar (bottom) in the reactor pool during an 8 h irradiation at 950 kW.

Figure 5.7 indicates that the radioargon inventory in the pool is comparable to the cumulative buildup in the beamport facilities. Based on the time-dependent buildup of the radioargon isotopes, buildup constants were calculated for the reactor pool and are given in Table 5.10.

Table 5.10: Buildup constants for radioargon in the reactor pool, assuming the irradiation time is much less than the half-life for each isotope and that initial concentrations are minimal.

	^{37}Ar	^{39}Ar
Bq·kWh^{-1}	$(6.89 \pm 0.31) \times 10^{1}$	$(7.58 \pm 0.36) \times 10^{-4}$

As mentioned, the total buildup in the reactor pool was calculated using concentric cylindrical regions around the core which were then segmented vertically. Analysis of buildup in the individual regions made it possible to estimate the effective region where buildup is occurring beyond which the contribution to the total radioargon is negligible. These results indicate that 46.71% of the buildup occurs in the active fuel region inside the inner shroud, above the bottom plate and below the top plate. 96% of the buildup occurs within a region defined by a cylinder of radius 70 cm that extends 50 cm below and 50 cm above the core midplane. 99.5% of the buildup occurs within the region defined by the cylinder of radius 85 cm that extends 70 cm below and 70 cm above the core midplane. For reference, the nearest walls of the biological shield are 99.06 cm from the core centerline and the reactor pool floor is 97.185 cm below the core midplane.

Based on the constant buildup rate calculated in Table 5.10, a system describing simultaneous buildup in the reactor pool and release from the top of the pool was solved. The off-gas rate values given in Section 3.3 were used and calculations assumed that, due to the circulation from the water pumps, the pool is well-mixed

such that the radioargon is evenly distributed through the volume. The results of previous sections indicate that, for even high neutron fluence, the buildup of ^{37}Ar can be treated linearly. This allows for analytical solution to the concentration of the isotope in the pool and diffusion out of the pool for both the irradiation period and the subsequent shut down period.

Let N represent the activity of ^{37}Ar in the pool and M represent the activity released into the bulk air of the reactor facility. For a buildup rate K in dimensions of Bq·s^{-1}, the activity in the pool is:

$$\frac{dN}{dt} = K - J \tag{5.1}$$

where J represents the diffusive flux out of the pool given in Section 3.3. Based on this convention, $\varphi = N/V$ where V is the volume of the pool. Consolidating V and the other coefficients of Equation (3.9), along with the ^{37}Ar decay constant, into the coefficient C gives:

$$\frac{dN}{dt} = K - CN \tag{5.2}$$

Given that the buildup K is constant, the solutions for $N(t)$ are:

$$\begin{aligned} N(t) &= \frac{K}{C}\left(1 - e^{-Ct}\right), \text{ during operation} \\ N(t) &= N_i e^{-Ct_d}, \text{ after shutdown} \end{aligned} \tag{5.3}$$

where N_i is the activity at the end of operation and t_d is the time since shutdown.

Similarly, the total activity M released to the bulk air from offgassing is given by:

$$M(t) = Kt + \frac{K}{C}\left(e^{-Ct} - 1\right), \text{ during operation}$$
$$M(t) = M_i + N_i\left(1 - e^{-Ct_d}\right), \text{ after shutdown} \quad (5.4)$$

These solutions were used to determine the effect of the off-gassing behavior on the total release. Of primary interest is fraction of ^{37}Ar that is released to the bulk air of the facility prior to decay. This fraction determines the amount of ^{37}Ar released as effluent relative to the amount produced in the pool.

For the test case of 950 kW operation for 8 hours, 5.5% of the ^{37}Ar inventory is released from the pool by the end of irradiation. Based on the total buildup of 5.234×10^5 Bq ^{37}Ar as shown in Figure 5.7, 4.946×10^5 Bq of ^{37}Ar are still in the pool at the time of shutdown.

Calculation of the equilibrium concentration indicates that only 0.32% of the ^{37}Ar decays prior to release as an effluent; the remaining 99.68% is released as effluent. This equilibrium value is reached approximately 18 days after shutdown. Although the off-gassing mechanism limits the effluent release rate of pool-generated ^{37}Ar, almost the entire inventory is released prior to decay under these conditions. For combinations of reactor power and run time less than 950 kW for 8 h, the released fraction exceeded 99.68%.

5.3.3 Biological Shield

Results for radioargon buildup in the concrete in the biological shield required the most computation time and sophistication of all the tradiaitional sources investigated. Tranport of neutrons to the biological shield required weight windowing

for each segmented volume used to calculate the flux at the inward faces of the shield. The particle histories required for acceptable statistics typically exceeded 1×10^8. The number density of the target isotopes on interest (primarily ^{40}Ca) were calculated based on the composition of high-density magnetite concrete. The contribution to the total buildup from activation of the air content of concrete is discussed later in this section.

Initial flux calculations were generated at the shield-pool water interface at the height of the core midplane. This region was chosen to gauge the maximum neutron flux reaching the interface and to compare to results of previous work on TRIGA reactors. Ref. [65] found a boundary neutron flux on the order of 1×10^9 n·cm^{-2}·s^{-1} for full power operations of the TRIGA reactor at the Atominstitut in Vienna, which has comparable design and dimensions to the NETL TRIGA. Scaled to the 250 kW power of the Atominstitut reactor, the MCNPX model indicates a boundary flux of $(1.381\pm0.02)\times10^9$ n$\cdot$cm$^{-2}\cdot$s^{-1} for the corresponding location in the NETL TRIGA. Both results were generated for the nearest boundary of the pool and biological shield at the height of the core midplane.

Tallying within the biological shield was achieved by division of the shield into five regions, arranged relative to the center of the reactor core. Two regions encompassed the portions of the shield outside the two half-cylinders that define the reactor pool, two regions accounted for the portions along the flat sides of the reactor pool, and one region accounted for the concrete below the bottom of the pool. These regions were further subdivided such that the flux profile was calculated for 47 discrete regions of the shield. Based on results for buildup on the reactor pool, the model only simulated the region of the biological shield between +1 m and -1.5 m relative to the core midplane. Buildup beyond these boundaries was found to be minimal relative to regions nearer the core, and inclusion of these regions imposed

significant computational expense on the simulation.

The buildup of radioargon in the biological shield is shown in Figure 5.8.

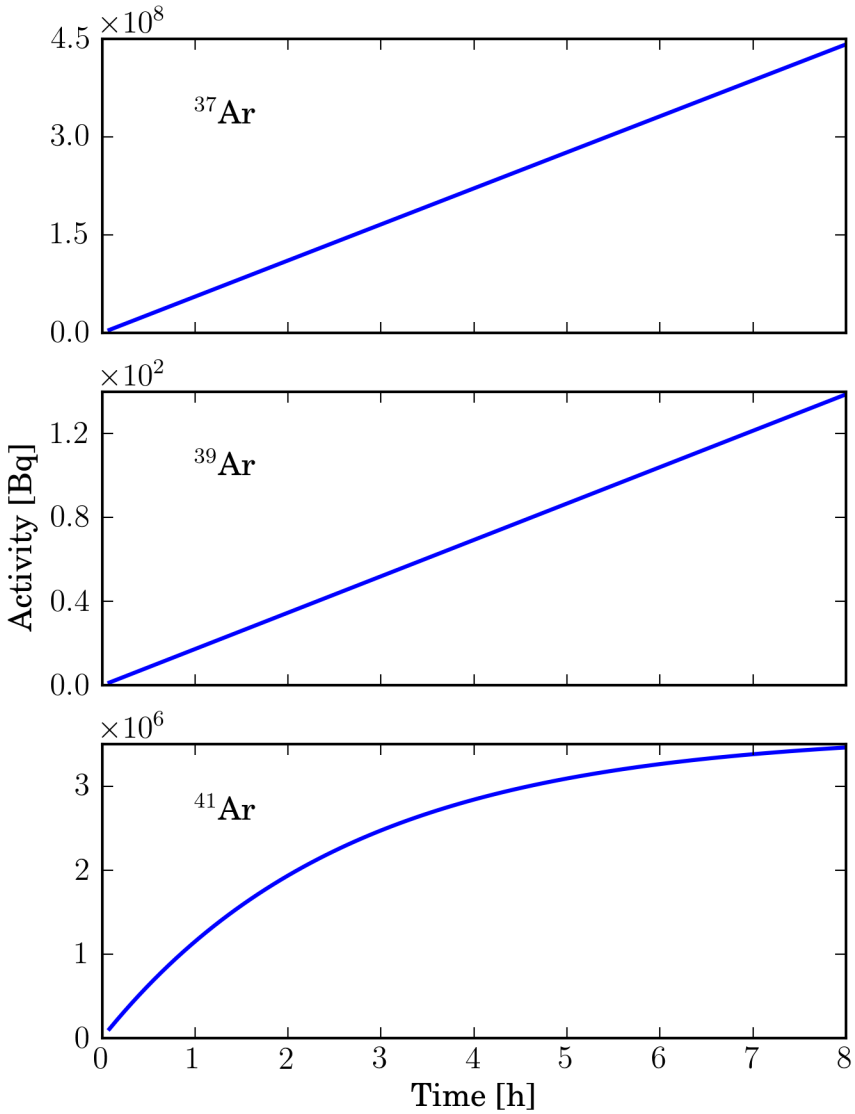

Figure 5.8: Activity of ^{37}Ar (top), ^{39}Ar (center), and ^{41}Ar (bottom) in the biological shield during an 8 h irradiation at 950 kW.

Based on the time-dependent buildup of the radioargon isotopes, buildup constants were calculated for the reactor pool and are given in Table 5.11.

Table 5.11: Buildup constants for radioargon in the biological, assuming the irradiation time is much less than the half-life for each isotope and that initial concentrations are minimal.

	^{37}Ar	^{39}Ar
Bq·kWh^{-1}	$(5.811 \pm 0.40) \times 10^{4}$	$(1.825 \pm 0.15) \times 10^{-2}$

Analysis of the contributions of the individual tally segments to the total buildup revealed a number of noteworthy trends in the spatial distribution of buildup in the shield. First, buildup in the biological shield at the far side of the pool (right side of the pool in Figure 3.5) was negligible relative to the segments nearer to the core. Buildup in the floor of the shield represented 0.56% of the total. Over 99.5% of the total buildup occurred in the vertical walls of the shield near the core. Further analysis of buildup in these walls indicated that much of the buildup occurs in the concrete near the beamport penetrations of the shield. To explore the effect of the beamport penetrations, the model was run to calculate the buildup only in the concrete defined by a cylinder of radius 25 cm surrounding each beamport, as indicated in Figure 5.9.

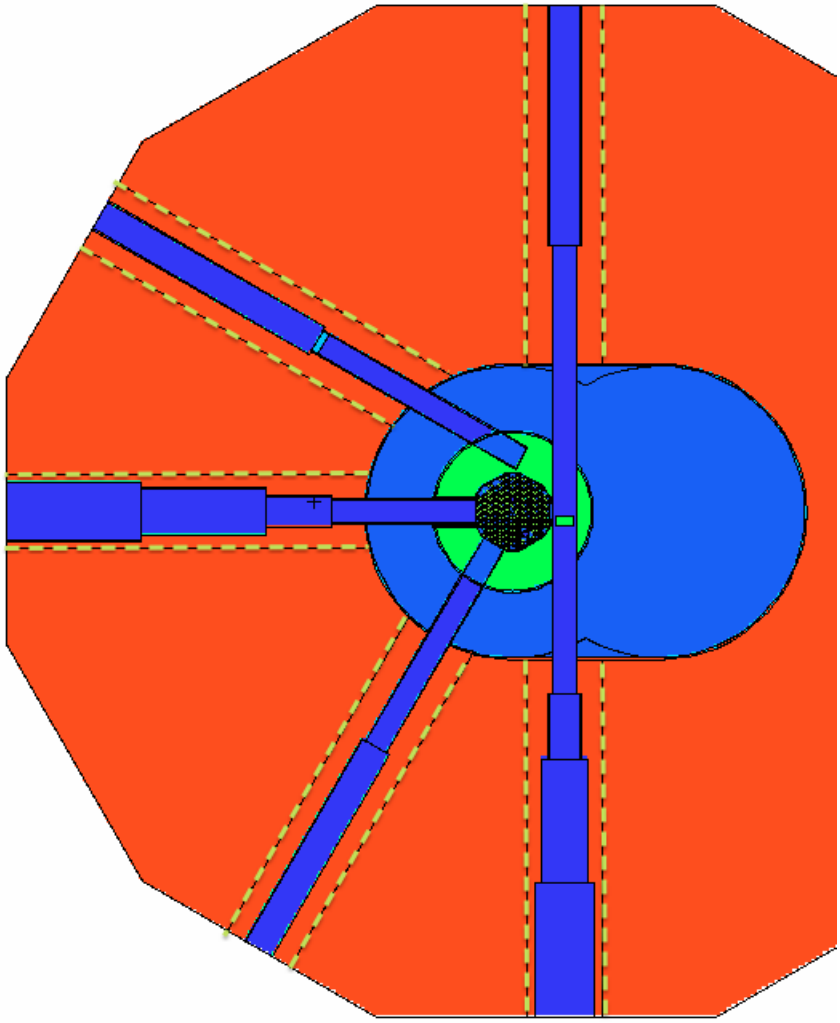

Figure 5.9: Tallying regions for calculating radioargon buildup in the biological shield concrete around the beamports. Boundaries of the 25 cm radius cylindrical regions are indicated by green lines

The five tallying cylinders, representing roughly 2.5% of the total volume of concrete in the modeled portion of the biological shield, accounted for 52.3% of the total radioargon buildup. Tallying cylinders of radius 35 cm, representing 5.7% of the total concrete volume, accounted for 57.8%. Although neutron leakage from the beamports is not a dominant effect in radioargon production in the biological

shield, it does contribute significantly to the cumulative buildup.

The buildup calculations in this section accounted for the Ca content of concrete, however the porosity of concrete will also result in some radioargon buildup within the concrete due to the activation of air. For high-density magnetite concrete (the material used in the radiation transport model for the biological shield), previous work has shown the air content to range between 3-6% by volume, depending on the aggregate particle size [66]. This air concentration was used to repeat the buildup calculation in a section of the biological shield with activation of air also included. At 6% air, the presence of the air increased the ^{37}Ar buildup by 4.6×10^{-4} % and the ^{39}Ar buildup by 1.5×10^{-2} %. The ^{41}Ar buildup increased by nearly a factor of 3. Significantly higher air content in structural concrete is unlikely, so the contribution of air activation in concrete is negligible to the total buildup of ^{37}Ar and ^{39}Ar. As a result of the small (n,α) cross-section in ^{44}Ca and the relatively large concentration of ^{40}Ar in air, accounting for the air content of concrete is a significant consideration for ^{41}Ar buildup. Based on these results, the total ^{41}Ar inventory in the biological shield is a factor of 2.8 higher than is indicated in Figure 5.8.

5.4 Other Sources

5.4.1 Ternary Fission

The maximum yield of ^{37}Ar calculated by Ref. [36] due to ternary fission is $2.2 \pm 0.22\times10^{-9}$ atoms of ^{37}Ar per binary fission. Although a number of nuclear data sets include ternary fission yields for a limited set of light elements, none were found with radioargon data, so the Kugler number represents that most up-to-date data on ^{37}Ar yield. It should be noted the ternary fission yield itself was not calculated

in Ref. [36], but constraints on the upper limit of the yield were determined. These upper limits are used in this section to calculate the maximum radioargon inventory in the fuel, primarily for the purposes of comparison to results from other sources. It should also be noted that depletion calculations with ORIGEN-ARP do not track ^{37}Ar as a fission product. Other depletion codes were not tested.

At 950 kW, the maximum ternary fission production rate of ^{37}Ar was calculated to be $(6.52 \pm 0.66) \times 10^7$ atoms s^{-1}, where the dominant source of uncertainty is the ^{37}Ar ternary fission yield. Estimates of the maximum production rate of the other radioargon isotopes, based on their yields calculated by Ref. [36], are given in Table 5.12. These production rates were calculated based on the fission rate for the reactor at 950 kW, and did not include the effects of radial or axial flux distributions within the fuel.

Table 5.12: Maximum yield and associated production rate at 950 kW for radioargon isotopes produced by ternary fission.

	TF Yield $[10^{-9}$ atoms $\cdot$ BF$^{-1}]$	Prod. Rate $[10^7$ atoms $\cdot$ s$^{-1}]$
^{36}Ar	< 2.4	< 7.12
^{37}Ar	< 2.2	< 6.52
^{38}Ar	< 2.0	< 5.93
^{39}Ar	< 0.78	< 2.31
^{40}Ar	< 690	$< 2.05 \times 10^3$
^{42}Ar	< 2.2	< 6.52

The depletion code was modified to include the fixed production rate of the radioargon isotopes. The region of interest for ternary fission is only the cladded fuel, so other contributions to the radioargon inventory were neglected in the depletion calculation. Typical buildup and absorption reactions within the radioargon isotopes themselves were accounted for. Flux within the fuel region varied by ele-

ment, so element B2 was chosen as the representative position. Flux profiles were generated for elements C3 and D4 (to cover the innermost, second, and third rings of fuel) as well, though the highest flux pin of the three was chosen to further pursue the estimation of the upper limit on the radioargon inventory.

For the upper limits given in Table 5.12, the buildup of radioargon for an 8 hour operation at 950 kW is shown in Figure 5.10.

Under typical conditions the ^{37}Ar produced as a ternary fission product would be contained in the cladded fuel region and would not be released from the facility. As a result, the radioargon produced from ternary fission is not included in the release inventory for the reactor. Some work to quantify the release of radioxenon from reactors has suggested fission product gas release as a source of radioxenon effluents [67]. If quantifiable levels of fission product radioxenon is being transported out of the cladded fuel region, it is likely that radioargon would be released through the same pathway. In this scenario, ternary fission could be a non-negligible source of radioargon release. For uncladded fuels, such as those found in a molten salt reactor, significantly elevated levels of ^{37}Ar could be seen.

Radioxenon release from processed medical isotope targets and reprocessed spent fuel has also been a topic of interest as these sources can interfere with atmospheric radioxenon monitoring for the CTBT. These processes would also result in the release of the radioargon isotopes produced by ternary fission.

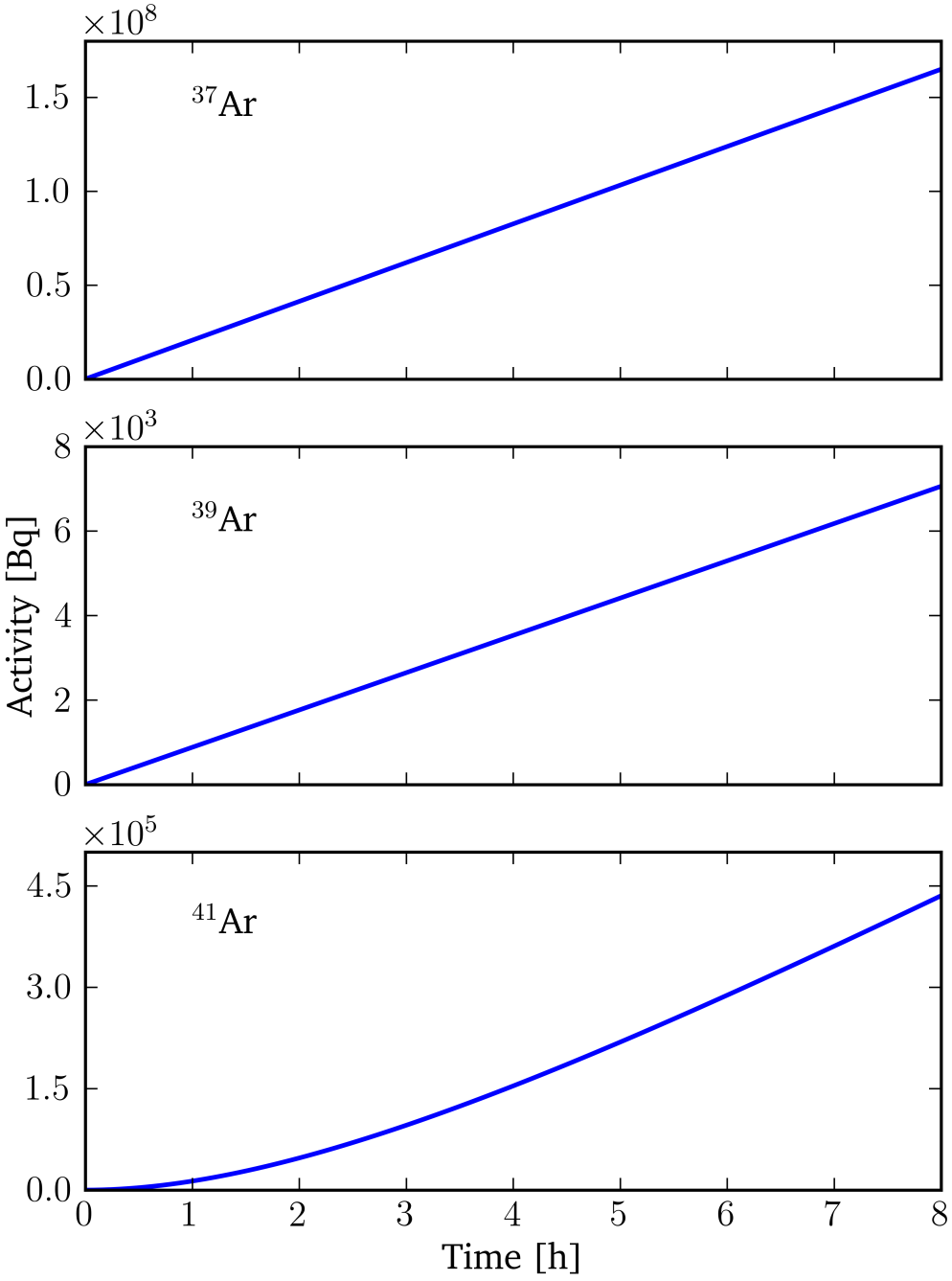

Figure 5.10: Maximum buildup of ^{37}Ar (top), ^{39}Ar (middle), and ^{41}Ar (bottom) in fuel element B2 during operation at 950 kW.

5.5 Diffusion and Tranport

While no experimental data on the diffusivity of argon in concrete that could be applied to this work was found, the diffusivity of a noble gas in a concrete matrix can be approximated based on the assumption that the ratio of noble gas diffusivity to hydrogen diffusivity is constant across various matrices [68]. The results of Ref. [68] found the relationship:

$$\frac{D_{NG}}{D_{H_2}} = \sqrt{\frac{M_{H_2}}{M_{NG}}} \tag{5.5}$$

where M_{NG} and M_{H_2} are the atomic masses of the noble gas and molecular hydrogen, respectively. For Ar, Equation (5.5) gives a ratio of 0.2236. For a typical concrete sample in STP conditions, the H_2 diffusivity was found to be 1.18×10^{-2} $cm^{-2}\cdot s^{-1}$. The estimated ^{37}Ar diffusivity in concrete is then 2.64×10^{-3} $cm^{-2}\cdot s^{-1}$.

Although high-fidelity characterization of gas transport in porous media typically accounts for the diffusivity of the gas in the pore volume and in the structure of the material then weights those on the porosity of the material, this estimate combines the bulk transport behavior in the concrete. Previous studies indicated that molecular diffusion is the dominant process for transport of gas in concrete unless there is a significant pressure gradient applied to the concrete and that bulk diffusivities shows good agreement with experimental results [69].

A simplification of Equation (3.20) was solved for a one-dimensional geometry to determine the time-dependent concentration of ^{37}Ar across the biological shield from the reactor face to the outward face. Diffusion from the biological shield back into the pool was ignored due to the lining of the reactor pool. The initial concentration distribution was determined based on the buildup results for the layers of

the biological shield presented in Section 5.3.3.

The solutions for the simplified Equation (3.20), based on the initial buildup concentrations, were calculated for 12 individual 20 cm layers of the biological shield. The exchange of radioargon between layers was calculated using finite elements with integrated time steps of 300 s, and the distribution of ^{37}Ar within each element was recalculated. The exchange between the outer element and the bulk air relied on the assumption that any ^{37}Ar the diffused out of the concrete was immediately transported away from the surface.

Ref. [70] found that the release efficiency for Rn gas is 0.035$\pm$0.006 for Rn produced in the concrete matrix from the decay of Ra and 0.40$\pm$0.04 for Rn produced near the pores of the matrix. These coefficients account for the fact that some atoms are trapped in the lattice of the concrete or in an isolated pore and do not diffuse significantly from the point of origin. Results from Section 5.3.3 indicated that air activation has a negligible contribution to ^{37}Ar buildup in the biological shield, so the fraction of mobile ^{37}Ar is likely to be on the order of the value 0.035$\pm$0.006. This value was used as an estimate of the release efficiency (or emanation coefficient) of Ar in a concrete matrix. There were no Ar-specific values found in the literature. The recoil of Rn from the decay of Ra contributes to the mobility of Rn, so the actual emanation coefficient of Ar may be lower considering it is not produced by decay.

As indicated by the asmyptotic value of Figure 5.11, 2.1$\pm$1.5% of the total ^{37}Ar produced during an operation is released into the bulk air prior to decay. Uncertainty in the total release fraction is on the order of 80% and includes the assumptions for the diffusion model and uncertainty in the diffusivity and emanation coefficient of ^{37}Ar. Due to the long half-life of ^{37}Ar, the exhalation of the biological shield from a single operation continues during period on the order of 1×10^2

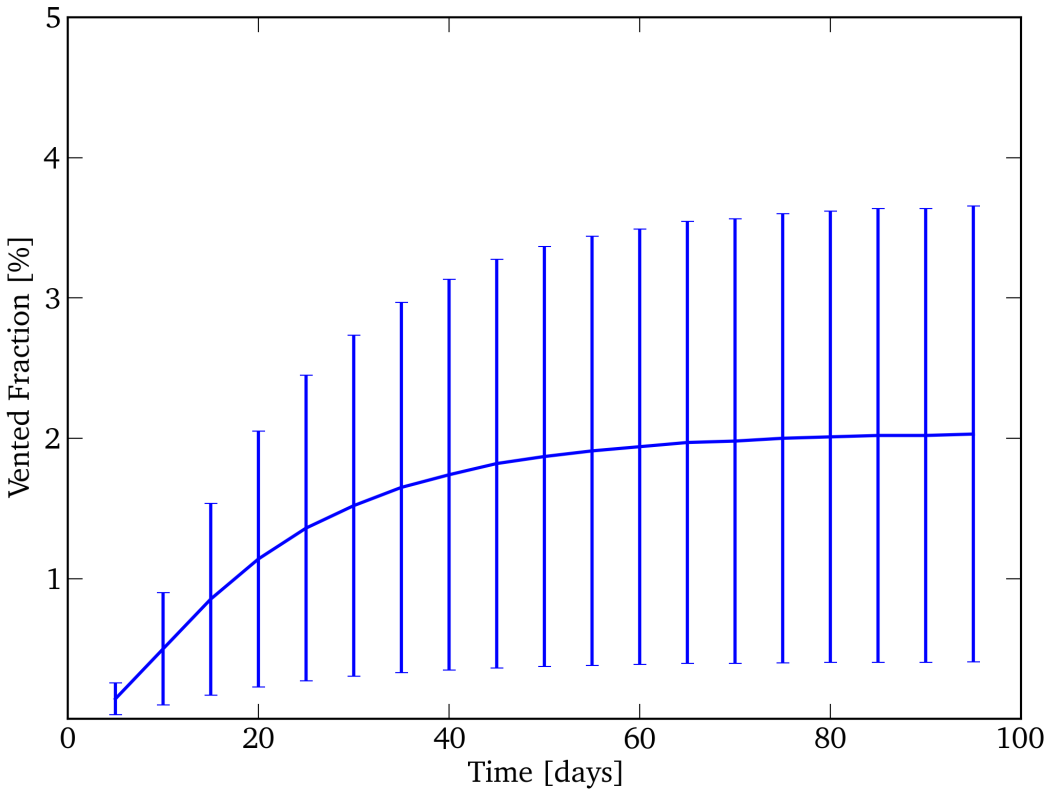

Figure 5.11: Vented fraction of ^{37}Ar from the biological shield following a 8 h irradiation at 950 kW.

days. During the 24 hour period following operation, nominally the time the reactor would be shut down prior to operation the following day, less than 0.1% of the total ^{37}Ar produced during the operation would be released.

In order to include the exhalation of the biological shield in the estimate for the release rate of radioargon from the reactor, the release rate was calculated based on the vented fraction in Figure 5.11. A total 4.44×10^{8} Bq of ^{37}Ar is produced for an 8 hour irradiation at 950 kW. The release rate and cumulative vented ^{37}Ar activity are shown in Figure 5.12.

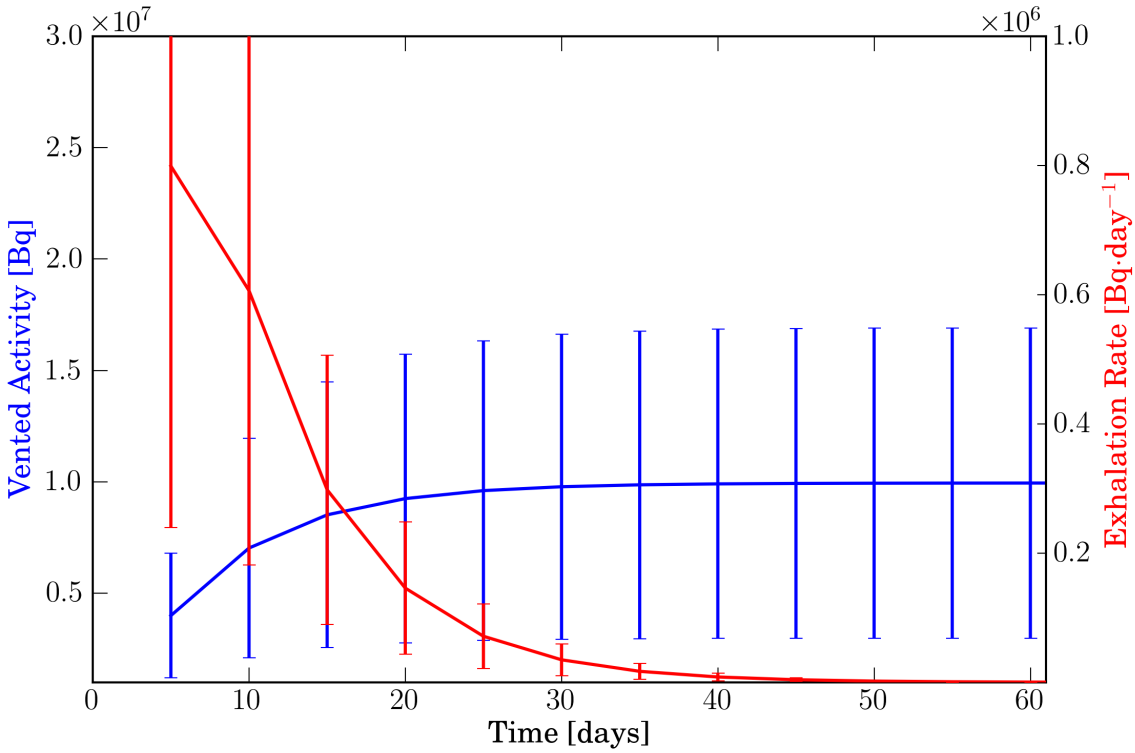

Figure 5.12: Vented activity (blue) and exhalation rate (red) of ^{37}Ar from the biological shield following a 8 h irradiation at 950 kW.

The presence of cracks, seams along the pool liner or beamports, or other transports pathways could significantly increase the fraction of radioargon that escapes the biological shield.

The solutions to the diffusion equation were then compartmentalized to determine the fraction of ^{37}Ar off-gassing from the regions nearest the boundary. The results from Figures 5.11 and 5.12 account for the full 240 cm depth of the biological shield. For 120 cm deep concrete region, the vented fraction is 3.4%. For regions

with depth smaller than 120 cm, the vented fraction approaches 3.5% which is the limiting value based on the exhalation coefficient. In the regime of depths on the order of 100 cm or less, a negligible amount of ^{37}Ar decays prior to release.

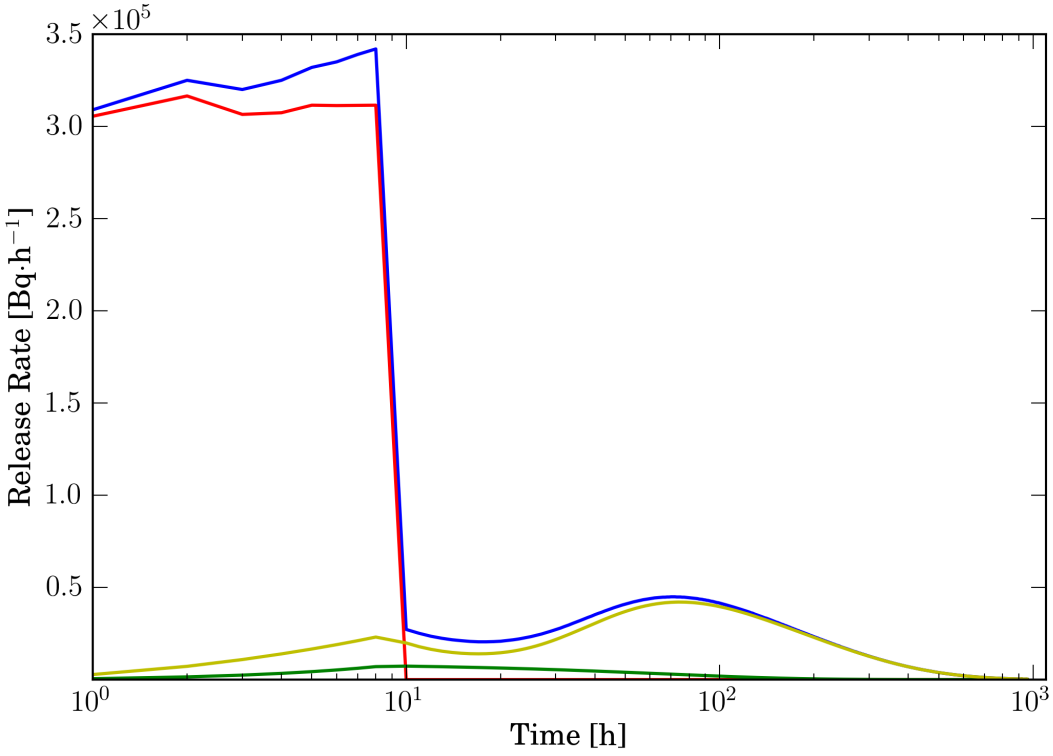

Figure 5.13: Release rate of ^{37}Ar from the beamports and RSR (red), the reactor pool (green), and the biological shield (yellow) for an 8 h operation at 950 kW. The total release rate is shown in blue. Model resolution for release rate calculations was 1 h.

To compare the exhalation of the biological shield to the other release mechanisms, the entire production-release model was run to simulate an 8 hour operation at 950 kW and the subsequent release from the shield and pool. The release rates

from each source as a function of time are plotted in Figure 5.13. The integrated release activity for the operation was calculated to be $(1.05\pm0.8)\times10^{7}$ Bq, corresponding to a power-normalized release of $(1.381\pm1.052)\times10^{3}$ Bq·kWh^{-1}.

This scenario assumes continuous venting of the irradiation facilities in the reactor, however real operation of the reactor would likely isolate specific irradiation facilities from the purge system if they are not being used for an experiment. The integrated buildup for a given operation time can be calculated to determine the release activity if the irradiation facilities are vented in batch rather than continuously during operation. The integrated activities during the 8 hour operation, representing the total activities in the irradiation facilities assuming no venting, are given Table 5.13. These values can be used to calculate the batch release of a single facility or combination of facilities for a given operation time.

The primary effect of a batch release is that the effluent source term will some orders of magnitude higher than for continuous release, albeit for a much short release period. The effect of this change on the ground-level concentration of ^{37}Ar is explored in Section 5.6.

Table 5.13: Integrated ^{37}Ar activity in the irradiation facilities assuming the facilities are not vented during operation. Values are for operation at 950 kW.

Time [h]	RSR [Bq]	BP1 [Bq]	BP2 [Bq]	BP3 [Bq]	BP4 [Bq]	BP5 [Bq]
1.0	1.15×10^{4}	1.12×10^{5}	1.54×10^{4}	9.7×10^{4}	1.28×10^{4}	6.26×10^{4}
2.0	2.30×10^{4}	2.24×10^{5}	3.07×10^{4}	1.94×10^{5}	2.55×10^{4}	1.25×10^{5}
3.0	3.45×10^{4}	3.36×10^{5}	4.61×10^{4}	2.91×10^{5}	3.82×10^{4}	1.88×10^{5}
4.0	4.59×10^{4}	4.48×10^{5}	6.14×10^{4}	3.87×10^{5}	5.10×10^{4}	2.50×10^{5}
5.0	5.74×10^{4}	5.60×10^{5}	7.67×10^{4}	4.84×10^{5}	6.37×10^{4}	3.13×10^{5}
6.0	6.87×10^{4}	6.72×10^{5}	9.21×10^{4}	5.81×10^{5}	7.64×10^{4}	3.75×10^{5}
7.0	8.01×10^{4}	7.84×10^{5}	1.07×10^{5}	6.77×10^{5}	8.91×10^{4}	4.37×10^{5}
8.0	9.16×10^{4}	8.95×10^{5}	1.23×10^{5}	7.74×10^{5}	1.02×10^{5}	5.00×10^{5}

5.6 Atmospheric Transport

Meteorological data for the TRIGA transport simulations was collected from the NOAA Air Resource Laboratory server. HYSPLIT simulations used archived data from the Eta Data Assimilation System (EDAS) with 40 km resolution. Ground-level concentrations were calculated as the average concentration over the range 0 m - 100 m above ground level (AGL). The emission rate used for the simulation was 3.2×10^{5} Bq·h^{-1} which was taken from Figure 5.13 to be the emission rate during operation of the NETL TRIGA at 950 kW. The decay of ^{37}Ar during transport was accounted for. Washout from precipitation (wet deposition) and chemical interaction with species at ground level (dry deposition) were neglected due to argon's low reactivity. The source location was Austin, TX at 30.25 N, 97.75 W with a release height of 10 m.

Simulations generated a release from the NETL TRIGA associated with an 8 hour operation at 950 kW. The release was tracked at 30 minute intervals for 24 hours following the start of the reactor operation. Simulated releases were initiated at 8:00 Coordinated Universal Time (UTC) on the first day of the month of March 2012, June 2012, September 2012, and December 2012.

For all simulated releases, the maximum concentration was seen at the point of release. The maximum calculated stack concentration was 4×10^{-5} Bq·m^{-3}, which was seen 1 hour into the simulated operation in March 2012. This concentration is equivalent to 4×10^{-2} mBq·m^{-3}, which is below the 20 mBq·m^{-3} MDC for a field measurement system. Stack concentrations for the simulated operations in June, September, and December of 2012 ranged between 1.3 - 1.7×10^{-2} mBq·m^{-3}. Considering the laboratory system MDC of 2×10^{-2} mBq·m^{-3}, samples collected at the NETL TRIGA stack may be measurable in the laboratory setting, depending on at-

mospheric conditions. Operations at power substantially lower than 950 kW would be unlikely to produce detectable concentrations of ^{37}Ar. A snapshot of the ground level concentration at the time of reactor shutdown for the simulated December 2012 operation is shown in Figure 5.14.

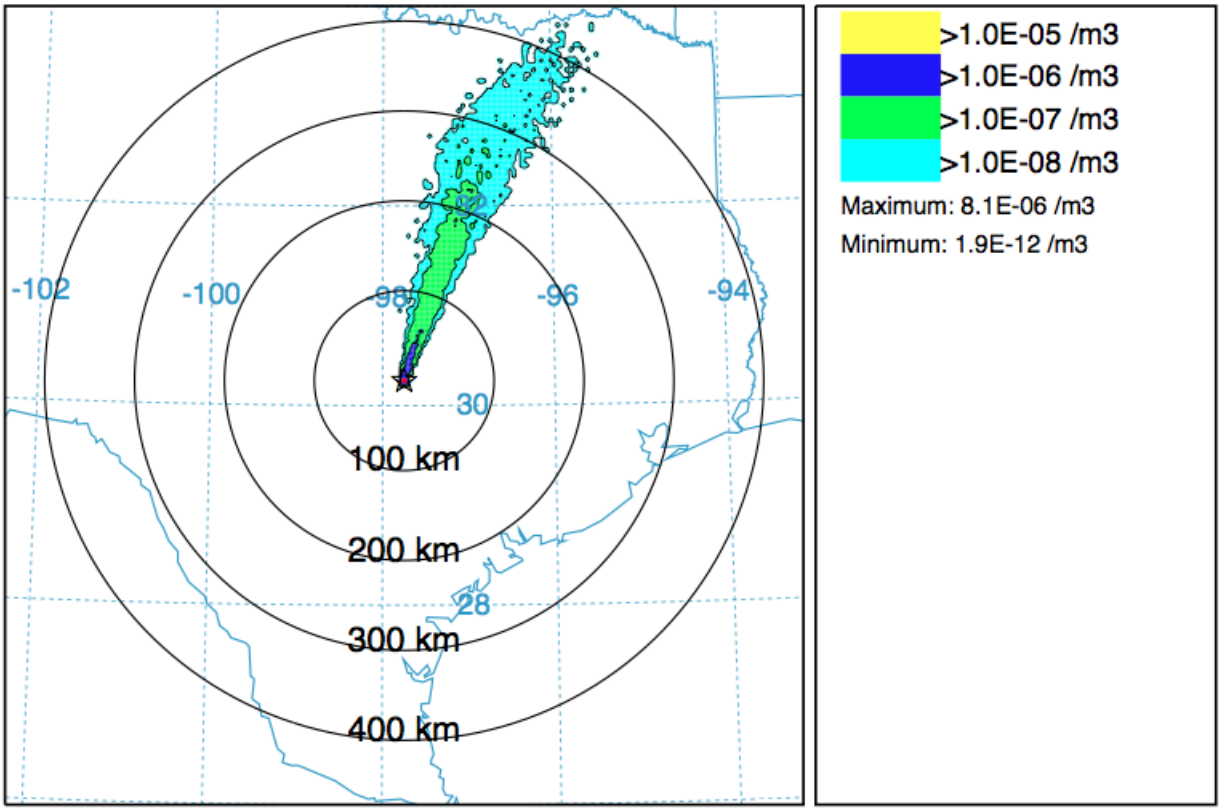

Figure 5.14: Ground level concentration of ^{37}Ar for a simulated operation of the NETL TRIGA for 8 h at 950 kW. Contours represent a snapshot of the ground level concentration at reactor shutdown. Contours are in dimensions of Bq·m^{-3}.

Ground-level concentrations greater than 1×10^{-6} Bq·m^{-3} existed within 150 km of the point of release, with most of the simulated releases only showing these concentrations within 80 km. Concentrations greater than 1×10^{-7} were seen for distances up to 400 km from the point of release. The simulated releases indicated

that the ^{37}Ar dispersed below the 1×10^{-7} Bq·m^{-3} level at the 400 km range within 24 hours of the reactor operation. To verify the insensitivity of the results to variations in the atmospheric data, the December 2012 simulation was re-run using HYSPLIT's Ensemble tool which calculates confidence intervals for the concentration contours based on variance in results produced by different atmospheric data sets. The ground-level concentrations listed above are consistent within 95% across the EDAS, Global Data Assimilation System data, and North American Model data.

Table 5.14: Dilution factor as a function of distance for ground level ^{37}Ar during a simulated release in December 2013.

Distance [km]	Dilution Factor [h·m^{-3}]
10	2×10^{-11}
20	1×10^{-11}
40	4×10^{-12}
100	2×10^{-12}
150	1×10^{-12}
200	7×10^{-13}

As a whole the results indicate that at a ^{37}Ar emission rate of 3.2×10^{5} Bq·h^{-1}, the NETL TRIGA would not produce field-detectable concentrations of ^{37}Ar. At full power and under favorable atmospheric conditions, stack sampling may produce detectable concentrations for a laboratory ^{37}Ar measurement system.

As discussed in Section 5.5, the irradiation facilities of the reactor would likely not be vented continuously during operation. Table 5.13 gave integrated activities in the irradiation facilities, which dominate the total ^{37}Ar inventory during operation, assuming that the facilities are not vented. The total ^{37}Ar inventory after an 8 hour operation at 950 kW, representing the largest inventory available for batch re-

lease under typical operating conditions, was calculated to be (2.49±0.15)×10^6 Bq. A batch release of this magnitude would only occur if the RSR and all beamports were simultaneously batch vented immediately after the full-power operation.

Considering the continuous release rate of 3.2×10^5 Bq·h^{-1}, a batch release of 2.49×10^6 Bq over a period of less than a minute represents a release two orders of magnitude higher than would be seen for continuous purging, albeit for a much shorter release period. A simulated 1 minute release of 2.49×10^6 Bq produced a peak ground-level concentration of 2.2×10^{-1} mBq·m^{-3} at the site of the release. As a result of the short-term release, the maximum ground-level concentration was diluted below that of a continuous release within 4 hours of the batch release.

In order to investigate the source term necessary to produce detectable ^{37}Ar, the simulation for December 2012 was re-run to determine the dilution factor as a function of distance from the point of release. Results indicated that stack concentrations of 20 mBq·m^{-3}, the MDC for a field measurement system, required a minimum emission rate of 5×10^8 Bq·h^{-1}.

For points beyond the stack, Table 5.14 gives the dilution factor as a function of distance based on results from the December 2012 simulation. The actual ground-level concentration can be determined by multiplying the dilution factor by the emission rate in units of Bq·h^{-1}. In all cases the concentration was measured within the plume. Concentrations outside the plume were negligible.

Regression analysis on the data in Table 5.14 gives the relationship:

$$C = \left(-2.36 \times 10^{-7}\right) x^3 + \left(3.70 \times 10^{-6}\right) x^2 - \left(1.96 \times 10^{-5}\right) x + \left(3.62 \times 10^{-5}\right) \quad (5.6)$$

with $R^2 = 0.9995$ where C is the ground-level concentration and x is the distance from the release in the direction parallel to the wind, as described in Section 3.5.

These results indicate the following:

- An emission rate of 1×10^{6} Bq·h^{-1} would be lab detectable at 10 km
- An emission rate of 1×10^{7} Bq·h^{-1} would be lab detectable at 100 km
- An emission rate of 1×10^{9} Bq·h^{-1} would be field detectable at 10 km
- An emission rate of 1×10^{10} Bq·h^{-1} would be field detectable at 100 km

As a reference, the Advanced Test Reactor (ATR) in the United States operates at a maximum power of 250 MW, as indicated by data in Appendix C. If the NETL TRIGA's emission rate is scaled to the power of the ATR, the ATR ^{37}Ar emission rate can be estimated to be 8.4×10^{7} Bq·h^{-1}. The release rate would be detectable by lab measurements but not field measurements, based on the estimated MDC of each system described in Section 2.4.

5.7 ^{41}Ar Benchmarking

Although the focus of the calculations and results has been the production of the longer-lived radioargon isotopes, primarily ^{37}Ar due to its relevance to CTBT verification, the short half-life and high-energy gamma ray of ^{41}Ar makes it the most significant of the radioargon isotopes for reactor operations. Within the USA, the Nuclear Regulatory Commission requires that facilities report their annual ^{41}Ar release activity to ensure that operations do not pose a health risk to nearby populations. Within facilities, the buildup of ^{41}Ar can pose a health risk to operators and experimenters. In many cases, reactors are built with specific systems to continuously vent air-filled regions to prevent this buildup. The NETL TRIGA includes ^{41}Ar venting systems for each of the beamports and a pool off-gas system that pulls air

from the top of the reactor pool. The beamport systems are typically only operated when specific beamports are in use.

The average ^{41}Ar release for the NETL TRIGA through the first three quarters of 2013, tracked to comply with NRC regulations, was normalized through the operations during that period. The published release activity for 2013 was 1.07×10^{11} Bq with an average release rate of 4.23×10^{5} Bq·kWh^{-1}. This value represents averaging over various operations with different run times and different venting systems active and includes all sources of ^{41}Ar buildup.

Due to the short half-life of ^{41}Ar, the buildup rate is non-linear and depends on the runtime of the reactor. The number of reactor operations at the NETL TRIGA during 2013 was used to calculate an average runtime and power, which was then used to model the ^{41}Ar buildup rate for comparison to the published numbers. For a 1 hour operation, the ^{41}Ar production rate across the entire facility was found to be $(5.25\pm0.29)\times10^{6}$ Bq·kWh^{-1}. The off-gas rate of the reactor pool, calculated in Section 5.3.2, indicated that 5.9% of the ^{41}Ar would escape the pool before decay. Based on this result, 94.1% of the ^{41}Ar produced in the pool would not make it into effluent stack. Accounting for this, the effective buildup rate would be $(4.32\pm0.24)\times10^{6}$ Bq·kWh^{-1}.

The published average ^{41}Ar release rate of 4.23×10^{5} Bq·kWh^{-1} differs from the modeled average of $(4.32\pm0.24)\times10^{6}$ Bq·kWh^{-1} by nearly a factor of 10. In both cases, the values represent averaging over a range of operation times and reactor power. Considering this, and the fact that the model did not explicitly factor in the use of venting systems in the beamports or other mechanisms affecting transport time, this comparison is best used as a check on the reasonableness of the modeled results.

6 | Generalization of Results

6.1 Thermal and Fast Flux Dependence

A key application of the results presented in previous sections is insight into the radioargon release inventory from other research reactors. In order to apply this work to a broader problem, the results for the NETL TRIGA need to be generalized, to the extent possible, to describe other irradiation conditions and environments.

Results for air activation in the NETL TRIGA were presented on a per facility basis, with the total volume of the facility and the neutron flux in the facility affecting the magnitude of the buildup constants. To determine the generality of the buildup constants for the 3L, the RSR, and the individual regions of the PTS and beamports, the constants were normalized by the volume of the tallied region. The plot of the normalized buildup constants, in dimensions of Bq $\cdot$ hr$^{-1}\cdot$ cm^{-3}, is given in Figure 6.1.

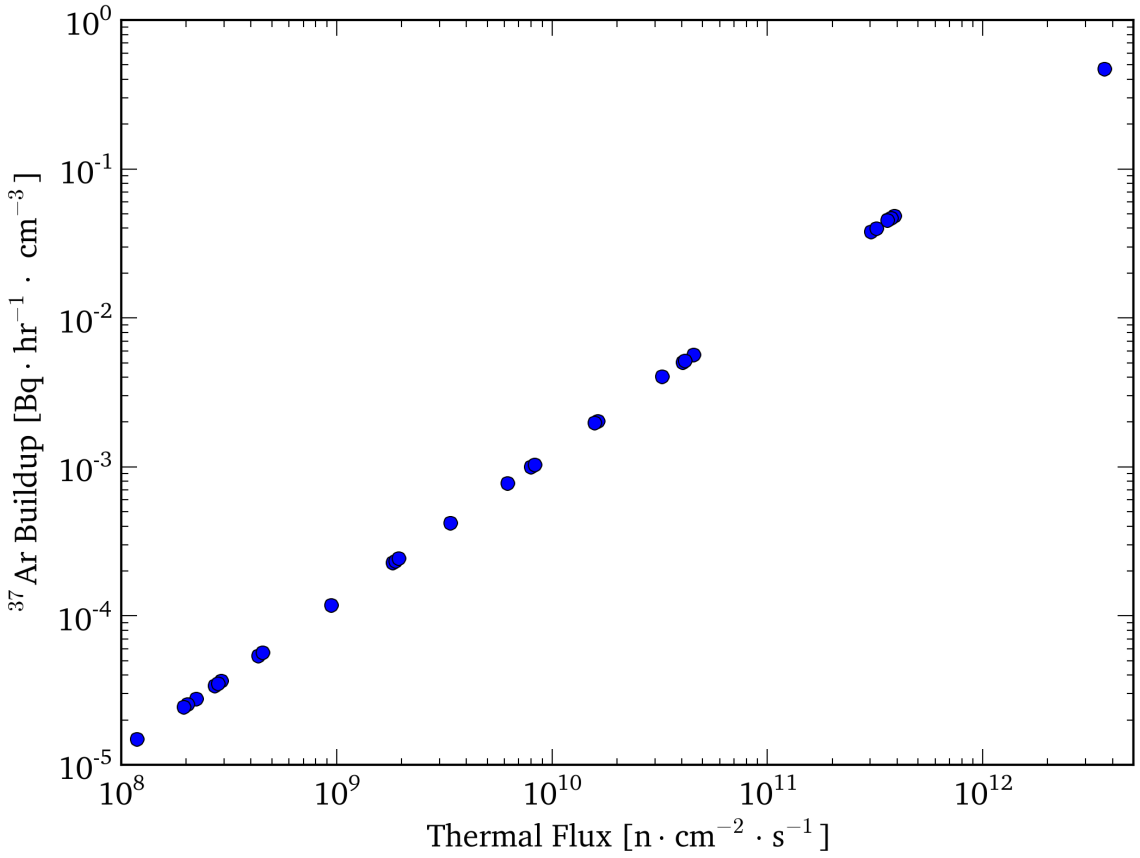

Figure 6.1: Volume-normalized buildup constants as a function of thermal flux for the air-filled irradiation facilities.

Figure 6.1 indicates a distinct relationship between the thermal flux and the buildup constant for ^{37}Ar. The outlier point at $\phi = 1.8\times10^{9}$ n·cm^{-2}·s^{-1} represents the buildup factor for the cavity of the PTS that is surrounded with a cadmium liner. The liner suppresses the thermal flux inside the facility. The buildup constant indicates that the radioargon buildup is larger than would be predicted based on the magnitude of the thermal flux alone. The results of Section 7 showed that contributions from reactions in the epithermal energy range contribute as much

as 10% of the radioargon buildup. In the case of the PTS irradiation cavity, the epithermal flux is $\sim 1 \times 10^3$ higher than the thermal flux, so epithermal reactions dominate radioargon buildup and the resulting activity is higher than the thermal flux would indicate.

Regression analysis on the data in Figure 6.1 gives the following relationship for ^{37}Ar buildup due to the activation of air by a typical thermal reactor flux:

$$\ln B = 0.99779 \ln \phi_t - 26.20659 \tag{6.1}$$

where A is the activity of ^{37}Ar normalized per kWh·cm^3 at an integrated thermal flux value ϕ_t. With the exception irradiation facilities where the thermal flux is significantly modified by some sort of filtering mechanism, this relationship holds for the general case of irradiation of a unit volume of air. The buildup of ^{37}Ar can be estimated for some air-filled region of a reactor with a known volume and known thermal fluence. Buildup in regions where the flux deviates significantly from a typical thermal reactor flux needs to be modeled on a case-by-case basis.

A similar method was followed to generalize the results describing the buildup of ^{37}Ar in the pool. The individual buildup constants for each of the 37 segmented regions used for flux tallying the NETL TRIGA pool were volume-normalized. These normalized buildup constants were plotted against the thermal flux of the region, as shown in Figure 6.2.

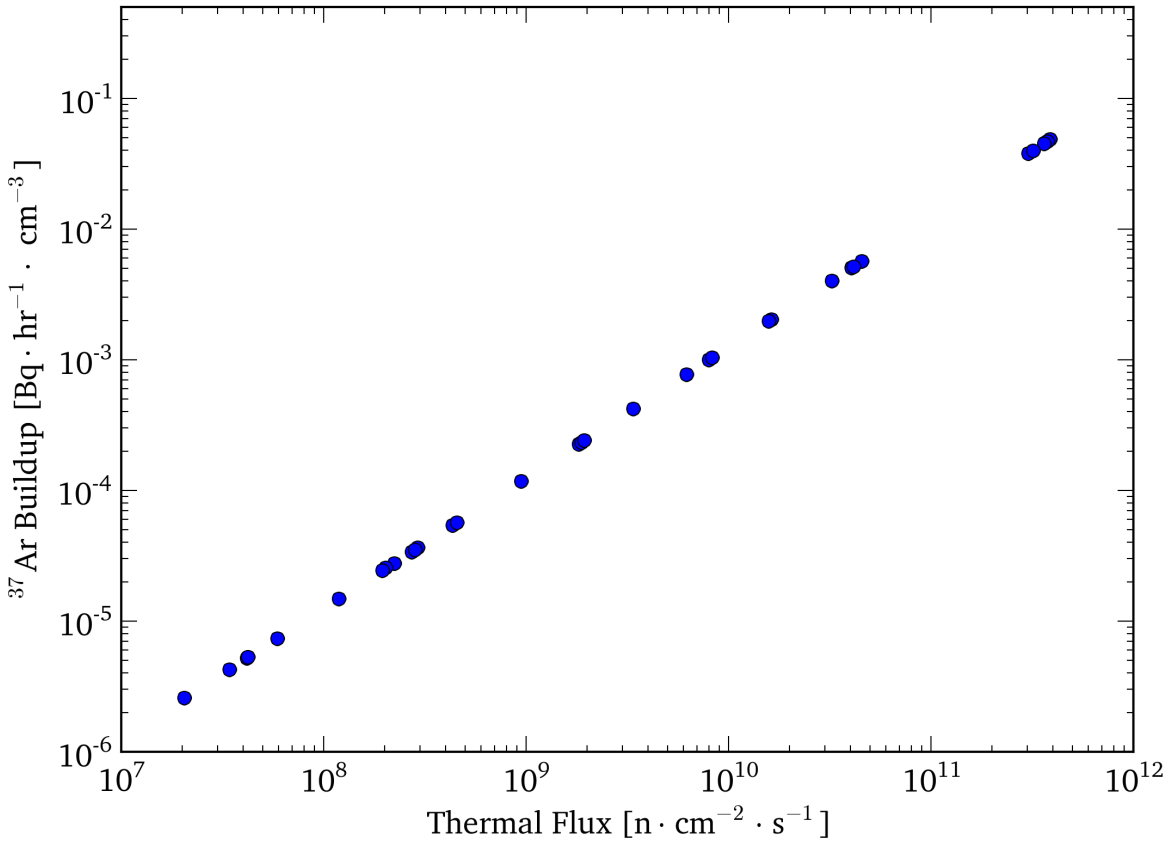

Figure 6.2: Volume-normalized buildup constants as a function of thermal flux for the tally regions of the reactor pool.

The trend in Figure 6.2 indicates that a similar relationship to Equation (6.1) can be found for buildup in water. Regression analysis on the data from Figure 6.2 gave:

$$\ln B = 1.00016 \ln \phi_t - 29.71627 \tag{6.2}$$

where B is the buildup constant in dimensions of [Bq· hr^{-1}· cm^{-3}] and ϕ_t is the

thermal flux.

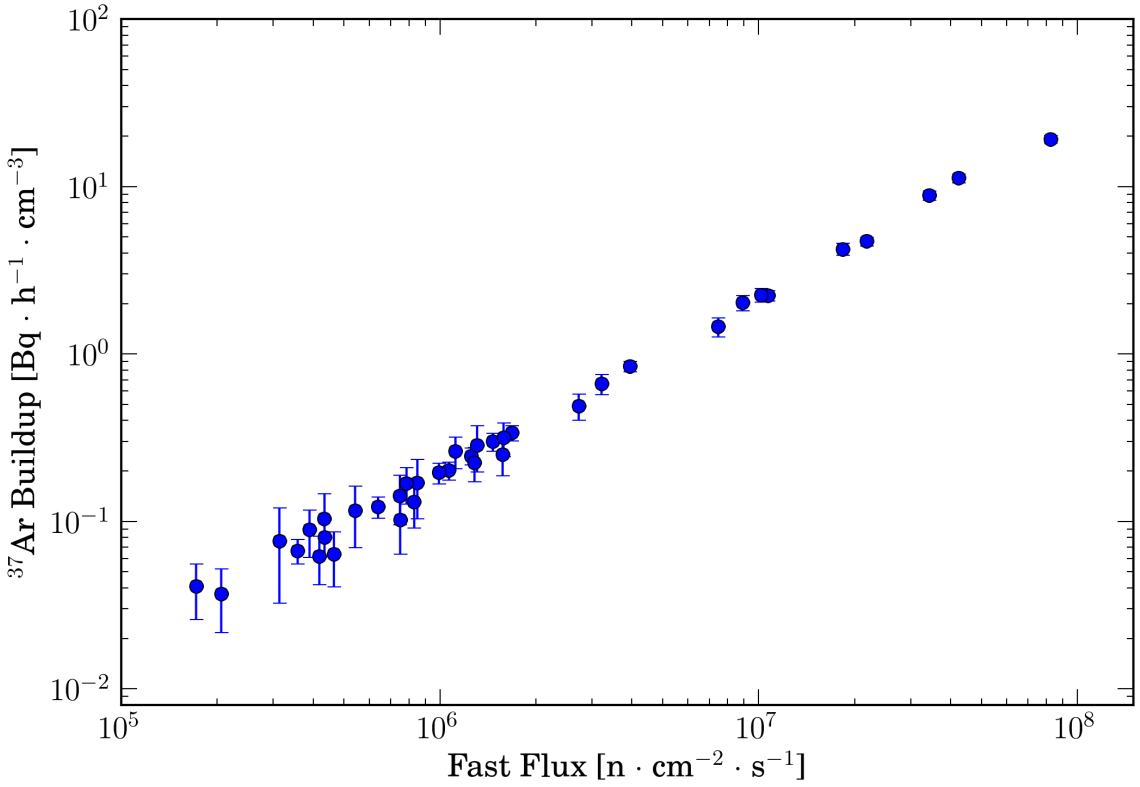

Figure 6.3: Volume-normalized buildup constants as a function of fast flux for the tally regions of the reactor biological shield.

The results from each of the 38 tally regions of the biological shield were volume-normalized and plotted against the thermal flux in the region, as was done in Figures 6.2 and 6.1. The same regression against the thermal flux gave an unreliable relationship. Sensitivity analyses reported in Section 7.2 show that Ar buildup due to Ca activation in the biological shield is dominated by fast neutron reactions rather than thermal reactions. The normalized buildup constants were plotted against the

fast neutron flux in Figure 6.3.

Regression analysis on the data from Figure 6.3 gave:

$$\ln B = 1.04277 \ln \phi_f - 16.03859 \tag{6.3}$$

where B is the buildup constant in dimensions of [Bq· hr^{-1}· cm^{-3}] and ϕ_f is the fast flux.

A number of elements of this work did not lend themselves well to generalization and would likely need to be calculated on a case-by-case basis. The variety in concrete mixtures and manufacturing methods result in significant variation in composition, which affects the ^{40}Ca concentration, and air void structure, which affects diffusion behavior. The variations in composition can also have significant impact on the shielding properties of the concrete and affect buildup deep in the shield. High accuracy measurements for radioargon buildup and diffusion in concrete would need to account for the specific characteristics of the concrete matrix. Generalizable relationships for pool off-gassing were derived in Section 5.3.2, however appropriate pool geometry would need to be included in the calculation. A number of assumptions, such as a well mixed pool, may be inappropriate in particular cases. Additionally, atmospheric transport behavior is highly sensitive to conditions at specific locations and specific times, so generalization of these results is limited to trends based on running test cases.

6.2 Proxy Isotope Estimates

Based on the relationships calculated in Equations (6.1), (6.2), and (6.3), the production rate in a given facility could be calculated if the geometry and flux for

various regions was known or calculated. In order to estimate the ^{37}Ar release from a facility where this information is not known or available, a proxy isotope method was developed [71]. Annual release data from the High Flux Isotope Reactor (HFIR) at Oak Ridge National Laboratory includes calculations of the released activity of a large set of noble gases (insufficient release data for the NETL TRIGA precluded using it as the example facility). ^{131m}Xe, ^{133}Xe, ^{133m}Xe, ^{135}Xe, and ^{41}Ar were chosen as proxy isotopes for modeling the activation of air (buildup from the activation of the Ca isotopes was not generalized in this manner). These xenon isotopes are frequently used in other monitoring applications.

The depletion code was run using a representative thermal reactor flux profile with a thermal flux of $1\times10^{15}\text{n}\cdot\text{cm}^{-2}\cdot\text{s}^{-1}$ to calculate the time dependent ratios of ^{135}Xe/^{133}Xe and ^{133m}Xe/^{131m}Xe as a function of irradiation time t_i and decay time t_d. In this case, t_i represented the time that a unit of air was subjected to a neutron flux and t_d represented the time between irradiation and release from the effluent stack. These results were compared against the published radioxenon ratios for HFIR to determine the facility-averaged values of t_i and t_d. For these irradiation parameters, the activity ratio for ^{37}Ar/^{41}Ar was calculated and the published ^{41}Ar activity was used to estimate the activity of ^{37}Ar released.

Results showed that a set of (t_i, t_d) value pairs produced radioxenon ratios that agreed with the published data with the pre-determined tolerance of 10%. For calculating the radioargon ratio, the average of the values within the tolerance were used. These averages were $t_i = 371$ s and $t_d = 12930$ s. The results for the ^{37}Ar/^{41}Ar activity and the ^{37}Ar release are given in Table 6.1.

As a result of the large difference in the half-lives of ^{37}Ar and ^{41}Ar, the projected release ratio showed greater sensitivity to decay time than to irradiation time, and decay time was found to vary little from year to year. As seen in Table 6.1, ratios

Table 6.1: Published ^{41}Ar release, calculated ^{37}Ar/^{41}Ar ratio, and annual ^{37}Ar release for the High Flux Isotope reactor.

Year	^{37}Ar/^{41}Ar [$\times 10^{-4}$]	^{41}Ar Release [$\times 10^{13}$ Bq]	^{37}Ar Release [$\times 10^{10}$ Bq]
1996	1.77	7.40	1.31±1.3
1998	1.44	29.6	4.27±9.0
1999	1.79	48.1	8.61±11.0
2000	1.63	13.4	2.19±2.3
2001	1.46	0.08	0.01±0.02
2002	1.42	5.51	0.78±1.0
2003	1.71	8.55	1.46±1.5
2004	n/a	7.51	n/a
2005	n/a	7.77	n/a
2006	1.37	8.47	1.16±1.3
2007	1.58	13.2	2.10±2.2
2008	1.48	21.4	3.16±3.6
2009	1.50	3.11	0.47±0.5
2010	1.44	3.50	0.51±0.6

of the proxy isotopes were not calculated for years 2004 and 2005. Published HFIR radioxenon release ratios were 2 to 3 orders of magnitude higher in 2004 and 2005 than in other years. Agreement between the model and the HFIR data was not consistent within an acceptable, and resulting ^{37}Ar estimates would have been greatly exceeded by their associated uncertainties. The reasons for the substantial change in radioxenon release for those years is unknown.

It should be noted that, according to Table 6.1, uncertainties in the projected ^{37}Ar release are, at best, on the order of the magnitude of the release itself. The dominant source of error in the predicted release concentrations is the distribution in t_i and t_d values that result in agreement between the model and the HFIR data. This distribution is a result of tolerance for agreement between the model and the published data, which is necessary to account for the uncertainty in the HFIR data

and the assumptions made by the model. The standard deviation values presented in Table 6.1 represent the minimum uncertainty in the data. Consideration of a spatially constant flux, identical diffusion behavior between isotopes, and distinct irradiation and decay times may introduce further uncertainty that is not account for in the results.

6.3 Global Research Reactor Fleet

In order to estimate the global release of ^{37}Ar from research reactors, the operational status of each reactor in the global fleet was determined using the International Atomic Energy Agency Research Reactor Database (RRDB) [72]. The RRDB curates information on the design and status of all research reactors, including the categorization of each reactor based on its utilization or average annual operation time:

- High utilization: greater than 20 full-power weeks per year
- Medium utilization: between 4 and 20 full-power weeks per year
- Low utilization: less than 4 full-power weeks per year

Subcritical assemblies, pulsed reactors, piles, and other non-traditional reactor types (many of which are listed as having a thermal capacity of 0 kW) which do not maintain typical operations and/or would not be expected to substantially contribute to the global source term were neglected for the calculation. In total, 163 research reactors listed on the RRDB as operational as of November 2013 were included in the calculation. These facilities, representing the global research reactor fleet, accounted for a total of 2.18×10^6 kW thermal capacity. Appendix C lists the

annual utilization and other operational parameters of the reactors included in the calculation.

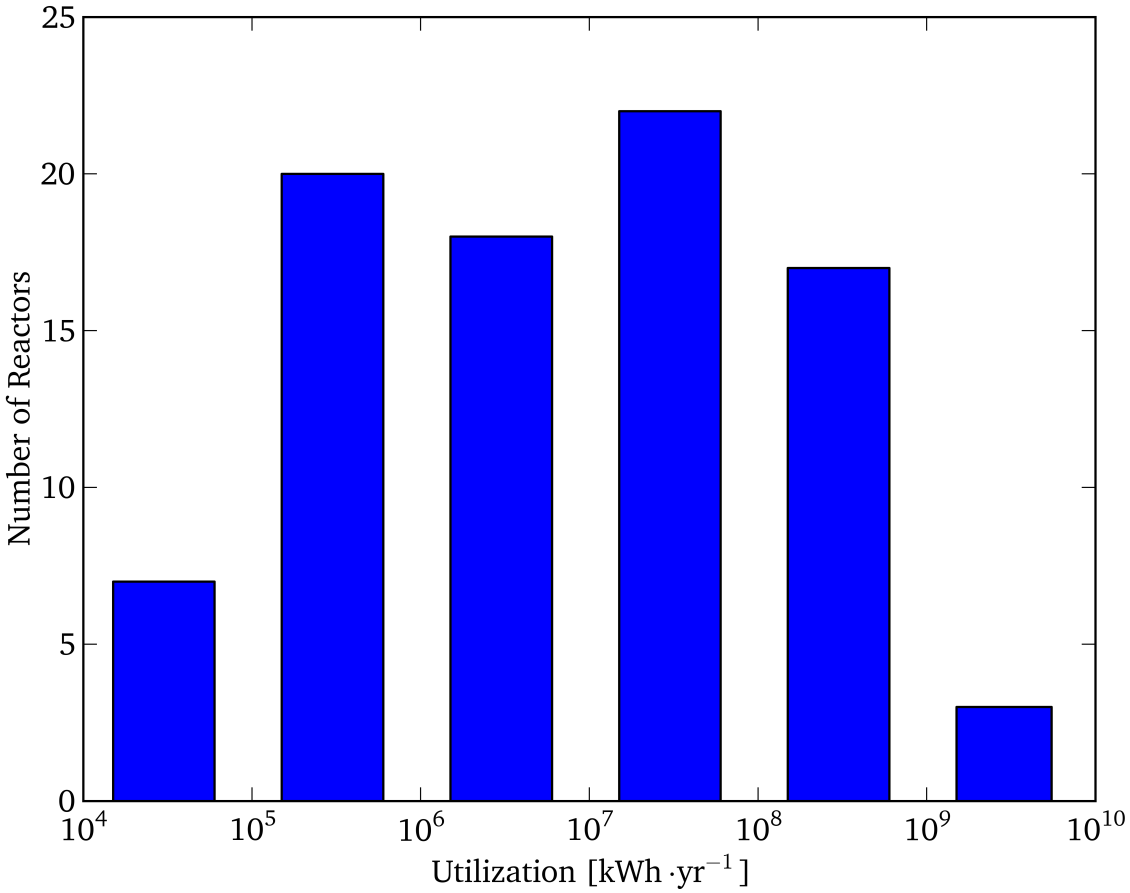

Figure 6.4: Distribution of research reactor utilization, according to the IAEA Research Reactor Database [72]. Bars indicate number of reactors within each utilization decade. Those reactors categorized in the RRDB as low utilization are not included.

The thermal energy produced, in kWh per year, for each of the medium and high utilization reactors was recorded from the RRDB to calculate the annual thermal energy production of the global research reactor fleet. For facilities where the

utilization was listed was medium or high but the actual MWd·yr^{-1} was not provided, an estimate was calculated based on the reactor power and the minimum operation time definitions for each category of utilization (listed above). The ^{37}Ar production rate of the NETL TRIGA, in Bq·kWh^{-1}, was then used to estimate the total annual ^{37}Ar release for the global research reactor fleet.

The thermal energy production for the fleet was calculated to be 3.86×10^{10} kWh·yr^{-1}. Individual contributions ranged between $\sim1\times10^{4}$ kWh·yr^{-1} for small, university-based reactors to $\sim1\times10^{10}$ kWh·yr^{-1} for particular Pu production reactors, isotope production reactors, and national-scale test reactors. The distribution of medium and high utilization reactors across the fleet is plotted in Figure 6.4.

From Section 5.5, an 8 hour operation of the NETL TRIGA at 950 kW resulted in an integrated release of $(1.05\pm0.8)\times10^{7}$ Bq of ^{37}Ar. The normalized release activity per unit of thermal energy produced at the NETL TRIGA is then $(1.381\pm1.052)\times10^{3}$ Bq·kWh^{-1}.

Considering the NETL TRIGA as a surrogate for the variety of research reactor designs across the fleet, the 3.86×10^{10} kWh·yr^{-1} corresponds to an annual release on the order of 1×10^{13} Bq·yr^{-1} of ^{37}Ar from the global research reactor fleet. The true release inventory is subject to the actual utilization of each facility in a given year. Further investigation of ^{37}Ar production and release from reactor designs beyond the TRIGA will illuminate the variance in the Bq·kWh^{-1} produced at different facilities and improve the accuracy of the global estimate.

Matuszek [15] measured the release rate of noble gases from a number of power producing reactors and found ^{37}Ar an annual release (adjusted for 95% capacity factor) for a 1.3 GWt pressurized water reactor (PWR) of 7×10^{11} Bq·yr^{-1}. Allowing the PWR to represent the $\sim$1200 GWe of installed capacity of the global power reactor fleet, Matuszek's measurements correspond to an annual release on the

order of 1×10^{15} Bq·yr^{-1} for the power reactor fleet.

7 | Sensitivity Analyses

Following the calculation of radioargon buildup in the NETL TRIGA facilities using MCNPX and the depletion code, a number of operational and methodological parameters were varied to explore the sensitivity of the results to these parameters. The operational sensitivity analyses were undertaken to explore the effect of changes to the physical characteristics or operations of the reactor. In large part this work was done in an effort to generalize, to the extent possible, the results of this project to describe radioargon production in other reactor facilities.

The interest in exploring the sensitivity of radioargon buildup calculations to changes in methodology is born primarily from the lack of precedent in comparable radioargon work. Light elements are typically not tracked in sophisticated depletion calculations where spent fuel isotopics are result of interest. These sensitivities were explored in this project to inform the approach to future work on radioargon production, specifically to identify those mechanisms, reactions, and species that are necessary to include in calculations and those that can be reasonably neglected.

For the sensitivity analysis of air activation, the production of radioargon in the 3L irradiation facility was used as a test case. Although this facility is backfilled with CO_2 or N_2 under normal operations and contributes minimally to the NETL TRIGA radioargon inventory, the flux profile is generally representative of the flux in an LWR and the radiation transport statistics for the facility are reliable. The purpose of the sensitivity study, in this case, is to explore the effect of various computational approaches. Any representative flux profile could have been used.

The baseline results for buildup of radioargon in the 3L for typical operation of the NETL TRIGA reactor were presented in Table 5.2 found in Section 5.2.1. The sensitivity of methodological changes are reported in relation to these results. Differences in activity are considered for 950 kW irradiations for the duration of 8 hours, unless otherwise noted.

7.1 Operational Cycles

One challenge in modeling the production of radioargon in the NETL TRIGA facility is the irregular frequency of reactor operations. The reactor is typically not operated on weekends, and operations during the working week can range from intermittent 1 hour runs at low power to 8 hour runs at full power. As seen in the results presented in Section 5.2, the buildup of radioargon is dependent on, in large part, the neutron fluence in the regions of interest. At lower neutron fluences, the linear response of the radioargon buildup allows for simple calculation of the radioargon inventory as long as the fluence (irradiation time and flux/power) are known. For some neutron fluence greater than those tested for previous results, the concentration of radioargon will become sufficiently large that loss by absorption will balance the buildup by capture in the stable isotopes. At these fluences, the linear relationships presented in Section 5.2 will no longer hold.

For the flux profile given in Section 5.2.1, the depletion code was run to characterize the deviation from linear buildup of ^{37}Ar as a function of neutron fluence. The results of a full-power irradiation for 120 h is shown in Figure 7.1.

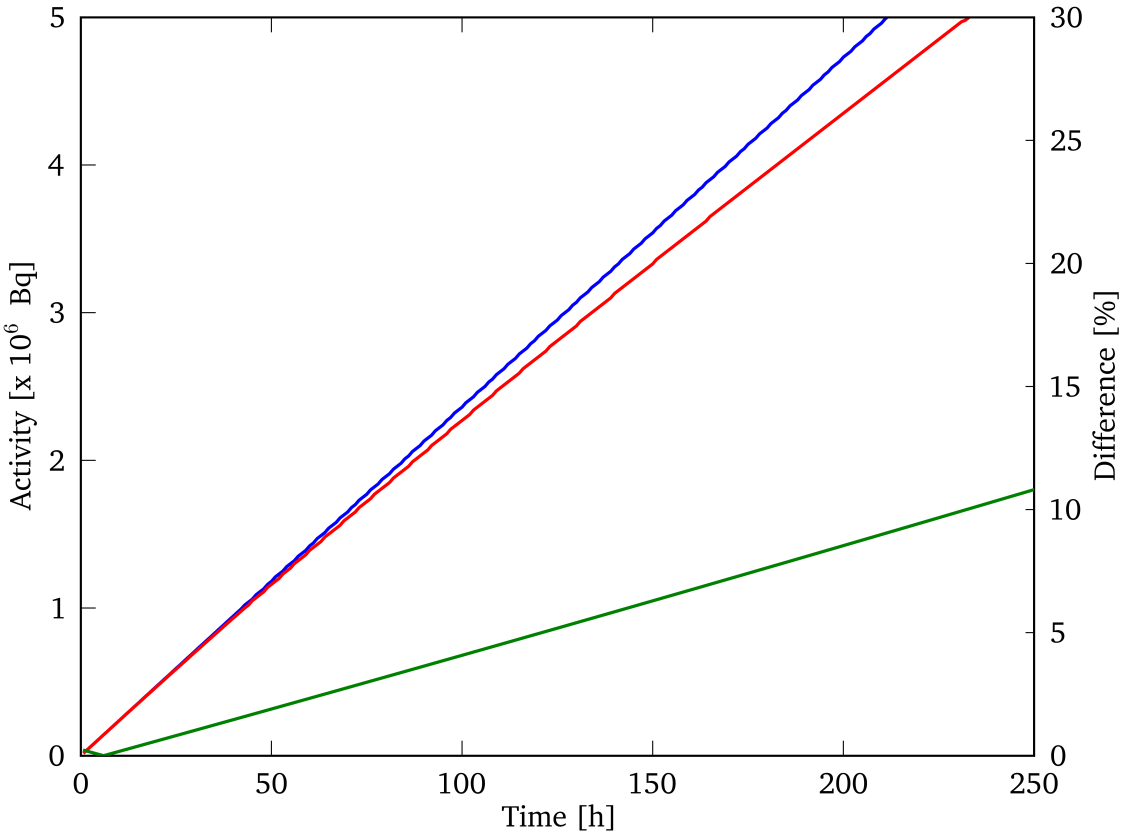

Figure 7.1: Buildup of ^{37}Ar in the 3L during a hypothetical irradiation. Activity calculated by the buildup coefficient for ^{37}Ar in the 3L (blue) and by the depletion code (red), along with the difference between the two (green).

The difference between the results of the depletion code and the extrapolated value using the buildup coefficient was 5.0% at 120 hours of operation. Differences in excess of 10% were not seen until 233 hours of full-power operation. For the purposes of comparison, the difference between the ^{39}Ar activity calculated by the buildup constant and the activity calculated by the depletion code was found to be 0.1% at 233 hours of full power operation. These discrepancies, calculated at full power, represent the largest that would be expected as a function of time.

Operation a lower reactor power would allow the linear relationship to hold for longer as a result of the lower fluence. Similarly, it is expected that the buildup coefficients would hold longer for other irradiation facilities for the same reasons. As previously mentioned, the short half-life of of ^{41}Ar precludes the use of a buildup constant to estimate the activity as a function of fluence.

For practical purposes, the buildup constant is accurate for facilities exposed to the bulk air of the facility and facilities accessed on a regular basis where the concentration of radioargon is vented to the bulk effluent inventory. Based on this, extrapolation from the linear buildup coefficients will provide accurate estimates of the radioargon concentration in the RSR, the PTS, the beamports, and the reactor pool.

A similar comparison was made for a representative region of concrete in the biological shield. The buildup constant for that region was calculated and the predicted buildup was compared to the actual buildup calculated by the depletion code. The results for the time-dependent ^{37}Ar activity agreed within 5% through 128 hours of uninterrupted, 950 kW operation. Differences of 10% were not seen until 244 hours at full power.

Although the constants show good agreement with the time-dependent activities calculated by the depletion code, care must be taken in using the constants to predict the buildup of species in the concrete of the biological shield. For air filled facilities and air activated in the pool, there are active or passive means by which the activation products can be transported into the bulk air of the facility. For species created deep in the biological shield, buildup may occur without venting for very long time periods with many startup-shutdown cycles. In the case of Ref. [65], among other similar projects, transport of activation products in the shield are treated as insignificant even when considering the lifetime of the reactor.

Accurate calculation of the buildup over these long periods of any isotope would require explicit modeling of these operational cycles.

7.2 Epithermal and Fast Neutrons

Activation calculations, including those in ORIGEN, often compute time-dependent concentrations using only neutrons in the thermal energy range (< 1 eV) or by using a scalar constant for the thermal flux and maintaining a fixed ratio between thermal, epithermal, and fast neutron fluxes. Although thermal neutron reactions are expected to dominate the buildup of radioargon, the flux profile of the 3L was adjusted to explore the sensitivity of the results to contributions from reactions in the epithermal and fast energy ranges. The 8 hour, full-power activity for the 3L was compared for the complete flux profile, a profile with no fast neutrons ($E > 0.1$ MeV), a profile with no epithermal neutrons (1 eV $< E <$ 0.1 MeV), and a profile with only thermal neutrons. The results are presented in Table 7.1.

Table 7.1: Full-power, 8 h operation buildup of radioargon in the 3L for different flux regimes.

Flux Regime	^{37}Ar $\times 10^5$ [Bq]	^{39}Ar $\times 10^0$ [Bq]	^{41}Ar $\times 10^8$ [Bq]
Full	1.889	1.961	9.312
No fast neutrons	1.888	1.960	9.302
No epithermal neutrons	1.713	1.785	8.435
No fast or epithermal neutrons	1.712	1.784	8.425

The effect of excluding the fast neutron flux of the reactor is negligible, with results changing by $< 0.01\%$ for a flux profile with no fast neutrons. The exclusion of epithermal neutrons has a much larger effect on the results. Activities differed

by 9.3%, 8.9%, and 9.4% for ^{37}Ar, ^{39}Ar, and ^{41}Ar respectively. To investigate the relative importance of the resonance capture regions visible in Figure 3.1 to this effect, another calculation was conducted excluding only neutrons in the epithermal range with energy lower than the capture resonances (5×10^{-3} MeV), so as to include the resonance region in the calculation. The resulting activities were 1.868×10^{5} Bq of ^{37}Ar, 1.940×10^{0} Bq of ^{39}Ar, and 9.213×10^{8} Bq of ^{41}Ar. These results indicate that for the epithermal energy range 1 eV $< E <$ 0.1 MeV, roughly 90% of the radioargon buildup occurs from reactions above 5 keV. The region above 5 keV represents 95% of the epithermal regime so contribution to the buildup is distributed relatively evenly across the epithermal region.

The same sensitivities were investigated for buildup due to activation of Ca in concrete. The same behavior as air activation was not expected considering the large (n,α) cross-sections at fast energies. The 8 hour, full-power activity for representative region of the biological shield was compared for the complete flux profile, a profile with no fast neutrons, a profile with no epithermal neutrons, and a profile with only thermal neutrons. The results of these regimes also motivated an additional regime consisting of only fast neutrons. The results are presented in Table 7.2.

The results of Table 7.2 provide further insight on the results presented in Section 5.3.3. Unlike air activation, radioargon generated from Ca activation is dominated by interactions in the fast energy range. Considering the reduced fast flux expected for neutron transport through the reflector and pool, the likely source of this fast flux is scattering and leakage of fast neutrons from the beamport penetrations.

Table 7.2: Full-power, 8 h operation buildup of radioargon in a segment of the biological shield for different flux regimes. b/l indicates that the activity was below the threshold for tracking in the depletion code.

Flux Regime	^{37}Ar $\times 10^{8}$ [Bq]	^{39}Ar $\times 10^{1}$ [Bq]	^{41}Ar $\times 10^{6}$ [Bq]
Full	1.998	6.354	1.585
No fast neutrons	0.296	b/l	b/l
No epithermal neutrons	1.955	6.354	1.585
No fast or epithermal neutrons	0.253	b/l	b/l
No thermal or epithermal neutrons	1.702	6.354	1.585

7.3 Depletion Code Fidelity

7.3.1 Tracked Isotopes

The first set of analyses compared the results produced using various levels of fidelity with respect to the species accounted for in the depletion calculation. The baseline results were generated by accounting for the set of isotopes listed in Section 3.2.4: ^{31}P, ^{32}P, ^{33}P, ^{32}S, ^{33}S, ^{34}S, ^{35}S, ^{36}S, ^{35}Cl, ^{36}Cl, ^{37}Cl, ^{36}Ar, ^{37}Ar, ^{38}Ar, ^{39}Ar, ^{40}Ar, ^{41}Ar, ^{42}Ar, ^{39}K, ^{40}K, ^{41}K, ^{42}K, ^{40}Ca, ^{41}Ca, and ^{42}Ca.

For the case of air activation with no initial concentrations of radioargon, exclusion of all species except for the argon isotopes had minimal effect on the calculated activity of ^{37}Ar, ^{39}Ar, or ^{41}Ar above the level of uncertainty in the calculation. Exclusion of ^{42}Ar (which restricted the tracked species to ^{36}Ar, ^{37}Ar, ^{38}Ar, ^{39}Ar, ^{40}Ar, ^{41}Ar) also had no effect on the calculated activity of ^{37}Ar, ^{39}Ar, or ^{41}Ar above the uncertainty. Subsequent elimination of the higher A isotopes of argon had negligible effect on the lower A isotopes still tracked in the calculation.

Modeling of higher neutron fluence, representing power levels and/or irradia-

tion times larger than any reasonable operation of the research reactor, yielded no significant differences between the model that included all species and the model that excluded all species except argon. The relative insensitivity of the radioargon concentration to other elements in the activation of air illuminates the dominant effect of the high abundance of argon in air.

The diverse composition of concrete, as listed in Table 3.2, resulted in a larger set of isotopes to test for sensitivities. For concrete with no initial concentration of argon, exclusion of all species except for the argon and calcium isotopes had negligible effect on the buildup of radioargon. Further exclusion of isotopes isolated ^{44}Ca as the dominant source of ^{41}Ar, ^{42}Ca as the dominant source of ^{39}Ar, and ^{40}Ca as the dominant source of ^{37}Ar. These results reflect the high calcium content of concrete relative to other potential target isotopes.

7.3.2 Tracked Reactions

To investigate sensitivity to the inclusion or exclusion of specific reactions in the calculation, the fidelity of the depletion model was incrementally reduced by excluding reactions. For the case of air activation, results generally mirrored those of in the previous section. Exclusion of the reactions with low cross-sections in the thermal energy regime, leaving only (n, γ) reactions, (n, p) reactions, and (n, α) reactions, had no measurable effect on the calculated activity of ^{37}Ar, ^{39}Ar, or ^{41}Ar for the 8 hour irradiation at 950 kW. Reduction of the model to only account for radiative capture in the argon isotopes showed differences below the 1% level. These results are implicitly reflected in the linear buildup calculated for the air activation cases: the number density of stable argon target atoms is sufficiently large compared to the number density of radioargon atoms that the loss terms in Equa-

tion (3.2) are negligible compared to the buildup terms.

For reference, modeling constant full-power operation of the NETL TRIGA for the period of 365 days yielded discrepancies between the highest fidelity model and lowest fidelity model of 3.7%, $< 1\%$, and $< 1\%$ for ^{37}Ar, ^{39}Ar, or ^{41}Ar, respectively.

For the case of calcium activation, as with air activation, exclusion of all reactions but (n, γ) reactions, (n, p) reactions, and (n, α) reactions, had no measurable effect on the calculated activity of ^{37}Ar, ^{39}Ar, or ^{41}Ar for the 8 hour irradiation at 950 kW.

7.3.3 Nuclear Data Sets

As highlighted in Section 7.3.2, radiative capture events in the stable argon species are the dominant mechanism for the production of radioargon in the activation of air. Investigation of the sources of ENDF-formatted data for the capture reactions (MT102) in the stable argon species revealed that all the major evaluated nuclear data libraries (ENDF/B, JEFF, JENDL, ROSFOND) relied on the same set of experiments to produce the data. As a result of the identical data sets, the choice of nuclear data file would not have a measurable effect on the results of the depletion calculation.

Nuclear data for the ^{40}Ca(n, α) reaction has been experimentally derived separately for the ENDF file, JEFF and ROSFOND files, for the JENDL-3.3 file, and for the JENDL-4.0 file. In order to explore the effect of the use of each data file on the results for calcium activation, the depletion calculation was rerun with each file used as the cross-section for ^{40}Ca$(n, \alpha)^{37}$Ar. The neutron flux in BP4 at the point of entry into the biological shield was used as the representative flux for the calculation. The buildup of ^{37}Ar in a cubic centimeter of concrete for an 8 hour irradiation

at 950 kW is shown in Figure 7.2.

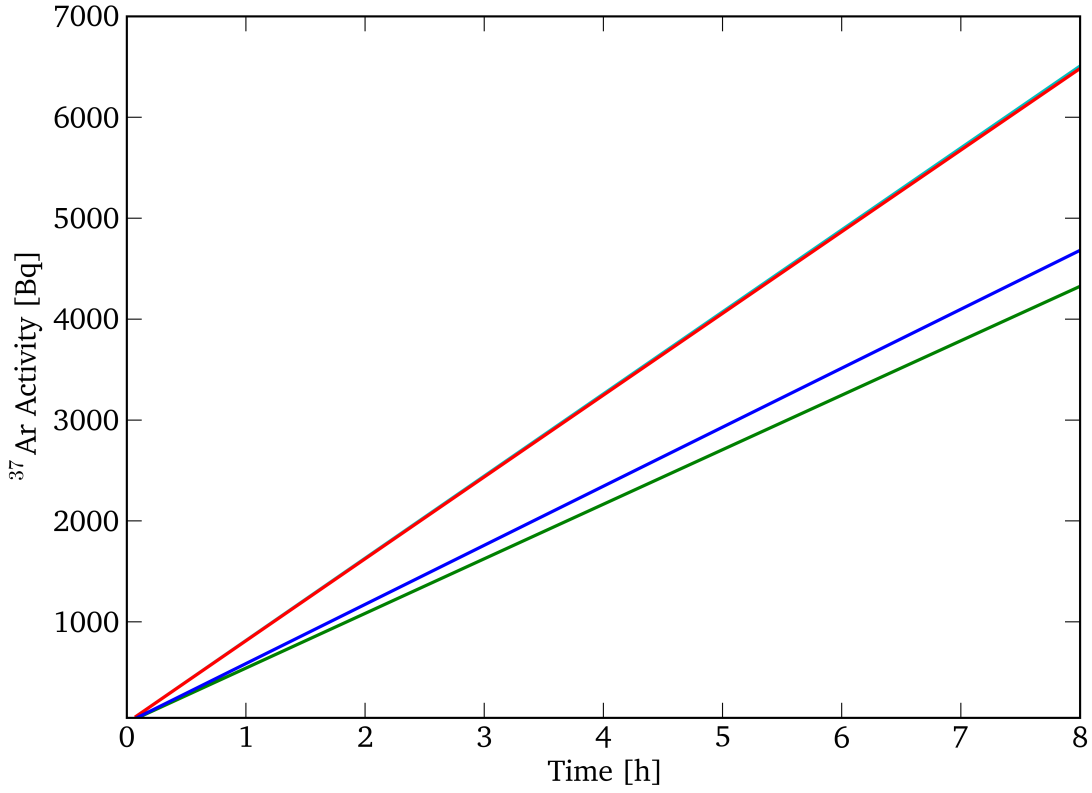

Figure 7.2: Buildup of ^{37}Ar in a sample of concrete as calculated using different nuclear data sets for the ^{40}Ca(n, α) reaction. Data from ENDF/B-VII (cyan), JEFF/ROSFOND (red), JENDL-3.3 (green), and JENDL-4.0 (blue) are shown.

The results for ENDF/B-VII agree with the results for JEFF/ROSFOND within a margin of 0.3%. Calculations using data from JENDL-3.3 and JENDL-4.0 differed from the ENDF calculations by 33% and 28%, respectively.

8 | Summary and Discussion

8.1 Summary of Results

Validation of the radiation transport model was conducted using experimental data collected during this project and previous projects at the NETL TRIGA reactor. Activity calculations for the 3L facility using wire flux monitor irradiation showed some disagreement with the model for two sample positions, and agreed within 1% for other sample positions. Model results for the entire 3L canister agreed within 4%. Activity calculations for the RSR using wire flux monitor irradiation agreed with the model within 1%, 2%, and 8% for the three sample positions tested. Comparison to previous work to comprehensively characterize the RSR flux showed agreement within 6% for thermal energies, 15% for epithermal energies, and 5% for fast energies. The average flux in a RSR sample can calculated by the model agreed with previous results within 3%. Comparison of endpoint fluxes for beamports 2 and 5 with previous agreed showed agreement with 17% and 15%, respectively.

Validation of the depletion code was conduction by comparing the time-dependent concentration of a number of isotopes to analytical solutions of simple decay cases. The code calculated single parent-daughter decay concentrations to an arbitrary precision. For multi-isotope decay chains, the code agreed with the ORIGEN-ARP code within 1% for all tested isotopes at all time steps. ORIGEN was also used for qualitative validation of the buildup capabilities of the code. ORIGEN input parameters for a 17x17 LWR fuel assembly data set were scaled to match the code's

calculated buildup for ^{36}Ar activation, the a full argon system was modeled. For long irradiations, the code agreed with the results of ORIGEN within a margin of 10% for all isotopes, with most agreeing within 5%. The effects of rounding in the numerical routines used in the code were found to be negligible.

To propagate uncertainty through the linear algebraic calculations of the depletion code, individual sources of uncertainty were identified in the input parameters including the MCNPX-generated flux profile, constants for converting MCNPX results to physical values, initial isotopic concentrations, and volume of the regions where radioargon is produced. Buildup calculations were iterated over with these variances in input parameters accounted for and the variance in the results were determined. Typical uncertainty for buildup in a facility was determined to be 4-4.5%. Individual uncertainty values were reported with the results. In order to estimate the effect of including uncertainty data in nuclear cross-sections (which are often neglected for general uncertainty measurements), the same procedure as above was followed with cross-section variance also included. Cross-section uncertainty was found to increase the uncertainty in reported ^{37}Ar, ^{39}Ar, and ^{41}Ar activities to 5.5%, 7.8%, and 5%, respectively.

Modeling of buildup due to air activation in the irradiation facilities found full-power, 8 hour activities of ^{37}Ar on the order of 1×10^5 Bq for both the 3L and 1×10^6 Bq for the RSR. Activity in the PTS sample tube was calculated to be on the order of 1×10^3 Bq for the same irradiation time, with a significant reduction of buildup as a result of the Cd liner. Buildup of ^{37}Ar in the beamports ranged between 1×10^5 Bq and 9×10^5, depending on the beamport, after an 8 hour irradiation at 950 kW.

Buildup of ^{37}Ar in the pool was also found to be on the order of 1×10^5 Bq, with nearly half the buildup occurring in the active fuel region of the reactor. The large majority of the buildup occurs in a small volume surrounding the core, with the

rest of the pool providing negligible amounts of radioargon. Calculaton of the off-gas rate of radioargon produced in the reactor pool showed that over 99% of ^{37}Ar produced in the pool diffuses into the bulk air of the facility before decay, though the diffusion mechanisms do throttle the release rate.

Modeling of Ca activation in the biological shield show that beamport penetrations of the shield, and the resulting fast neutron flux interacting with the concrete, results in the largest single source of ^{37}Ar buildup. The predicted ^{37}Ar activity in the whole shield after an 8 hour operation was on the order of 1×10^{8} Bq. Accounting for the activation of air trapped in the concrete matrix had minimal effect on the total activity, though the contribution of the air was comparable to buildup in some of the other irradiation facilities. Analysis of the spatial distribution of buildup showed that the regions immediately surrounding the beamport penetration accounted for a significant portion of the total buildup.

The results predict a total ^{37}Ar buildup of $(5.877\pm0.40)\times10^{4}$ Bq·kWh^{-1} in the entire facility. Of this total, $(6.567\pm0.31)\times10^{2}$ Bq·kWh^{-1} occurred in the irradiation facilities and the reactor pool where the radioargon is expected to be collected in the bulk air of the facility relatively quickly after production.

For the $(5.811\pm0.40)\times10^{4}$ Bq·kWh^{-1} produced in the biological shield, only 0.1 - 3.5% was found to vent from the shield prior to decay. Exhalation times were on the order of tens of days for the ^{37}Ar activated from an 8 hour irradiation at 950 kW. The buildup of ^{37}Ar from activation of air trapped in the concrete of the biological shield was predicted to contribute less than 0.0001% of the total radioargon inventory in the shield.

Atmospheric transport modeling indicated that, under certain atmospheric conditions, full-power operation of the NETL TRIGA might produce ^{37}Ar concentrations detectable in a laboratory measurement system if samples are taken at the stack.

At 250 MW, even the Advanced Test Reactor would not produce field measurable concentrations at 10 km or beyond.

Published release data for ^{41}Ar produced in the NETL TRIGA was compared to the predicted buildup of ^{41}Ar in the facility. Normalizing the total ^{41}Ar released during quarters 1-3 of 2013 by the operation time during the same period, a release rate of 4.23×10^{5} Bq·kWh^{-1}. The modeled buildup rate was calculated to be $(4.32\pm0.24)\times10^{6}$ Bq·kWh^{-1}.

The proxy isotope method was presented as an alternative to direct characterization of a facility. Published radioxenon release values were collected for the High Flux Isotope Reactor and the depletion code was used to determine the operational parameters of the reactor that would produce the published radioxenon isotopic ratios. These parameters predicted an annual ^{37}Ar release from the facility on the order of 1×10^{10} Bq.

Volume normalization of the ^{37}Ar and ^{39}Ar buildup constants showed that a power law relationship holds between thermal flux and the buildup constant for air-filled regions where the thermal flux is not specifically filtered. Energy filtered facilities, like the Cd lined cavity of the PTS, produce higher radioargon activities than predicted by the thermal flux as a results of reactions in the epithermal range. A buildup constant for ^{37}Ar that could estimate the buildup in a region of some general thermal research reactor was calculated. For Ca-generated radioargon, a similar power law relationship was found to describe the buildup as a function of fast neutron flux. These power law relationships were simplified to show that the inventory in a given region can be reasonably estimated by solving Equation (3.2) for with only the radiative capture term (for air and water activation) or the (n,α) term for Ca activation.

The sensitivity of radioargon buildup to a number of operational and method-

ological changes was explored using the depletion code. High neutrons fluences were simulated to determine the fluence regime for which buildup behaves linear. In this regime, the buildup constants can be used to estimate the activity as a function of kWh. Buildup from air activation was found to agree with the constants within 5% for 120 hours of operation at 950 kW and within 10% for 233 hours of 950 kW operation. Limits for 5% and 10% agreement for buildup from Ca activation were found to be 128 hours and 244 hour, respectively.

The relative contributions of thermal neutrons (< 1 eV), epithermal neutrons (1 eV < E < 0.1 MeV), and fast neutrons (> 0.1 MeV) to the buildup from air activation was explored by adjusting the flux profile of the 3L facility. Reducing the epithermal flux to zero decreased the ^{37}Ar activity by 9.3% for an 8 hour irradiation. Excluding epithermal neutrons in the resonance regions for capture in the stable argon isotopes indicated that contributions to the buildup were evenly distributed between the resonance regions and sub-resonance regions. Excluding fast neutrons resulted in a negligible change in the buildup from air activation. For Ca activation in the biological shield, the fast neutron flux accounted for 85% of the ^{37}Ar buildup. Epithermal reactions accounted for the majority of the rest of the buildup, with thermal reactions contributing minimally.

For typical irradiation conditions in the reactor facility it was shown that radioargon buildup is dominated by radiative capture in the stable argon isotopes for air activation and by (n, α) reactions in Ca for interactions in the biological shield. Low-probability and threshold reactions in other species with similar A and Z to the radioargon isotopes contribute minimally to buildup and calculations excluding other isotopes and reactions produced results similar to the highest fidelity calculations. The relatively high concentration of stable Ar in air and stable Ca in concrete dominate the production even for high neutron fluence.

8.2 Conclusions

Each of the goals listed in Section 1.1 were addressed during the course of this research. The radiation transport software MCNPX was used to simulate the physics of the University of Texas at Austin's NETL TRIGA reactor, and the model was validated against a number of experimental results. The buildup rate of radioargon was calculated for the air-filled irradiation facilities, the reactor pool, and the biological shield. Based on these buildup rates, the release rate of ^{37}Ar was estimated. The depletion code, written to calculate the time-dependent radioargon concentration based on the MCNPX results, was used to explore the sensitivity of the buildup to changes in reactor operations, flux profiles, and the inclusion or exclusion of particular nuclear data. Generalized relationships for the buildup rate as a function of thermal or fast neutron flux were determined to allow estimation of the radioargon produced in other facilities. Finally, the source term calculated for the NETL TRIGA was used with the atmospheric transport code HYSPLIT to estimate the ground-level ^{37}Ar concentration around the facility. The conditions under which field-measurable concentrations would be produced were also determined.

The research included a number of other accomplishments not explicitly outlined in Section 1.1, including.

- Comprehensive review of work to date related to radioargon production and measurement.
- Collection of experimental data produced at the NETL TRIGA for reactor model benchmarking.
- Development of depletion code with flexibility to integrate arbitrary flux profiles and explore sensitivity to individual isotopes and reactions.

- Initial estimates of radioargon buildup in spent fuel due to ternary fission.

Ultimately this project was the first to address the relative contributions of noble gas production in a reactor. The results from the different regions of the reactor showed that no one mechanism dominated the radioargon source term. The results of buildup in the biological shield highlighted that there may be mechanisms that produce substantial amounts of gases that do no transport to the effluent stack for release. The diffusion mechanisms for the reactor pool and biological shield produce complicated time-dependent release trends during and after operation, as indicated in Figure 5.13.

The sensitivity analyses showed that the mathematics describing radioargon buildup are relatively simple, with single reactions accounting for nearly all of the buildup of ^{37}Ar, ^{39}Ar, and ^{41}Ar. As a result, knowledge of the thermal or fast flux in a particular volume in a facility would provide a highly accurate estimate of the time-dependent radioargon concentration.

Atmospheric transport results indicated that even high-power research reactor facilities are unlikely to produce field-detectable concentrations of ^{37}Ar at ground level for the current predicted MDCs of those measurement systems. Estimates based on the NETL TRIGA results and the IAEA RRDB indicated that research reactors are, as expected, a small source of ^{37}Ar relative to the likely production at nuclear power reactors.

8.3 Future Work

A substantial number of questions arose during the course of this work that could serve as the basis for future research. Additionally, portions of this work could be improved upon with focused study of those particular issues. The opportunities

for future work that offer the highest research impact are discussed in this section.

For any future work to characterize anthropogenic sources of radioargon, whether experimental or computational, the quality of results will be limited by evaluated nuclear data. Improvement of cross-section data for the radiative capture reactions in ^{36}Ar and ^{38}Ar would increase the precision of all future air activation work. Reconciliation of the discrepancies in ^{40}Ca(n,α)^{37}Ar data would dramatically improve confidence in results related to Ca-generated radioargon. Cross-section measurement campaigns are often driven by the demands of the user community, so discussion of the impact of cross-section uncertainty on the total uncertainty of future work is encouraged.

A major limitation on this project was the lack of easily accessible ^{37}Ar measurement systems. Collection and measurement of radioargon could have provided a stronger experimental basis to the results. The current state of ^{37}Ar measurement relies on ultra-high purity materials and sophisticated fabrication methods. Further, this capability is limited to a few facilities. Previous experiments that relied on radioargon measurements were able to measure medium-activity samples with relatively simple internal source proportional counters. Reclaiming a reliable measurement capability is highly recommend, and could open the door to a number of interesting experiments to investigate the production of radioargon in air, water, concrete, and other matrices.

In a similar vein, ternary fission data for ^{37}Ar has not been improved in over 40 years. Unintentional release of fission product gases has previously contributed to the inventory of radioactive noble gas effluent from a facility [67]. Knowledge of radioxenon fission product ratios was crucial for identifying the source of the gas in that case. In the case where the radioargon content of irradiated fuel is desired, ternary fission data might limit the precision to an order-of-magnitude estimate.

Although the results of this project represent the highest fidelity calculations of radioargon production in a reactor, the impact of the individual transport pathways from source to release warrants further work. For the case of an open pool reactor, the diffusion behavior of radioargon out of the pool may be generalized to other reactors, however many other transport pathways would have to be treated on a case-by-case basis due to differing reactor design and operation. For most pathways, the transport time is unlikely to be significant compared to the half-life of ^{37}Ar, though transport mechanisms could be responsible for discrepancies between calculated production rates and measured release rates. Further development of techniques blind to the transport mechanisms (such as the proxy isotope method described in Ref. [71]) would increase the confidence of results from both approaches.

The new capabilities for ^{37}Ar purification and measurement at Pacific Northwest National Laboratory could enable the collection of samples from an operating reactor. Based its accessibility and flexibility, the NETL TRIGA facility would be well-suited as the site of this collection. Proof-of-concept for a collection of experiment could be executed by collecting bulk air from the reactor bay during or after a reactor operation. With the venting systems for the reactor pool and bay closed, ^{37}Ar would build up in the bay and could be collected. Dose calculations would be necessary to ensure that simultaneous buildup of ^{41}Ar in the bay would not approach dose limits for experimenters.

Alternatively, a collection campaign could leverage the NETL TRIGA's radioargon purge system. The system consists of individual purge lines for each of the beamports, a purge line that pulls air off the top of the reactor pool, and large vents on the south wall of the reactor bay. The reactor pool purge and the reactor bay purge are vented to the stack. The beamport purge lines meet at a manifold at the ground-level of the biological shield and are consolidated into a single pipe for

venting to the stack.

The beamport purge manifold is accessible and could serve as the basis for small-scale, initial collections to verify the experimental plan for the whole facility. The individual lines of the manifold would be tapped to allow collection of samples directly from the pipe. An individual beamport would be plugged and the purge system for that beamport isolated from the main purge line (there are manual valves at the manifold controlling the venting of each beamport). The reactor would be operated to build up ^{37}Ar in the empty volume of the beamport, then the purge line could be vented into the collection volume. This approach would avoid the health physics considerations of allowing radioargon buildup in the reactor bay and could directly compared to buildup calculations in the beamports. Comparison of bay measurements would have to account for transport in the pool and the biological shield.

In total, the use of ^{37}Ar as a tracer for treaty monitoring has re-invigorated work related to the radioargon isotopes as a whole. Establishing fundamental, lab-accessible measurement capabilities, understanding the limitations of current radioargon nuclear data, and beginning experiments to collect ^{37}Ar from an operating reactor would provide a strong foundation for future work.

A | MCNPX - Reactor Model

This appendix provides the general input deck used for radiation transport calculations in this project. Commenting within the code has been reduced to only those comments that provide information useful to a secondary user. The geometry includes the full pool volume and biological shield. Individual tallies and temporary variance reduction implementations are excluded from this general input file. Test runs of the file were run using MCNPX version 2.7.0 on a quad-core 3.10 GHz machine running Windows 7. Complete runs were executed on the University of Texas at Austin Nuclear and Radiation Engineering Program's computer cluster, NUKESTAR.

```
--UT NETL TRIGA Reactor Deck--
c
c ********************* File Description ******************************
c
c This file is a working deck of the University of Texas' Nuclear
c  Engineering Teaching Laboratory MARK II TRIGA reactor. Please see
c  the accompanying TRIGA_Readme.txt file for a full description of
c  the deck and features.
c
c For reference, the origin (0,0,0) of the problem geoemtry corresponds
c  to the midplane of the central axis of the reactor core, as indicated
c on the elevation diagram of the reactor assembly.
c  The x-axis is chosen to be parallel with BP3, the y-axis parallel to
c  BPs 1&5. The vertical extent of the reactor is built in the z
c  direction. Following this convention, "right" and "left" refer to
c  +/-x, "up" and  "down" refer to +/-y, "top" and "bottom" refer
c  to +/-z.
c
c Some surfaces are transformed (particularly those not
c  parallel/perpendicular to any of the basis vectors. These surfaces
c  will be marked with the word TRANSFORMED in the comment,
c  and the associated TR card can be found in the
c  Data block. The TR card number is listed immediately after the surface
c  number and, in most cases, should match the surface number.
c
c Every cell is defined by surfaces. Macrobodies are not used.
c  The core grid is defined using inidividual fuel pins rather
```

```
c  than a lattice scheme. Individual tallies of items in a lattice
c  can be tedious, while individual pin construction offers a bit
c  more flexibility in tallying. That said, everything
c  done in this deck could be done in a lattice-oriented deck.
c
c The current pin positions occupied by the 3L irradiation facility are:
c  position   cell #   surface #   transformation #
c    E11       1348     848          348
c    F13       1374     874          374
c    F14       1375     875          375
c
c Transformations 302 - 427 are used for defining the fuel pins.
c  The universe containing the fuel pin is constructed in position B1.
c  It is composed of the fuel element surrounded by infinite water.
c  The TR cards 302 - 427 give the translations for each pin position
c  relative to B1. This is necessary because when you instruct MCNPX
c  to fill a cell with a universe, it does not align the center of the
c  universe with the center of that cell.
c  Instead, it fills that cell with the part of the universe that
c  coincides with the cell in the real coordinate frame. As a result,
c  we must translate the universe so it is centered in each fuel pin
c  cell so the fuel pin properly fills the cell. If we did not translate
c  the universe, each filled cell would only be filled with water
c  because the region in the real coordinate frame occupied by
c  our cell to be filled contains only water in the
c  fuel pin universe. This behavior can be inferred by looking at
c  the examples of universe fills in the Advanced Geometry
c  section of the LANL MCNPX training course notes.
c
c The transient control rod universe is built in the transient rod
c  position. Although it is not necessary to create transient rod
c  universe (because the universe is built in the transient rod
c  position and no other cells are filled with that universe u=3),
c  building it as a universe allows for easy movement of the entire
c  rod structure using the TR card associated with the universe fill.
c  This could also be accomplished without the use of
c  universes by using the TRCL option with the cell containing the
c  transient  rod. The fuel following control rod (RR, S1, S2) universe
c  is built in the Reg. rod position. The cells for S1 and S2 are filled
c  with the FFCR universe (u=2) with the appropriate TR cards.
c  Movement of the control rods is accomplished
c  by changing the z-value of the translation in the associated TR
c  card. By default the control rods are built in the "fully inserted"
c  position. When the rod is "fully withdrawn", the 15" following fuel
c  region of the rod aligns with the 15" fuel region of the fuel elements.
c  The rod has a 15" range of motion,
c  meaning that when "fully inserted", the 15" poison region of the rod
c  does not perfectly align with the 15" fuel element fuel region. The
c  poison region is offset above the FE fuel region because of the gap
c  between the poison and fuel/air follower in the rod. If the rods are
c  raised above full withdrawal (TR308/314/325/333 z-value > 38.1)
c  or pushed below full insert (z-value < 0) you are modeling behavior
c  that is not possible in the real NETL TRIGA reactor. The x and y values
c  SHOULD NOT be adjusted. The following  information might be useful:
c              Cell #   TR #  TR z-value full in   full out
c   Reg. rod    1314    314              0.0        38.1
c   Shim 1      1325    325              0.0        38.1
c   Shim 2      1333    333              0.0        38.1
c   Transient   1308    308              0.0        38.1
```

```
c
c Author: AG Fay
c
c
c   ***  Cell Cards ***
c
c  * Graveyard *
1     0             -114:115:116:-117:102:-103
                    :118:119:120:121:122:123:124:125       imp:n=0
c  * Bonus water region *
2     11 -0.998207  -106 107 108 -109 101 105 -102 103
                    #1050 #1051                            imp:n=1
c  * Pool liner left cylinder *
3     12 -2.700000  -110 101 -108 -102 103
                    #1060 #1061 #1062 #1063
                    #1070 #1071 #1080 #1081    imp:n=1
c  * Pool liner *
4     12 -2.700000  -111 105 109 -102 103                  imp:n=1
c  * Pool liner top *
5     12 -2.700000  108 -109 -112 106 -102 103
                    #1050 #1051                            imp:n=1
c  * Pool liner bottom *
6     12 -2.700000  108 -109 -107 113 -102 103
                    #1050 #1051                            imp:n=1
c  * Biological shield *
7     19 -4.040000  114 -115 -116 117 -120 -121
                    -122 -123 -118 -119 -124 -125
                    (110 111) (112:-113:-108:109)
                    #1050 #1051 #1052 #1053 #1054 #1055
                    #1056 #1057 #1058 #1059 #1060 #1061
                    #1062 #1063 #1064 #1065 #1066 #1067
                    #1068 #1069 #1070 #1071 #1074 #1075
                    #1080 #1081 #1084 #1085    imp:n=0
c  * Pool water outer cylinder *
2000  11 -0.998207  (-101:-105) 104 -102 103
                    #1001 #1002 #1003 #1004
                    #1005 #1006
                    #1008 #1009 #1010 #1020 #1021 #1050 #1051
                    #1060 #1061 #1070 #1071 #1072 #1073 #1080 #1081
                    #1082 #1083 #1022 #1023 #1036 #1086
                    #1062 #1063 (304:-301:307:-308)
                                              imp:n=1
c  * Pool water inner cylinder *
2001  11 -0.998207  -102 103 -104 #1001 #1002 #1005 #1006
                    #1004 #1008 #1009 #1010 #1020 #1021 #1050
                    #1070 #1071 #1072 #1073 #1302 #1303
                    #1304 #1305 #1306 #1307 #1308 #1309 #1310 #1311
                    #1312 #1313 #1315 #1316 #1317 #1318 #1319 #1320
                    #1321 #1322 #1323 #1324 #1326 #1327 #1328 #1329
                    #1330 #1331 #1332 #1334 #1335 #1336 #1337 #1338
                    #1339 #1340 #1341 #1342 #1343 #1344 #1345 #1346
                    #1347       #1349 #1350 #1351 #1352 #1353 #1354
                    #1355 #1356 #1357 #1358 #1359 #1360 #1361
                    #1362 #1363 #1364 #1365 #1366 #1367 #1367 #1368
                    #1369 #1370 #1371 #1372 #1373             #1376
                    #1377 #1378 #1379 #1380 #1381 #1382 #1383 #1384
                    #1385 #1386 #1387 #1388 #1389 #1390 #1391
                    #1393 #1394 #1395 #1396 #1397 #1399 #1400 #1401
                    #1402 #1403 #1405 #1406 #1407 #1408 #1409 #1411
```

```
                    #1412 #1413 #1414 #1415 #1417 #1418 #1419 #1420
                    #1421 #1424 #1426 #1427
                    #1314 #1325 #1333 #1036 #1040 #1041
                    #1060 #1061 #1062 #1063 #1086
                    #1190 #1191 #1192 #1193 #1194
                                            imp:n=1
c
c     * Grid Plates *
c  * Top grid plate *
1001  12 -2.700000  -131  132  -133
                     801 802 803 804 805 806 807 808 809 810
                     811 812 813 814 815 816 817 818 819 820
                     821 822 823 824 825 826 827 828 829 830
                     831 832 833 834 835 836 837 838 839 840
                     841 842 842 843 844 845 846 847 848 849
                     850 851 852 853 854 855 856 857 858 859
                     860 861 862 863 864 865 866 867 868 869
                     870 871 872 873 874 875 876 877 878 879
                     880 881 882 883 884 885 886 887 888 889
                     890 891 893 894 895 896 897 899 900 901
                     902 903 905 906 907 908 909 911 912 913
                     914 915 917 918 919 920 921 923 924 925
                     926 927 930 931 932 933 934 935 936 937
                     938 939 940 941 942 943 944 945 946 947
                     948 949 950 951 952 953 954 955 956 957
                     958 959 960 961 962 963 964 350
                                         imp:n=1
c  * Bottom grid plate *
1002   12 -2.700000  -134  135 137 -138 -139 140 -141 -142 -143
                     -144 -145 -146 -147 -148
                      801 802 803 804 805 806 807 808 809 810
                      811 812 813 814 815 816 817 818 819 820
                      821 822 823 824 825 826 827 828 829 830
                      831 832 833 834 835 836 837 838 839 840
                      841 842 842 843 844 845 846 847 848 849
                      850 851 852 853 854 855 856 857 858 859
                      860 861 862 863 864 865 866 867 868 869
                      870 871 872 873 874 875 876 877 878 879
                      880 881 882 883 884 885 886 887 888 889
                      890 891 893 894 895 896 897 899 900 901
                      902 903 905 906 907 908 909 911 912 913
                      914 915 917 918 919 920 921 923 924 925
                      926 927 930 931 932 933 934 935 936 937
                      938 939 940 941 942 943 944 945 946 947
                      948 949 950 951 952 953 954 955 956 957
                      958 959 960 961 962 963 964 965 966 967
                      968 969 970 971 972 973 974 imp:n=1
c
c     * Shrouds and Reflector Assemblies *
c  * Outer shroud *
1003   12 -2.700000  161 -162 -163 164 600 (610:167)
                       imp:n=1
c  * Inner shroud, main sleeve *
1004   12 -2.700000  -165 135
                     (167 -168 -169 170 -171 -172 -173 -174 -175 -176
                     -177 -178)
                     (-137:138:139:-140:141:142:143:144:145:146:147:148)
                      imp:n=1
c  * Foundation mount *
```

```
1005   12 -2.700000  (-167:168:169:-170:171:172:173:174:175:176:177:178)
                     -161 -280 281 imp:n=1
c  * Foundation mount lip *
1006   12 -2.700000  -161 282 -281 135 imp:n=1
c  * Top shroud top ring *
1008   12 -2.700000  (-137:138:139:-140:141:142:143:144:145:146:147:148)
                     -180 181 -182 (-132:133) (-183:165) #1004 imp:n=1
c  * Top shroud scoop *
1009   12 -2.700000  -165 185 -187 183 (-184:-182:186)  imp:n=1
c  * Top plate of top shroud *
1010   12 -2.700000  -161 187 -188 189   imp:n=1
c  * Reflector *
1020   14 -1.700000  -161 -189 280(-167:168:169:-170:171:172:173:174:
                  175:176:177:178) (187:-185) 600 (610:167) (620:-175)
                     (630:632) (-168:220:-221:222:-223:224)   imp:n=1
c  * Air cavity *
1021   10 -0.001205  -181 185 -183
                    (-167:168:169:-170:171:172:173:174:175:176:177:178)
                          imp:n=1
c
c     * RSR *
c  * RSR Housing *
1022   12 -2.700000  -305 300 -306 311 (309:302)
                     (-301:304:307:-308) (304:-303:307:-310) imp:n=1
c  * RSR cavity *
1023   10 -0.001205  -304 301 -307 310 (303:308)
                     #521 #522 #523 #524 #525 #526 #527 #528 #529 #530
                     #531 #532 #533 #534 #535 #536 #537 #538 #539 #540
                     #541 #542 #543 #544 #545 #546 #547 #548 #549 #550
                     #551 #552 #553 #554 #555 #556 #557 #558 #559 #560
                                                              imp:n=1
c  * RSR specimen cans *
521    12 -2.700000  -313 -315 317 (314:-316)          imp:n=1
522    like 521 but TRCL=(-0.41190    5.23371 0)
523    like 521 but TRCL=(-1.63747   10.33857 0)
524    like 521 but TRCL=(-3.64652   15.18884 0)
525    like 521 but TRCL=(-6.38958   19.66512 0)
526    like 521 but TRCL=(-9.79912   23.65718 0)
527    like 521 but TRCL=(-13.79118  27.06672 0)
528    like 521 but TRCL=(-18.26746  29.80978 0)
529    like 521 but TRCL=(-23.11773  31.81883 0)
530    like 521 but TRCL=(-28.22258  33.04440 0)
531    like 521 but TRCL=(-33.45630  33.45630 0)
532    like 521 but TRCL=(-38.69002  33.04440 0)
533    like 521 but TRCL=(-43.79487  31.81883 0)
534    like 521 but TRCL=(-48.64514  29.80978 0)
535    like 521 but TRCL=(-53.12142  27.06672 0)
536    like 521 but TRCL=(-57.11348  23.65718 0)
537    like 521 but TRCL=(-60.52302  19.66512 0)
538    like 521 but TRCL=(-63.26608  15.18884 0)
539    like 521 but TRCL=(-65.27513  10.33857 0)
540    like 521 but TRCL=(-66.50070   5.23372 0)
541    like 521 but TRCL=(-66.91260   0.00000 0)
542    like 521 but TRCL=(-66.50070  -5.23372 0)
543    like 521 but TRCL=(-65.27513 -10.33857 0)
544    like 521 but TRCL=(-63.26608 -15.18884 0)
545    like 521 but TRCL=(-60.52302 -19.66512 0)
546    like 521 but TRCL=(-57.11348 -23.65718 0)
```

```
547   like 521 but TRCL=(-53.12142 -27.06672 0)
548   like 521 but TRCL=(-48.64514 -29.80978 0)
549   like 521 but TRCL=(-43.79487 -31.81883 0)
550   like 521 but TRCL=(-38.69002 -33.04440 0)
551   like 521 but TRCL=(-33.45630 -33.45630 0)
552   like 521 but TRCL=(-28.22258 -33.04440 0)
553   like 521 but TRCL=(-23.11773 -31.81883 0)
554   like 521 but TRCL=(-18.26746 -29.80978 0)
555   like 521 but TRCL=(-13.79118 -27.06672 0)
556   like 521 but TRCL=(-9.79912  -23.65718 0)
557   like 521 but TRCL=(-6.38958  -19.66512 0)
558   like 521 but TRCL=(-3.64652  -15.18884 0)
559   like 521 but TRCL=(-1.63747  -10.33857 0)
560   like 521 but TRCL=(-0.41190   -5.23372 0)
c
c     * RSR Flux wires *
c 561    22 -2.707190  -290  291 -292        imp:n=1
c 562    22 -2.707190  -290  291 -293        imp:n=1
c 563    22 -2.707190  -290  291 -294        imp:n=1
c 564    22 -2.707190  -290  291 -295        imp:n=1
c
c     * 3L Facility *
c  * 3L tube *
1030   12 -2.700000  -334 -330 333 (335:331:-332)          u=4  imp:n=1
c  * Air cavity inside insert *
1031   10 -0.001205  -347 342 -331                         u=4  imp:n=1
c  * Insert *
1032   12 -2.700000  -340 -346 343 (347:-342)              u=4  imp:n=1
c  * Cd/Pb liner *
1033   20 -11.34000  -341 332 -345 (346:-343)              u=4  imp:n=1
c  * Air cavity outside insert *
1034   10 -0.001205  -335 347 -331 332 (345:341) (346:340)  u=4  imp:n=1
c  * External water *
1035   11 -0.998207  (334:330:-333)                       u=4  imp:n=1
c  * 3L Facility fill *
1036   0             -350 -102 134                     fill=4  imp:n=1
c
c     * Central Thimble *
c  * Al guide tube *
1040   12 -2.700000  -131 135 -320 321         imp:n=1
c  * Sample location *
1041   11 -0.998207  -323 325 -324               imp:n=1
c
c     * Beam Ports *
1050   12 -2.700000  -607 625 -600 601      imp:n=1  $ BP1/5 tube
1051   10 -0.001205  -607 625 -601  #1086   imp:n=1  $ BP1/5 tube cavity
1052   13 -8.000000  605 -606 607 -116      imp:n=1  $ BP1 stage 2 tube
1053   10 -0.001205  -605 607 -116          imp:n=1  $ BP1 stage 2 cavity
1054   13 -8.000000  605 -605 -625 626      imp:n=1  $ BP5 stage 2 tube
1055   10 -0.001205  -605 -625 626          imp:n=1  $ BP5 stage 2 cavity
1056   13 -8.000000  608 -609 -626 629      imp:n=1  $ BP5 stage 3 tube
1057   10 -0.001205  -608 -626 629          imp:n=1  $ BP5 stage 3 cavity
1058   13 -8.000000  627 -628 -629 117      imp:n=1  $ BP5 stage 4 tube
1059   10 -0.001205  -627 -629 117          imp:n=1  $ BP5 stage 4 cavity
1060   12 -2.700000  -162 -610 611 -167     imp:n=1  $ BP3 outer tube
1061   11 -0.998207  -162 -611 -167 613     imp:n=1  $ BP3 water cavity
1062   12 -2.700000   617 -613 614 -167     imp:n=1  $ BP3 inner tube
1063   10 -0.001205   617 -614 -167         imp:n=1  $ BP3 air cavity
```

```
1064   13 -8.000000  -617 636 615 -616      imp:n=1  $ BP3 stage 2 tube
1065   10 -0.001205  -617 636 -615          imp:n=1  $ BP3 stage 2 cavity
1066   13 -8.000000  -636 637 618 -619      imp:n=1  $ BP3 stage 3 tube
1067   10 -0.001205  -636 637 -618          imp:n=1  $ BP3 stage 3 cavity
1068   13 -8.000000  -637 114 638 -639      imp:n=1  $ BP3 stage 4 tube
1069   10 -0.001205  -637 114 -638          imp:n=1  $ BP3 stage 4 cavity
1070   12 -2.700000  -622 162 -620 621 175  imp:n=1  $ BP4 tube
1071   10 -0.001205  -622 162 -621 175      imp:n=1  $ BP4 cavity
1072   12 -2.700000  -161 -620 621 175      imp:n=1  $ Inner BP4 tube
1073   11 -0.998207  -161 -621 175 662      imp:n=1  $ Inner BP4 cavity
1074   13 -8.000000   623 -624 622 -123     imp:n=1  $ BP4 stage 2 tube
1075   10 -0.001205  -623 622 -123          imp:n=1  $ BP4 stage 2 cavity
1080   12 -2.700000   633 162 -630 631 -632 imp:n=1  $ BP2 tube
1081   10 -0.001205   633 162 -631 -632     imp:n=1  $ BP2 cavity
1082   12 -2.700000  -161 -630 631 -632     imp:n=1  $ Inner BP2 tube
1083   11 -0.998207  -161 -631 -632         imp:n=1  $ Inner BP2 cavity
1084   13 -8.000000   634 -635 -633 -124    imp:n=1  $ BP2 stage 2 tube
1085   10 -0.001205  -634 -633 -124         imp:n=1  $ BP2 stage 2 cavity
c
1086   14 -3.0000000 -602 223 -604          imp:n=1  $ Scattering block
c
c     * Beam Port Tally Cells
c 1091   10 -0.001205  -650            imp:n=1  $ BP1 sphere
c 1092   10 -0.001205  -654            imp:n=1  $ BP2 sphere
c 1093   10 -0.001205  -658            imp:n=1  $ BP3 sphere
c 1094   10 -0.001205  -662            imp:n=1  $ BP4 sphere
c 1095   10 -0.001205  -666            imp:n=1  $ BP5 sphere
c
c     * Fuel Element Universe - Pos. B1 *
1100   15 -5.890000  -500 510 -511 514     u=1  imp:n=1 $ FE fuel
1101   14 -1.700000  -500 -509 511         u=1  imp:n=1 $ Top reflector
1102   14 -1.700000  -500 505 -515         u=1  imp:n=1 $ Bottom reflector
1103   18 -6.506000  -510 -511 514         u=1  imp:n=1 $ Zirc tube
1104   10 -0.001205  -500 -504 509         u=1  imp:n=1 $ FE air cavity
1105   17 -10.22000  -500 515 -514         u=1  imp:n=1 $ Mo disc
1106   13 -8.000000   500 -501 -504 505    u=1  imp:n=1 $ FE cladding
c  * FE top tri-flute and pin *
1107   13 -8.000000 (-501 504 -503):(-508 503 -502)   u=1  imp:n=1
c  * FE bottom tri-flute and pin *
1108   13 -8.000000 (-501 -505 134):(-508 -134 135)   u=1  imp:n=1
c  * FE external water *
1109   11 -0.998207  (508:502:-135) (501:503:-134)    u=1  imp:n=1
c
c     * Fuel Following Control Rod Universe - RR/Pos. C7 *
1150   13 -8.000000  -401 410 413 -412    u=2  imp:n=1 $ SS cladding
1151   13 -8.000000  -400 401 -412        u=2  imp:n=1 $ Top fitting
1152   10 -0.001205  -413 -401 402        u=2  imp:n=1 $ Top air void
1153   13 -8.000000  -413 -402 403        u=2  imp:n=1 $ Upper plug
1154   10 -0.001205  -413 -403 405(414:404)  u=2  imp:n=1 $ Upper air gap
1155   16 -2.520000  -414 -404 405       u=2  imp:n=1 $ Poison region
1156   13 -8.000000  -413 -405 406       u=2  imp:n=1 $ Middle plug
1157   10 -0.001205  -413 -406 407       u=2  imp:n=1 $ Lower air gap
1158   15 -5.890000  -413 417 -407 408   u=2  imp:n=1 $ Fuel region
1159   18 -6.506000  -417 -407 408       u=2  imp:n=1 $ Zirc rod
1160   13 -8.000000  -413 -408 409       u=2  imp:n=1 $ Lower plug
1161   10 -0.001205  -416 -409 410       u=2  imp:n=1 $ Bottom air void
1162   12 -2.700000   416 -413 -409 410  u=2  imp:n=1 $ Bottom air void Al
```

```
1163   13 -8.000000  -412 -410 411       u=2  imp:n=1 $ Bottom fitting
1164   11 -0.998207  (412:400:-411)      u=2  imp:n=1 $ External water
c
c     * Transient/Air Following Control Rod - Pos. C1 *
1170   12 -2.700000  -426 427 -420 425    u=3  imp:n=1 $ Al cladding
1171   12 -2.700000  -427 -420 421        u=3  imp:n=1 $ Top fitting
1172   16 -2.520000  -428 -421 422        u=3  imp:n=1 $ B4C poison region
1173   10 -0.001205  -427 428 -421 422    u=3  imp:n=1 $ Air around B4C
1174   12 -2.700000  -427 -422 423        u=3  imp:n=1 $ Middle Al plug
1175   10 -0.001205  -427 -423 424        u=3  imp:n=1 $ Air void
1176   12 -2.700000  -427 -424 425        u=3  imp:n=1 $ Bottom fitting
1177   11 -0.998207  (426:420:-425)       u=3  imp:n=1 $ External water
c
c     * Test Universe - Graphite *
1180   14 -1.700000 -101 -102 103            u=4  imp:n=1 $ All graphite
c
c     * Pneumatic System *
1190   10 -0.001205  -369 370 -375            imp:n=1 $ Air cavity
1191   12 -2.700000  -368 371 -375 (369:-370) imp:n=1 $ Al sample tube
1192   23 -8.650000  -367 372 -375 (368:-371) imp:n=1 $ Cd sleeve
1193   10 -0.001205  -366 373 -375 (367:-372) imp:n=1 $ Air gap
1194   12 -2.700000  -365 374 -375 (366:-373) imp:n=1 $ Al transfer tube
c
c     * Fuel Elements/Control Rods *
1302   0          -802 -502 135 fill=1       imp:n=1  $ FE - B1
1303   0          -803 -502 135 fill=1 (303) imp:n=1  $ FE - B2
1304   0          -804 -502 135 fill=1 (304) imp:n=1  $ FE - B3
1305   0          -805 -502 135 fill=1 (305) imp:n=1  $ FE - B4
1306   0          -806 -502 135 fill=1 (306) imp:n=1  $ FE - B5
1307   0          -807 -502 135 fill=1 (307) imp:n=1  $ FE - B6
1308   0          -808 -102 103 fill=3 (308) imp:n=1  $ TR - C1
1309   0          -809 -502 135 fill=1 (309) imp:n=1  $ FE - C2
1310   0          -810 -502 135 fill=1 (310) imp:n=1  $ FE - C3
1311   0          -811 -502 135 fill=1 (311) imp:n=1  $ FE - C4
1312   0          -812 -502 135 fill=1 (312) imp:n=1  $ FE - C5
1313   0          -813 -502 135 fill=1 (313) imp:n=1  $ FE - C6
1314   0          -814 -102 103 fill=2 (314) imp:n=1  $ RR - C7
1315   0          -815 -502 135 fill=1 (315) imp:n=1  $ FE - C8
1316   0          -816 -502 135 fill=1 (316) imp:n=1  $ FE - C9
1317   0          -817 -502 135 fill=1 (317) imp:n=1  $ FE - C10
1318   0          -818 -502 135 fill=1 (318) imp:n=1  $ FE - C11
1319   0          -819 -502 135 fill=1 (319) imp:n=1  $ FE - C12
1320   0          -820 -502 135 fill=1 (320) imp:n=1  $ FE - D1
1321   0          -821 -502 135 fill=1 (321) imp:n=1  $ FE - D2
1322   0          -822 -502 135 fill=1 (322) imp:n=1  $ FE - D3
1323   0          -823 -502 135 fill=1 (323) imp:n=1  $ FE - D4
1324   0          -824 -502 135 fill=1 (324) imp:n=1  $ FE - D5
1325   0          -825 -102 103 fill=2 (325) imp:n=1  $ S1 - D6
1326   0          -826 -502 135 fill=1 (326) imp:n=1  $ FE - D7
1327   0          -827 -502 135 fill=1 (327) imp:n=1  $ FE - D8
1328   0          -828 -502 135 fill=1 (328) imp:n=1  $ FE - D9
1329   0          -829 -502 135 fill=1 (329) imp:n=1  $ FE - D10
1330   0          -830 -502 135 fill=1 (330) imp:n=1  $ FE - D11
1331   0          -831 -502 135 fill=1 (331) imp:n=1  $ FE - D12
1332   0          -832 -502 135 fill=1 (332) imp:n=1  $ FE - D13
1333   0          -833 -102 103 fill=2 (333) imp:n=1  $ S2 - D14
1334   0          -834 -502 135 fill=1 (334) imp:n=1  $ FE - D15
```

```
1335   0          -835 -502 135 fill=1 (335) imp:n=1  $ FE - D16
1336   0          -836 -502 135 fill=1 (336) imp:n=1  $ FE - D17
1337   0          -837 -502 135 fill=1 (337) imp:n=1  $ FE - D18
1338   0          -838 -502 135 fill=1 (338) imp:n=1  $ FE - E1
1339   0          -839 -502 135 fill=1 (339) imp:n=1  $ FE - E2
1340   0          -840 -502 135 fill=1 (340) imp:n=1  $ FE - E3
1341   0          -841 -502 135 fill=1 (341) imp:n=1  $ FE - E4
1342   0          -842 -502 135 fill=1 (342) imp:n=1  $ FE - E5
1343   0          -843 -502 135 fill=1 (343) imp:n=1  $ FE - E6
1344   0          -844 -502 135 fill=1 (344) imp:n=1  $ FE - E7
1345   0          -845 -502 135 fill=1 (345) imp:n=1  $ FE - E8
1346   0          -846 -502 135 fill=1 (346) imp:n=1  $ FE - E9
1347   0          -847 -502 135 fill=1 (347) imp:n=1  $ FE - E10
c 1348   0          -848 -502 135 fill=1 (348) imp:n=1  $ FE - E11 (3L)
1349   0          -849 -502 135 fill=1 (349) imp:n=1  $ FE - E12
1350   0          -850 -502 135 fill=1 (350) imp:n=1  $ FE - E13
1351   0          -851 -502 135 fill=1 (351) imp:n=1  $ FE - E14
1352   0          -852 -502 135 fill=1 (352) imp:n=1  $ FE - E15
1353   0          -853 -502 135 fill=1 (353) imp:n=1  $ FE - E16
1354   0          -854 -502 135 fill=1 (354) imp:n=1  $ FE - E17
1355   0          -855 -502 135 fill=1 (355) imp:n=1  $ FE - E18
1356   0          -856 -502 135 fill=1 (356) imp:n=1  $ FE - E19
1357   0          -857 -502 135 fill=1 (357) imp:n=1  $ FE - E20
1358   0          -858 -502 135 fill=1 (358) imp:n=1  $ FE - E21
1359   0          -859 -502 135 fill=1 (359) imp:n=1  $ FE - E22
1360   0          -860 -502 135 fill=1 (360) imp:n=1  $ FE - E23
1361   0          -861 -502 135 fill=1 (361) imp:n=1  $ FE - E24
1362   0          -862 -502 135 fill=1 (362) imp:n=1  $ FE - F1
1363   0          -863 -502 135 fill=1 (363) imp:n=1  $ FE - F2
1364   0          -864 -502 135 fill=1 (364) imp:n=1  $ FE - F3
1365   0          -865 -502 135 fill=1 (365) imp:n=1  $ FE - F4
1366   0          -866 -502 135 fill=1 (366) imp:n=1  $ FE - F5
1367   0          -867 -502 135 fill=1 (367) imp:n=1  $ FE - F6
1368   0          -868 -502 135 fill=1 (368) imp:n=1  $ FE - F7
1369   0          -869 -502 135 fill=1 (369) imp:n=1  $ FE - F8
1370   0          -870 -502 135 fill=1 (370) imp:n=1  $ FE - F9
1371   0          -871 -502 135 fill=1 (371) imp:n=1  $ FE - F10
1372   0          -872 -502 135 fill=1 (372) imp:n=1  $ FE - F11
1373   0          -873 -502 135 fill=1 (373) imp:n=1  $ FE - F12
c 1374   0          -874 -502 135 fill=1 (374) imp:n=1  $ FE - F13 (3L)
c 1375   0          -875 -502 135 fill=1 (375) imp:n=1  $ FE - F14 (3L)
1376   0          -876 -502 135 fill=1 (376) imp:n=1  $ FE - F15
1377   0          -877 -502 135 fill=1 (377) imp:n=1  $ FE - F16
1378   0          -878 -502 135 fill=1 (378) imp:n=1  $ FE - F17
1379   0          -879 -502 135 fill=1 (379) imp:n=1  $ FE - F18
1380   0          -880 -502 135 fill=1 (380) imp:n=1  $ FE - F19
1381   0          -881 -502 135 fill=1 (381) imp:n=1  $ FE - F20
1382   0          -882 -502 135 fill=1 (382) imp:n=1  $ FE - F21
1383   0          -883 -502 135 fill=1 (383) imp:n=1  $ FE - F22
1384   0          -884 -502 135 fill=1 (384) imp:n=1  $ FE - F23
1385   0          -885 -502 135 fill=1 (385) imp:n=1  $ FE - F24
1386   0          -886 -502 135 fill=1 (386) imp:n=1  $ FE - F25
1387   0          -887 -502 135 fill=1 (387) imp:n=1  $ FE - F26
1388   0          -888 -502 135 fill=1 (388) imp:n=1  $ FE - F27
1389   0          -889 -502 135 fill=1 (389) imp:n=1  $ FE - F28
1390   0          -890 -502 135 fill=1 (390) imp:n=1  $ FE - F29
1391   0          -891 -502 135 fill=1 (391) imp:n=1  $ FE - F30
```

```
1393   0          -893 -502 135 fill=1 (393) imp:n=1  $ FE - G2
1394   0          -894 -502 135 fill=1 (394) imp:n=1  $ FE - G3
1395   0          -895 -502 135 fill=1 (395) imp:n=1  $ FE - G4
1396   0          -896 -502 135 fill=1 (396) imp:n=1  $ FE - G5
1397   0          -897 -502 135 fill=1 (397) imp:n=1  $ FE - G6
1399   0          -899 -502 135 fill=1 (399) imp:n=1  $ FE - G8
1400   0          -900 -502 135 fill=1 (400) imp:n=1  $ FE - G9
1401   0          -901 -502 135 fill=1 (401) imp:n=1  $ FE - G10
1402   0          -902 -502 135 fill=1 (402) imp:n=1  $ FE - G11
1403   0          -903 -502 135 fill=1 (403) imp:n=1  $ FE - G12
1405   0          -905 -502 135 fill=1 (405) imp:n=1  $ FE - G14
1406   0          -906 -502 135 fill=1 (406) imp:n=1  $ FE - G15
1407   0          -907 -502 135 fill=1 (407) imp:n=1  $ FE - G16
1408   0          -908 -502 135 fill=1 (408) imp:n=1  $ FE - G17
1409   0          -909 -502 135 fill=1 (409) imp:n=1  $ FE - G18
1411   0          -911 -502 135 fill=1 (411) imp:n=1  $ FE - G20
1412   0          -912 -502 135 fill=1 (412) imp:n=1  $ FE - G21
1413   0          -913 -502 135 fill=1 (413) imp:n=1  $ FE - G22
1414   0          -914 -502 135 fill=1 (414) imp:n=1  $ FE - G23
1415   0          -915 -502 135 fill=1 (415) imp:n=1  $ FE - G24
1417   0          -917 -502 135 fill=1 (417) imp:n=1  $ FE - G26
1418   0          -918 -502 135 fill=1 (418) imp:n=1  $ FE - G27
1419   0          -919 -502 135 fill=1 (419) imp:n=1  $ FE - G28
1420   0          -920 -502 135 fill=1 (420) imp:n=1  $ FE - G29
1421   0          -921 -502 135 fill=1 (421) imp:n=1  $ FE - G30
c 1423   0          -923 -502 135 fill=1 (423) imp:n=1  $ Source - G32
1424   0          -924 -502 135 fill=1 (424) imp:n=1  $ FE - G33
c 1425   0          -925 -502 135 fill=1 (425) imp:n=1  $ PNT - G34
1426   0          -926 -502 135   fill=1 (426) imp:n=1  $ FE - G35
1427   0          -927 -502 135   fill=1 (427) imp:n=1  $ FE - G36

c   *** Surface Cards ***
c
c    ** Reactor Pool**
101 CZ 99.06
102 PZ 95
103 PZ -97.185
104 CZ 27
105 C/Z 99.06  0.0  99.06
106 PY  99.06
107 PY -99.06
108 PX  0.0
109 PX  99.06
c
c    ** Pool Liner **
110 CZ 100.33
111 C/Z 99.06  0.0  100.33
112 PY  100.33
113 PY -100.33
c
c    Bio Shield
c
114     PX    -342.90
115     PX     388.62
116     PY     342.90
117     PY    -342.90
118     P     1.732120  -1.00   0.00     760.9241    $ Lower right
119     P     0.577551  -1.00   0.00     422.3918    $ Lower right
```

```
120     P     1.732120   1.00   0.00     760.9241    $ Upper right
121     P     0.577551   1.00   0.00     422.3918    $ Upper right
122     P    -1.747154  -1.00   0.00     689.4911    $ Lower left
123     P    -0.577844  -1.00   0.00     396.0144    $ Lower left
124     P    -1.747154   1.00   0.00     689.4911    $ Upper left
125     P    -0.577844   1.00   0.00     396.0144    $ Upper left
c
c    ** Core Shrouds **
c     * Outer Shroud *
161   CZ   53.49875              $ Inner surface
162   CZ   54.76875              $ Outer surface
163   PZ   28.7401               $ Top plane
164   PZ  -32.2199               $ Bottom plane
c
c     * Inner Shroud *
c Inner surface planes defined by edges of bottom grid plate.
c  Outer plane #s defined as parallel inner surface plane # + 30.
165   PZ   28.9052               $ Top plane
c 166   PZ  -36.3474                $ Bottom plane (= 135)
167   PX  -25.4330               $ Left edge
168   PX   25.4330               $ Right edge
169   PY   26.7564               $ Up edge
170   PY  -26.7564               $ Down edge
171   P    0.57711   1.00000  0.0000  29.3636 $ Upper right long edge
172   P    1.723252  1.00000  0.0000  53.5234 $ Upper right short
173   P    1.723252 -1.00000  0.0000  53.5234 $ Lower right short
174   P    0.57711  -1.00000  0.0000  29.3636 $ Lower right long edge
175   P   -0.57711  -1.00000  0.0000  29.3636 $ Lower left long edge
176   P   -1.723252 -1.00000  0.0000  53.5234 $ Lower left short
177   P   -1.723252  1.00000  0.0000  53.5234 $ Upper left short
178   P   -0.57711   1.00000  0.0000  29.3636 $ Upper left long edge
c
c     * Top Shroud *
180   PZ   33.9852    $ Top of top shroud ring
181   PZ   26.3652    $ Bottom of top shroud ring
182   CZ   30.0831    $ Outer diameter of ring
183   CZ   29.4481    $ Outer cutout diameter
184   PZ    7.6327    $ Top of scoop bottom
185   PZ    6.9977    $ Bottom of scoop bottom
186   CZ   36.8300    $ Inside of outer scoop ring
187   CZ   37.4650    $ Outside of outer scoop ring
188   PZ   29.5402    $ Top of top plate
189   PZ   28.2702    $ Bottom of top plate
c
c    ** Reflector **
c  Reflector is currently defined by the inner and outer shrouds,
c   along with the top plate and beam port surfaces. See cell 1020.
c
c     * Cutout Port for BP1/5 *
220   PZ   1.415      $ Top of through port
221   PZ  -15.385     $ Bottom of through port
222   PY   9.525      $ Up side of through port
223   PY  -9.525      $ Down side of through port
224   PX   35.2552    $ End of through port
c
c    ** Foundation **
280   PZ  -27.94                 $ Top of mounting surface
281   PZ  -29.21                 $ Bottom of mounting surface
```

```
282   CZ   52.2288                $ IR of mounting surface lip
c
c    ** RSR **
300   PZ    8.90270   $ Bottom of bottom housing
301   PZ    9.53770   $ Top of bottom housing
302   PZ   34.03520   $ Bottom of step-out
303   PZ   36.35380   $ Top of step-out
304   PZ   43.66900   $ Bottom of top cap
305   PZ   44.46270   $ Top of top cap
306   CZ   36.67370   $ Outside of outer housing
307   CZ   36.03880   $ Inside of outer housing
308   CZ   30.87450   $ Inside of inner housing
309   CZ   30.23940   $ Outside of inner housing
310   CZ   28.27270   $ Inside of step-out
311   CZ   27.53760   $ Outside of step-out
313   C/Z  33.4563 0.0 1.74625  $ Outer tube surface
314   C/Z  33.4563 0.0 1.67259  $ Inner tube surface
315   PZ   40.1193    $ Top of speciman can
316   PZ   10.9550    $ Top of specimen can bottom
317   PZ   10.8077    $ Bottom of specimen can bottom
c
c    ** RSR flux wires **
c 290   PZ   12.4550                 $ RSR flux wire - upper bound
c 291   PZ   11.4550                 $ RSR flux wire - lower bound
c 292   C/Z  33.4563   0.0      0.1 $ RSR flux wire - pos.
c 293   C/Z  0.0     -33.4563   0.1 $ RSR flux wire - pos.
c 294   C/Z -33.4563   0.0      0.1 $ RSR flux wire - pos.
c 295   C/Z  0.0      33.4563   0.1 $ RSR flux wire - pos.
c
c    ** Central Thimble **
320     CZ      1.5000        $ Guide rod OD
321     CZ      1.4150        $ Guide rod ID
322     CZ      1.2500        $ Sample holder OD
323     CZ      1.1850        $ Sample holder ID
324     PZ      2.5000        $ Upper sample holder
325     PZ     -2.5000        $ Lower sample holder
c
c    ** 3L Irradiation Tube **
330  PZ   94.78010              $ Top of top fitting
331  PZ   91.60510              $ Bottom of top fitting/top of tube
332  PZ  -30.63240              $ Bottom of tube/top of bottom fitting
333  PZ  -33.17240              $ Bottom of bottom fitting
334  C/Z   8.79798 -15.23750  2.38125 $ Tube outer surface
335  C/Z   8.79798 -15.23750  2.23393 $ Tube inner surface
340  PZ   89.48420            $ Top of insert
341  PZ   87.57920            $ Top of Cd/Pb liner
342  PZ  -30.21330           $ Top surface of insert bottom
343  PZ  -30.53080           $ Top of Cd/Pb bottoms discs
344  PZ  -30.63240           $ Bottom of Cd/Pb bottom discs (= 332)
345  C/Z   8.79798 -15.23750  2.16535 $ Liner outer surface
346  C/Z   8.79798 -15.23750  2.06375 $ Insert outer surface
347  C/Z   8.79798 -15.23750  1.93929 $ Insert inner surface
350  C/Z   8.79798 -15.23750  2.40000 $ Cell for universe fill
c
360  PZ  10.3928                     $ 3L RR tally segmenting surfaces
361  PZ  50.9989
c 362  PZ -12.2133
c
```

```
c    ** Pneumatic Transfer System **
365  C/Z   -11.3106   19.5910   1.74625  $ Element G34, transfer tube OR
366  C/Z   -11.3106   19.5910   1.53543  $ Tube IR
367  C/Z   -11.3106   19.5910   1.16205  $ Cd liner
368  C/Z   -11.3106   19.5910   1.11125  $ Sample tube OR
369  C/Z   -11.3106   19.5910   0.86995  $ Sample tube IR
370  PZ    -2.07645               $ Top of sample tube bottom
371  PZ    -2.94775               $ Bottom of sample tube bottom
372  PZ    -2.99855               $ Bottom of Cd liner
373  PZ    -3.37193               $ Top of transfer tube bottom
374  PZ    -3.58275               $ Bottom of transfer tube bottom
375  PZ     50.0000               $ Top cutoff
c
c    ** Control Rods **
c     * Fuel Follower *
400  PZ     39.62810        $ Top of top fitting/top of everything
401  PZ     38.35810        $ Bottom of top fitting/top of air void
402  PZ     21.84810        $ Bottom of air void/top of plug
403  PZ     20.57810        $ Bottom of plug/top of air gap
404  PZ     20.27310        $ Bottom of air gap/top of B4C
405  PZ    -17.82690       $ Bottom of B4C/top of plug
406  PZ    -19.09690       $ Bottom of plug/top of air gap
407  PZ    -19.73190       $ Bottom of air gap/top of fuel (= 514)
408  PZ    -57.83190       $ Bottom of fuel/top of plug
409  PZ    -60.37190       $ Bottom of plug/top of air void
410  PZ    -76.88190       $ Bottom of air void/top of lower fitting
411  PZ    -78.15190       $ Bottom of lower fitting/bottom of everything
412  C/Z     0.00000 -8.70712  1.71450  $ Cladding outer radius
413  C/Z     0.00000 -8.70712  1.66350  $ Cladding inner radius
414  C/Z     0.00000 -8.70712  1.50749  $ Poison outer radius
c 415  C/Z     0.00000 -8.70712  1.66350  $ Fuel outer radius (= 413)
416  C/Z     0.00000 -8.70712  1.57460  $ Aluminum sleeve inner radius
417  C/Z     0.00000 -8.70712  0.28500  $ Zirc rod surface
c
c     * Transient/Air Follower *
420  PZ     24.71810    $ Top of top fitting/top of everything
421  PZ     20.90810    $ Bottom of top fitting/top of B4C
422  PZ    -17.19190    $ Bottom of B4C/top of Al plug
423  PZ    -19.73190    $ Bottom of Al plug/top of air void (= 514)
424  PZ    -72.76210    $ Bottom of air void/top of bottom fitting
425  PZ    -74.03710    $ Bottom of bottom fitting/bottom of everything
426  C/Z     0.00000  8.70712  1.58750  $ Cladding outer radius
427  C/Z     0.00000  8.70712  1.55200  $ Cladding inner radius
428  C/Z     0.00000  8.70712  1.51130  $ Poison outer radius
c
c    ** Fuel Element **
c  *
500  C/Z    0.00000  4.35356  1.8161  $ Inner surface
501  C/Z    0.00000  4.35356  1.8669  $ Outer surface
502  PZ    35.9297             $ Top plane
503  PZ    31.7387             $ Top of top tri-flute
504  PZ    27.6366             $ Top of cladded region
505  PZ   -28.4974             $ Bottom of cladded region
c 506   PZ  -33.1724           $ Bottom of bottom triflute (SAME AS 134)
c 507   PZ  -36.3474           $ Bottom plane (SAME AS 135)
508  C/Z    0.00000  4.35356  0.7874  $ End pin surface
509  PZ    27.0549                   $ Bottom of air gap
```

```
510  C/Z    0.00000  4.35356  0.2850  $ Zirc rod surface
511  PZ    18.3681                   $ Top of F3/bottom of top reflector
c                        $ Left blank in case you want to
c                        $  divide the pellets using surfaces 512/513
514  PZ   -19.7319            $ Top of Mo disc/bottom of F1
515  PZ   -19.8106            $ Top of bottom reflector/bottom of Mo disc
c
c
c    ** Beam Ports **
c     * BP 1&5 *
600  C/Y  35.2552  -6.985  8.41375    $ Reflector tube - Outer surface
601  C/Y  35.2552  -6.985  7.77875    $ Reflector tube - Inner surface
605  C/Y  35.2552  -6.985  10.31875   $ S2 tube inner surface
606  C/Y  35.2552  -6.985  10.95375   $ S2 tube outer surface
607  PY   180                         $ Stage 1/2 divider
608  C/Y  35.2552  -6.985  15.5575    $ S3 tube inner surface
609  C/Y  35.2552  -6.985  16.19250   $ S3 tube outer surface
625  PY   -123.19                     $ Stage 1/2
626  PY   -167.64                     $ Stage 2/3
627  C/Y  35.2552  -6.985  19.6850    $ S4 tube inner surface
628  C/Y  35.2552  -6.985  20.320     $ S4 tube outer surface
629  PY  -251.46                      $ Stage 3/4 divider
c
602  PY  -2.54                        $ Scatter block begin
604  C/Y  35.2552  -6.985  6.35       $ Scatter block OR
c
c     * BP 3 *
610  C/X   0.0000  -6.985  10.16    $ Reflector tube - Outer surface
611  C/X   0.0000  -6.985  9.525    $ Reflector tube - Inner surface
613  C/X   0.0000  -6.985  8.41375  $ BP tube - Outer surface
614  C/X   0.0000  -6.985  7.70255  $ BP tube - Inner surface
615  C/X   0.0000  -6.985  10.31875 $ S2 tube inner surface
616  C/X   0.0000  -6.985  10.95375 $ S2 tube outer surface
617  PX   -123.19                   $ Stage 1/2 divider
618  C/X   0.0000  -6.985  15.5575  $ S3 tube inner surface
619  C/X   0.0000  -6.985  16.19250 $ S3 tube outer surface
636  PX   -167.64                   $ Stage 2/3
637  PX   -251.46                   $ Stage 3/4
638  C/X   0.0000  -6.985  19.6850  $ S4 tube inner surface
639  C/X   0.0000  -6.985  20.320   $ S4 tube outer surface
c
c     * BP 4 *
620 620  CX   8.41375   $ Refl. tube - Untransformed outer surface
621 621  CX   7.77875   $ Refl. tube - Untransformed inner surface
c  * Stage 1/2 divider - TRANSFORMED *
622 622  P   -0.57711  -1.00000  0.0000  28.6332
623 623  CX   10.31875   $ S2 tube outer surface - TRANSFORMED
624 624  CX   10.95375   $ Refl. tube inner surface - TRANSFORMED
c
c     * BP 2 *
630 630  CX   8.41375   $ Refl. tube outer surface - TRANSFORMED
631 631  CX   7.77875   $ Refl. tube inner surface - TRANSFORMED
632 632  PX   0.00000   $ End cutoff plane - TRANSFORMED
633 633  PX   0.00000   $ Stage 1/2 divider - TRANSFORMED
634 634  CX   10.31875   $ S2 tube outer surface - TRANSFORMED
635 635  CX   10.95375   $ Refl. tube inner surface - TRANSFORMED
c
c     * BP Tallies
```

```
650 S  35.2552  54.0  -6.985  2.5  $ BP1 tally
654 S -30.0     56.0  -6.985  2.5  $ BP2 tally
658 S -65.0      0.0  -6.985  2.5  $ BP3 tally
662 S -33.0    -56.0  -6.985  2.5  $ BP4 tally
666 S  35.2552 -54.0  -6.985  2.5  $ BP5 tally
c
671  CZ  40.2887                $ Segmenting surface for BP3 tally
672  CZ  55.1444                $ Segmenting surface for BP3 tally
c
c
c    ** Grid Plates **
c     * Top Plate *
131   PZ   32.3850               $ Top surface of top grid plate
132   PZ   30.8102               $ Bottom of top grid plate
133   CZ   27.6225               $ Top grid plate radius
c
c     * Bottom Plate *
c The slope of the long sides are +/- 0.57711
c The slope of the short sides are +/- 1.73252
c These slopes can be used to calculate the planes bounding the GP.
c The edge of the GP is 2.16678 cm from the center of pin holes.
134   PZ  -33.1724        $ Top of bottom grid plate
135   PZ  -36.3474        $ Bottom of bottom grid plate
137   PX  -24.7980        $ Left edge
138   PX   24.7980         $ Right edge
139   PY   26.1214         $ Up edge
140   PY  -26.1214        $ Down edge
141   P    0.57711   1.00000  0.0000  28.6332 $ Upper right long edge
142   P    1.723252  1.00000  0.0000  52.2533 $ Upper right short
143   P    1.723252 -1.00000  0.0000  52.2533 $ Lower right short
144   P    0.57711  -1.00000  0.0000  28.6332 $ Lower right long edge
145   P   -0.57711  -1.00000  0.0000  28.6332 $ Lower left long edge
146   P   -1.723252 -1.00000  0.0000  52.2533 $ Lower left short
147   P   -1.723252  1.00000  0.0000  52.2533 $ Upper left short
148   P   -0.57711   1.00000  0.0000  28.6332 $ Upper left long edge
c
c    ** Grid Plate Holes - Top **
c     * Fuel Pin Holes *
801  CZ                       1.91135  $ A1
802  C/Z    0.00000   4.35356 1.91135  $ B1
803  C/Z    3.76936   2.17678 1.91135  $ B2
804  C/Z    3.76936  -2.17678 1.91135  $ B3
805  C/Z    0.00000  -4.35356 1.91135  $ B4
806  C/Z   -3.76936  -2.17678 1.91135  $ B5
807  C/Z   -3.76936   2.17678 1.91135  $ B6
808  C/Z    0.00000   8.70712 1.91135  $ C1
809  C/Z    3.76936   6.53034 1.91135  $ C2
810  C/Z    7.54126   4.35356 1.91135  $ C3
811  C/Z    7.54126   0.00000 1.91135  $ C4
812  C/Z    7.54126  -4.35356 1.91135  $ C5
813  C/Z    3.76936  -6.53034 1.91135  $ C6
814  C/Z    0.00000  -8.70712 1.91135  $ C7
815  C/Z   -3.76936  -6.53034 1.91135  $ C8
816  C/Z   -7.54126  -4.35356 1.91135  $ C9
817  C/Z   -7.54126   0.00000 1.91135  $ C10
818  C/Z   -7.54126   4.35356 1.91135  $ C11
819  C/Z   -3.76936   6.53034 1.91135  $ C12
820  C/Z    0.00000   13.0607 1.91135  $ D1
```

```
821  C/Z    3.76936   10.8839 1.91135  $ D2
822  C/Z    7.54126   8.70712 1.91135  $ D3
823  C/Z    11.3106   6.53034 1.91135  $ D4
824  C/Z    11.3106   2.17678 1.91135  $ D5
825  C/Z    11.3106  -2.17678 1.91135  $ D6
826  C/Z    11.3016  -6.53034 1.91135  $ D7
827  C/Z    7.54126  -8.70712 1.91135  $ D8
828  C/Z    3.76936  -10.8839 1.91135  $ D9
829  C/Z    0.00000  -13.0607 1.91135  $ D10
830  C/Z   -3.76936  -10.8839 1.91135  $ D11
831  C/Z   -7.54126  -8.70712 1.91135  $ D12
832  C/Z   -11.3016  -6.53034 1.91135  $ D13
833  C/Z   -11.3106  -2.17678 1.91135  $ D14
834  C/Z   -11.3106   2.17678 1.91135  $ D15
835  C/Z   -11.3106   6.53034 1.91135  $ D16
836  C/Z   -7.54126   8.70712 1.91135  $ D17
837  C/Z   -3.76936   10.8839 1.91135  $ D18
838  C/Z    0.00000   17.4142 1.91135  $ E1
839  C/Z    3.76936   15.2375 1.91135  $ E2
840  C/Z    7.54126   13.0607 1.91135  $ E3
841  C/Z    11.3106   10.8839 1.91135  $ E4
842  C/Z    15.0825   8.70712 1.91135  $ E5
843  C/Z    15.0825   4.35356 1.91135  $ E6
844  C/Z    15.0825   0.00000 1.91135  $ E7
845  C/Z    15.0825  -4.35356 1.91135  $ E8
846  C/Z    15.0825  -8.70712 1.91135  $ E9
847  C/Z    11.3106  -10.8839 1.91135  $ E10
848  C/Z    7.54126  -13.0607 1.91135  $ E11
849  C/Z    3.76936  -15.2375 1.91135  $ E12
850  C/Z    0.00000  -17.4142 1.91135  $ E13
851  C/Z   -3.76936  -15.2375 1.91135  $ E14
852  C/Z   -7.54126  -13.0607 1.91135  $ E15
853  C/Z   -11.3106  -10.8839 1.91135  $ E16
854  C/Z   -15.0825  -8.70712 1.91135  $ E17
855  C/Z   -15.0825  -4.35356 1.91135  $ E18
856  C/Z   -15.0825   0.00000 1.91135  $ E19
857  C/Z   -15.0825   4.35356 1.91135  $ E20
858  C/Z   -15.0825   8.70712 1.91135  $ E21
859  C/Z   -11.3106   10.8839 1.91135  $ E22
860  C/Z   -7.54126   13.0607 1.91135  $ E23
861  C/Z   -3.76936   15.2375 1.91135  $ E24
862  C/Z    0.00000   21.7678 1.91135  $ F1
863  C/Z    3.76936   19.5910 1.91135  $ F2
864  C/Z    7.54126   17.4142 1.91135  $ F3
865  C/Z    11.3106   15.2375 1.91135  $ F4
866  C/Z    15.0825   13.0607 1.91135  $ F5
867  C/Z    18.8519   10.8839 1.91135  $ F6
868  C/Z    18.8519   6.53034 1.91135  $ F7
869  C/Z    18.8519   2.17678 1.91135  $ F8
870  C/Z    18.8519  -2.17678 1.91135  $ F9
871  C/Z    18.8519  -6.53034 1.91135  $ F10
872  C/Z    18.8519  -10.8839 1.91135  $ F11
873  C/Z    15.0825  -13.0607 1.91135  $ F12
874  C/Z    11.3106  -15.2375 1.91135  $ F13
875  C/Z    7.54126  -17.4142 1.91135  $ F14
876  C/Z    3.76936  -19.5910 1.91135  $ F15
877  C/Z    0.00000  -21.7678 1.91135  $ F16
```

```
878  C/Z   -3.76936  -19.5910 1.91135  $ F17
879  C/Z   -7.54126  -17.4142 1.91135  $ F18
880  C/Z   -11.3106  -15.2375 1.91135  $ F19
881  C/Z   -15.0825  -13.0607 1.91135  $ F20
882  C/Z   -18.8519  -10.8839 1.91135  $ F21
883  C/Z   -18.8519  -6.53034 1.91135  $ F22
884  C/Z   -18.8519  -2.17678 1.91135  $ F23
885  C/Z   -18.8519   2.17678 1.91135  $ F24
886  C/Z   -18.8519   6.53034 1.91135  $ F25
887  C/Z   -18.8519   10.8839 1.91135  $ F26
888  C/Z   -15.0825   13.0607 1.91135  $ F27
889  C/Z   -11.3106   15.2375 1.91135  $ F28
890  C/Z   -7.54126   17.4142 1.91135  $ F29
891  C/Z   -3.76936   19.5910 1.91135  $ F30
893  C/Z    3.76936   23.9446 1.91135  $ G2
894  C/Z    7.54126   21.7678 1.91135  $ G3
895  C/Z    11.3106   19.5910 1.91135  $ G4
896  C/Z    15.0825   17.4142 1.91135  $ G5
897  C/Z    18.8519   15.2375 1.91135  $ G6
899  C/Z    22.6212   8.70712 1.91135  $ G8
900  C/Z    22.6212   4.35356 1.91135  $ G9
901  C/Z    22.6212   0.00000 1.91135  $ G10
902  C/Z    22.6212  -4.35356 1.91135  $ G11
903  C/Z    22.6212  -8.70712 1.91135  $ G12
905  C/Z    18.8519  -15.2375 1.91135  $ G14
906  C/Z    15.0825  -17.4142 1.91135  $ G15
907  C/Z    11.3106  -19.5910 1.91135  $ G16
908  C/Z    7.54126  -21.7678 1.91135  $ G17
909  C/Z    3.76936  -23.9446 1.91135  $ G18
911  C/Z   -3.76936  -23.9446 1.91135  $ G20
912  C/Z   -7.54126  -21.7678 1.91135  $ G21
913  C/Z   -11.3106  -19.5910 1.91135  $ G22
914  C/Z   -15.0825  -17.4142 1.91135  $ G23
915  C/Z   -18.8519  -15.2375 1.91135  $ G24
917  C/Z   -22.6212  -8.70712 1.91135  $ G26
918  C/Z   -22.6212  -4.35356 1.91135  $ G27
919  C/Z   -22.6212   0.00000 1.91135  $ G28
920  C/Z   -22.6212   4.35356 1.91135  $ G29
921  C/Z   -22.6212   8.70712 1.91135  $ G30
923  C/Z   -18.8519   15.2375 1.91135  $ G32
924  C/Z   -15.0825   17.4142 1.91135  $ G33
925  C/Z   -11.3106   19.5910 1.91135  $ G34
926  C/Z   -7.54126   21.7678 1.91135  $ G35
927  C/Z   -3.76936   23.9446 1.91135  $ G36
c
c     * Other Holes *
930  C/Z   -21.7170   12.5476 0.79375  $ Sa (top)
931  C/Z    21.7170  -12.5476 0.79375  $ Sb (top)
932  C/Z    13.3350   23.0962 0.51594  $ Ra (top)
933  C/Z    13.3350  -23.0962 0.51594  $ Rb (top)
934  C/Z   -13.3350  -23.0962 0.51594  $ Rc (top)
935  C/Z   -13.3350   23.0962 0.51594  $ Rd (top)
936  C/Z    26.6700   0.00000 0.51594  $ Pa (top)
937  C/Z   -26.6700   0.00000 0.51594  $ Pb (top)
938  C/Z    26.6700  -1.11252 0.31750  $ Na (top)
939  C/Z   -26.6700  -1.11252 0.31750  $ Nb (top)
940  C/Z    1.25730   6.53034 0.25781  $ Ha
```

```
941  C/Z    1.25730  -6.53034 0.25781  $ Hb
942  C/Z    1.25730   10.8839 0.25781  $ Ja
943  C/Z    1.25730  -10.8839 0.25781  $ Jb
944  C/Z    1.25730   15.2375 0.25781  $ Ka
945  C/Z    1.25730  -15.2375 0.25781  $ Kb
946  C/Z    1.25730   19.5910 0.25781  $ La
947  C/Z    1.25730  -19.5910 0.25781  $ Lb
948  C/Z    1.25730   23.9446 0.25781  $ Ma
949  C/Z    1.25730  -23.9446 0.25781  $ Mb
950  C/Z    6.28396  -2.17678 0.25781  $ Ba
951  C/Z   -6.28396  -2.17678 0.25781  $ Bb
952  C/Z    8.79856  -2.17678 0.25781  $ Ca
953  C/Z   -8.79856  -2.17678 0.25781  $ Cb
954  C/Z    13.8252  -2.17678 0.25781  $ Da
955  C/Z   -13.8252  -2.17678 0.25781  $ Db
956  C/Z    16.3398  -2.17678 0.25781  $ Ea
957  C/Z   -16.3398  -2.17678 0.25781  $ Eb
958  C/Z    21.3639  -2.17678 0.25781  $ Fa
959  C/Z   -21.3639  -2.17678 0.25781  $ Fb
960  C/Z    23.8785  -2.17678 0.25781  $ Ga
961  C/Z   -23.8785  -2.17678 0.25781  $ Gb
962  C/Z    1.25730   2.17678 0.25781  $ Aa
963  C/Z    1.25730  -2.17678 0.25781  $ Ab
964  C/Z   -1.25730  -2.17678 0.25781  $ Ac
965  C/Z    21.9964   12.7000 0.51594  $ Ra (bot)
966  C/Z    21.9964  -12.7000 0.51594  $ Rb (bot)
967  C/Z   -21.9964  -12.7000 0.51594  $ Rc (bot)
968  C/Z   -21.9964   12.7000 0.51594  $ Rd (bot)
969  C/Z    0.00000   25.4000 0.51594  $ Pa (bot)
970  C/Z    0.00000  -25.4000 0.51594  $ Pb (bot)
971  C/Z    1.11252   25.4000 0.39687  $ Na (bot)
972  C/Z    1.11252  -25.4000 0.39687  $ Nb (bot)
973  C/Z   -8.79856   10.8839 0.55562  $ S (bot)
974  C/Z    8.79856  -15.2375 0.55562  $ T (bot)
c

c ------------------------------------------------------
c   *** Data Cards ***
c
c    ** General Physics **
MODE N
c  * -102, Analog sampling, models only, multigroup emission *
PHYS:P  100 0 0 0 1 -101
c
c    ** Weight Windows **
c WWP:N 5 3 5 0 -1 0
c WWG 15 2001
c
c    ** Tallies **
c
c
c    ** Criticality **
KCODE 100000 1.0 30 110
KSRC   3.76936  6.53034 0.0   $ C12
       3.76936 -6.53034 0.0   $ C2
      -3.76936 -6.53034 0.0   $ C6
      -3.76936  6.53034 0.0   $ C8
       11.3106   10.8839 0.0  $ E4
```

```
 11.3106  -10.8839 0.0  $ E10
-11.3106  -10.8839 0.0  $ E16
-11.3106   10.8839 0.0  $ E22
 11.3106   19.5910 0.0  $ G4
 11.3106  -19.5910 0.0  $ G16
-11.3106  -19.5910 0.0  $ G22
 0.00000   4.35356 0.0  $ B1
 3.76936   2.17678 0.0  $ B2
 3.76936  -2.17678 0.0  $ B3
 0.00000  -4.35356 0.0  $ B4
-3.76936  -2.17678 0.0  $ B5
-3.76936   2.17678 0.0  $ B6
 7.54126   4.35356 0.0  $ C3
 7.54126   0.00000 0.0  $ C4
 7.54126  -4.35356 0.0  $ C5
-7.54126  -4.35356 0.0  $ C9
-7.54126   0.00000 0.0  $ C10
-7.54126   4.35356 0.0  $ C11
 0.00000   13.0607 0.0  $ D1
 3.76936   10.8839 0.0  $ D2
 7.54126   8.70712 0.0  $ D3
 11.3106   6.53034 0.0  $ D4
 11.3106   2.17678 0.0  $ D5
 11.3016  -6.53034 0.0  $ D7
 7.54126  -8.70712 0.0  $ D8
 3.76936  -10.8839 0.0  $ D9
 0.00000  -13.0607 0.0  $ D10
-3.76936  -10.8839 0.0  $ D11
-7.54126  -8.70712 0.0  $ D12
-11.3016  -6.53034 0.0  $ D13
-11.3106   2.17678 0.0  $ D15
-11.3106   6.53034 0.0  $ D16
-7.54126   8.70712 0.0  $ D17
-3.76936   10.8839 0.0  $ D18
 0.00000   17.4142 0.0  $ E1
 3.76936   15.2375 0.0  $ E2
 7.54126   13.0607 0.0  $ E3
 15.0825   8.70712 0.0  $ E5
 15.0825   4.35356 0.0  $ E6
 15.0825   0.00000 0.0  $ E7
 15.0825  -4.35356 0.0  $ E8
 15.0825  -8.70712 0.0  $ E9
 3.76936  -15.2375 0.0  $ E12
 0.00000  -17.4142 0.0  $ E13
-3.76936  -15.2375 0.0  $ E14
-7.54126  -13.0607 0.0  $ E15
-15.0825  -8.70712 0.0  $ E17
-15.0825  -4.35356 0.0  $ E18
-15.0825   0.00000 0.0  $ E19
-15.0825   4.35356 0.0  $ E20
-15.0825   8.70712 0.0  $ E21
-7.54126   13.0607 0.0  $ E23
-3.76936   15.2375 0.0  $ E24
 0.00000   21.7678 0.0  $ F1
 3.76936   19.5910 0.0  $ F2
 7.54126   17.4142 0.0  $ F3
 11.3106   15.2375 0.0  $ F4
```

```
        15.0825   13.0607 0.0  $ F5
        18.8519   10.8839 0.0  $ F6
        18.8519   6.53034 0.0  $ F7
        18.8519   2.17678 0.0  $ F8
        18.8519  -2.17678 0.0  $ F9
        18.8519  -6.53034 0.0  $ F10
        18.8519  -10.8839 0.0  $ F11
        15.0825  -13.0607 0.0  $ F12
        3.76936  -19.5910 0.0  $ F15
        0.00000  -21.7678 0.0  $ F16
       -3.76936  -19.5910 0.0  $ F17
       -7.54126  -17.4142 0.0  $ F18
       -11.3106  -15.2375 0.0  $ F19
       -15.0825  -13.0607 0.0  $ F20
       -18.8519  -10.8839 0.0  $ F21
       -18.8519  -6.53034 0.0  $ F22
       -18.8519  -2.17678 0.0  $ F23
       -18.8519   2.17678 0.0  $ F24
       -18.8519   6.53034 0.0  $ F25
       -18.8519   10.8839 0.0  $ F26
       -15.0825   13.0607 0.0  $ F27
       -11.3106   15.2375 0.0  $ F28
       -7.54126   17.4142 0.0  $ F29
       -3.76936   19.5910 0.0  $ F30
        3.76936   23.9446 0.0  $ G2
        7.54126   21.7678 0.0  $ G3
        15.0825   17.4142 0.0  $ G5
        18.8519   15.2375 0.0  $ G6
        22.6212   8.70712 0.0  $ G8
        22.6212   4.35356 0.0  $ G9
        22.6212   0.00000 0.0  $ G10
        22.6212  -4.35356 0.0  $ G11
        22.6212  -8.70712 0.0  $ G12
        18.8519  -15.2375 0.0  $ G14
        15.0825  -17.4142 0.0  $ G1
        7.54126  -21.7678 0.0  $ G17
        3.76936  -23.9446 0.0  $ G18
       -3.76936  -23.9446 0.0  $ G20
       -7.54126  -21.7678 0.0  $ G21
       -15.0825  -17.4142 0.0  $ G23
       -18.8519  -15.2375 0.0  $ G24
       -22.6212  -8.70712 0.0  $ G26
       -22.6212  -4.35356 0.0  $ G27
       -22.6212   0.00000 0.0  $ G28
       -22.6212   4.35356 0.0  $ G29
       -22.6212   8.70712 0.0  $ G30
       -15.0825   17.4142 0.0  $ G33
       -7.54126   21.7678 0.0  $ G35
       -3.76936   23.9446 0.0  $ G36
c
c    ** Material Cards **
c     * AIR *
M10   6000    0.000150   $ carbon
      7014    0.784431   $ nitrogen
      8016    0.210748   $ oxygen
      18000   0.004671   $ argon
c     * WATER *
```

```
M11   1001    0.666657
      8016    0.333343
MT11  lwtr.60t          $ 294K/ENDF7
c     * ALUMINUM 6061 *
M12   12000   0.011162
      13027   0.977325
      14000   0.005796
      22000   0.000499
      24000   0.001017
      25055   0.000435
      26000   0.001987
      29000   0.001174
      30000   0.000606
MT12  al27.12t           $ 294 K/ENDF7
c     * STAINLESS STEEL 304 *
M13   6000    0.001830
      14000   0.009781
      15031   0.000408
      16000   0.000257
      24000   0.200762
      25055   0.010001
      26000   0.690375
      28000   0.086587
c     * GRAPHITE *
M14   6000    0.999999
      5010    0.0000002   $ Boron impurities
      5011    0.0000008
MT14  grph.60t          $ 294K/ENDF7
c     * URANIUM ZIRCHYDRIDE  - FUEL *
M15  40000   -0.8991050
     1001    -0.0158948
     92235   -0.0165750
     92238   -0.0684250
MT15 zr/h.62t
     h/zr.62t
c     * BORON CARBIDE *
M16  6000     0.200019
     5010     0.159996
     5011     0.639985
c     * MOLYBDENUM *
M17  42000    1.000000
c     * ZIRCONIUM *
M18  40000    1.000000
c     * CONCRETE *
c  * Basalt Magnetite Concrete with rebar     den=4.04g/cc *
M19  1001        -0.00663900
     1002        -0.00000100
     11023.60c   -0.00848000
     12000       -0.01760000
     13027       -0.03380000
     14000       -0.10564201
     15031       -0.00163200
     16000       -0.00077420
     19000.60c   -0.00232000
     20000.60c   -0.07104001
     22000       -0.00480000
     24050.60c   -0.00000610
     24052.60c   -0.00011750
     24053.60c   -0.00001330
```

```
     24054.60c   -0.00000330
     25055       -0.00340460
     26000       -0.40312284
     28058.60c   -0.00027360
     28060.60c   -0.00010460
     28061.60c   -0.00000450
     28062.60c   -0.00001440
     28064.60c   -0.00000360
     29063.60c   -0.00026340
     29065.60c   -0.00011740
     42000       -0.00098180
     6000        -0.00044080
     8016        -0.33826467
     8017        -0.00013536
c     * LEAD *
M20  82000    1.000000
c
c     * ARGON 36 *
M21  18036    1.000000
c
c     * COBALT WIRE *
M22  13027   -0.00116
     27059   -0.99884
c
c     * CADMIUM *
M23  48000    1.000000
c
c    ** Transformations **
c     * Fuel Pin Universe *
c  * FE - B1 is the basis, needs no transformation *
c TR302    0.00000  0.00000 0
TR303    3.76936  -2.17678 0   $ FE - B2
TR304    3.76936  -6.53034 0   $ FE - B3
TR305    0        -8.70712 0   $ FE - B4
TR306   -3.76936  -6.53034 0   $ FE - B5
TR307   -3.76936  -2.17678 0   $ FE - B6
c  * Transient Rod - C1 (TR UNIVERSE BUILT IN C1, NO X/Y TR NEEDED) *
TR308    0.00000   0.00000 16.1
TR309    3.76936   2.17678 0   $ FE - C2
TR310    7.54126   0.00000 0   $ FE - C3
TR311    7.54126  -4.35356 0   $ FE - C4
TR312    7.54126  -8.70712 0   $ FE - C5
TR313    3.76936 -10.88390 0   $ FE - C6
c  * Reg. Rod - C7 (CR UNIVERSE BUILT IN C7, NO X/Y TR NEEDED) *
TR314    0.00000   0.00000 16.1
TR315   -3.76936 -10.88390 0   $ FE - C8
TR316   -7.54126  -8.70712 0   $ FE - C9
TR317   -7.54126  -4.35356 0   $ FE - C10
TR318   -7.54126   0.00000 0   $ FE - C11
TR319   -3.76936   2.17678 0   $ FE - C12
TR320    0.00000   8.70714 0   $ FE - D1
TR321    3.76936   6.53034 0   $ FE - D2
TR322    7.54126   4.35356 0   $ FE - D3
TR323   11.3106    2.17678 0   $ FE - D4
TR324   11.3106   -2.17678 0   $ FE - D5
TR325   11.3106    6.53034 16.1   $ Shim 1 - D6 (Trans. relative to C7)
TR326   11.3016  -10.88390 0   $ FE - D7
TR327    7.54126 -13.06068 0   $ FE - D8
```

```
TR328    3.76936 -15.23746 0   $ FE - D9
TR329    0.00000 -17.41426 0   $ FE - D10
TR330   -3.76936 -15.23746 0   $ FE - D11
TR331   -7.54126 -13.06068 0   $ FE - D12
TR332  -11.3016  -10.88390 0   $ FE - D13
TR333  -11.3106    6.53034 16.1   $ Shim 2 - D14 (Trans. relative to C7)
TR334  -11.3106   -2.17678 0   $ FE - D15
TR335  -11.3106    2.17678 0   $ FE - D16
TR336   -7.54126   4.35356 0   $ FE - D17
TR337   -3.76936   6.53034 0   $ FE - D18
TR338    0.00000  13.06064 0   $ FE - E1
TR339    3.76936  10.88394 0   $ FE - E2
TR340    7.54126   8.70714 0   $ FE - E3
TR341   11.31060   6.53034 0   $ FE - E4
TR342   15.08250   4.35356 0   $ FE - E5
TR343   15.08250   0.00000 0   $ FE - E6
TR344   15.08250  -4.35356 0   $ FE - E7
TR345   15.08250  -8.70712 0   $ FE - E8
TR346   15.08250 -13.06068 0   $ FE - E9
TR347   11.31060 -15.23746 0   $ FE - E10
c TR348    7.54126 -17.41426 0   $ FE - E11 (ccomment out for 3L)
TR349    3.76936 -19.59106 0   $ FE - E12
TR350    0.00000 -21.76776 0   $ FE - E13
TR351   -3.76936 -19.59106 0   $ FE - E14
TR352   -7.54126 -17.41426 0   $ FE - E15
TR353  -11.31060 -15.23746 0   $ FE - E16
TR354  -15.08250 -13.06068 0   $ FE - E17
TR355  -15.08250  -8.70712 0   $ FE - E18
TR356  -15.08250  -4.35356 0   $ FE - E19
TR357  -15.08250   0.00000 0   $ FE - E20
TR358  -15.08250   4.35356 0   $ FE - E21
TR359  -11.31060   6.53034 0   $ FE - E22
TR360   -7.54126   8.70714 0   $ FE - E23
TR361   -3.76936  10.88394 0   $ FE - E24
TR362    0.00000  17.41424 0   $ FE - F1
TR363    3.76936  15.23744 0   $ FE - F2
TR364    7.54126  13.06064 0   $ FE - F3
TR365   11.3106   10.88394 0   $ FE - F4
TR366   15.0825    8.70714 0   $ FE - F5
TR367   18.8519    6.53034 0   $ FE - F6
TR368   18.8519    2.17678 0   $ FE - F7
TR369   18.8519   -2.17678 0   $ FE - F8
TR370   18.8519   -6.53034 0   $ FE - F9
TR371   18.8519  -10.88390 0   $ FE - F10
TR372   18.8519  -15.23746 0   $ FE - F11
TR373   15.0825  -17.41424 0   $ FE - F12
c TR374   11.3106  -19.59106 0   $ FE - F13 (comment out for 3L)
c TR375    7.54126 -21.76776 0   $ FE - F14 (comment out for 3L)
TR376    3.76936 -23.94456 0   $ FE - F15
TR377    0.00000 -26.12136 0   $ FE - F16
TR378   -3.76936 -23.94456 0   $ FE - F17
TR379   -7.54126 -21.76776 0   $ FE - F18
TR380  -11.3106  -19.59106 0   $ FE - F19
TR381  -15.0825  -17.41426 0   $ FE - F20
TR382  -18.8519  -15.23746 0   $ FE - F21
TR383  -18.8519  -10.88390 0   $ FE - F22
TR384  -18.8519   -6.53034 0   $ FE - F23
```

```
TR385  -18.8519   -2.17678 0   $ FE - F24
TR386  -18.8519    2.17678 0   $ FE - F25
TR387  -18.8519    6.53034 0   $ FE - F26
TR388  -15.0825    8.70714 0   $ FE - F27
TR389  -11.3106   10.88394 0   $ FE - F28
TR390   -7.54126  13.06064 0   $ FE - F29
TR391   -3.76936  15.23744 0   $ FE - F30
TR393    3.76936  19.59104 0   $ FE - G2
TR394    7.54126  17.41424 0   $ FE - G3
TR395   11.3106   15.23744 0   $ FE - G4
TR396   15.0825   13.06064 0   $ FE - G5
TR397   18.8519   10.88394 0   $ FE - G6
TR399   22.6212    4.35356 0   $ FE - G8
TR400   22.6212    0.00000 0   $ FE - G9
TR401   22.6212   -4.35356 0   $ FE - G10
TR402   22.6212   -8.70712 0   $ FE - G11
TR403   22.6212  -13.06064 0   $ FE - G12
TR405   18.8519  -19.59106 0   $ FE - G14
TR406   15.0825  -21.76776 0   $ FE - G15
TR407   11.3106  -23.94456 0   $ FE - G16
TR408    7.54126 -26.12136 0   $ FE - G17
TR409    3.76936 -28.29816 0   $ FE - G18
TR411   -3.76936 -28.29816 0   $ FE - G20
TR412   -7.54126 -26.12136 0   $ FE - G21
TR413  -11.3106  -23.94456 0   $ FE - G22
TR414  -15.0825  -21.76776 0   $ FE - G23
TR415  -18.8519  -19.59106 0   $ FE - G24
TR417  -22.6212  -13.06068 0   $ FE - G26
TR418  -22.6212   -8.70712 0   $ FE - G27
TR419  -22.6212   -4.35356 0   $ FE - G28
TR420  -22.6212    0.00000 0   $ FE - G29
TR421  -22.6212    4.35356 0   $ FE - G30
c TR423  -18.8519   10.88394 0   $ Source - G32
TR424  -15.0825   13.06064 0   $ FE - G33
c TR425  -11.3106   15.23744 0   $ PNT - G34
TR426   -7.54126  17.41424 0   $ FE - G35
TR427   -3.76936  19.59104 0   $ FE - G36
c
c     * Beam Port 2 and 4 Alignment *
c  * Translate BP4/surface 320 down to BP plane *
c  * Rotate to perp. with long side of inner shroud *
*TR620   0  0 -6.985
         59.8665 -30.1335  90
         149.8665 59.8665  90
         90       90       0
c  * Translate BP4/surface 320 down to BP plane *
c  * Rotate to perp. with long side of inner shroud *
*TR621   0  0 -6.985
         59.8665 -30.1335  90
         149.8665 59.8665  90
         90       90       0
c  * Translate BP4/surface 320 down to BP plane *
*TR622   -80 -138.564 -6.985
c  * Translate BP4/surface 320 down to BP plane *
c  * Rotate to perp. with long side of inner shroud *
*TR623   0  0 -6.985
         59.8665 -30.1335  90
         149.8665 59.8665  90
```

```
         90       90       0
c  * Translate BP4/surface 320 down to BP plane *
c  * Rotate to perp. with long side of inner shroud *
*TR624   0  0 -6.985
         59.8665 -30.1335  90
         149.8665 59.8665  90
         90       90       0
c  * Translate BP2/surface 330 down to BP plane *
c  * Rotate to perp. with long side of inner shroud *
*TR630    0    39.5947 -6.985
         -30 -120  90
         60  -30   90
         90   90   0
c  * Translate BP2/surface 330 down to BP plane *
c  * Rotate to perp. with long side of inner shroud *
*TR631   0    39.5947 -6.985
         -30 -120  90
         60  -30   90
         90   90   0
c  * Translate BP2 end cutoff plane *
c  * Rotate to perp. with BP2 *
*TR632   8    39.5947 -6.985
         -30 -120  90
         60  -30   90
         90   90   0
c  * Translate BP2 stage divider plane *
c  * Rotate to perp. with BP2 *
*TR633  -130.564 119.5947 -6.985
         -30 -120  90
         60  -30   90
         90   90   0
c  * Translate BP2/surface 330 down to BP plane *
c  * Rotate to perp. with long side of inner shroud *
*TR634   0    39.5947 -6.985
         -30 -120  90
         60  -30   90
         90   90   0
c  * Translate BP2/surface 330 down to BP plane *
c  * Rotate to perp. with long side of inner shroud *
*TR635   0    39.5947 -6.985
         -30 -120  90
         60  -30   90
         90   90   0
```

B | Data Processing

This appendix provides the source code for the Python routines used to produce the computational results presented in this report. Brief descriptions of the purpose and functionality of each file is followed by the source code. Some reformatting has been done for readability. Superfluous comments in the original files have been removed. All codes were executed in Python 2.7.3 on a 2.53 GHz dual-core Apple MacBook with 4GB RAM. Runtime was typically less than 10 seconds, depending on the time resolution of the output data. Example input files, such as the isotope list `isolist.txt` and isotope table `isotable.txt`, are provided after the source code. For reference, implementation of some features of the code are described here.

Changing the flux: The `rxr_calc` routine imports a text file named `flux.txt` from the data library. Flux profiles can be investigated as needed by changing the `flux.txt` file. The energy bin structure of the input flux is inflexible.

Including/excluding isotopes from the system: The `isolist.txt` input file in the data library contains a list of isotopes (and associated data for other routines) in the system. The code will account for isotopes listed in `isolist.txt`. Commenting out (with the # character) or deleting an isotope altogether will exclude that isotope from the system.

Including/excluding specific reactions from the system: For each isotope in the system, `dep_mtx.build_XS()` scans the directory of NJOY-processed cross-sections and will account for each of those reactions in the depletion calculations. Adding an NJOY-processed cross-section file to the directory will include that re-

action in the calculation. Removing the cross-section file from the directory will exclude the reaction from the depletion calculation.

Changing the weighting for multigroup cross-section calculations: The default weighting regime set by the NJOY template file `template.txt` is a generalized water moderated reactor flux profile. NJOY has a number of other built-in weighting regimes, and also allows for a user-defined weights for the multigroup calculation. The weight regime is controlled by the fourth entry on the second card of the GROUPR section in the NJOY input file. Setting this parameter (in the NJOY99 manual as `IWT`) to 1 will point NJOY to the user-defined weights in CARD 8A. More information on the format of the card can be found in the description of GROUPR in the NJOY99 manual.

Changing the cross-section data set used for reactions: For the specified isotope, the NJOY processing routine will read in the the associated ENDF-formatted cross-section library from the ENDF folder in the data library and write the processed file to the output directory. Replacing the cross-section file for a given isotope with one from the desired data set and rerunning `njoy.input_run` for the isotope and reaction will run the next calculation with those cross sections.

data_read.py

The `data_read` routines defines a number of subroutines that are commonly called in the other files. `data_read.index()` reads the `isolist.txt` file to build a Python dictionary where the keys are indices and the values are isotope identifiers (such as 'Ar37'). `data_read.inv_index()` builds the opposite library where isotope identifiers are the keys and the indices are the values. This allows for searching of the index associated with an isotope and vice versa for the depletion matrix con-

struction routines. `data_read.decay_data()` opens the `isolist.txt` file to build a dictionary of isotope/decay constant pairs. `data_read.init_conc()` opens the `isolist.txt` file to build a dictionary of isotope/initial concentration pairs.

```
#!/user/bin/python

import math
import numpy
import os

# Reads in list of isotopes, assigns index value
def index():
    comment_char = '#'
    file_var = open('../datalib/isolist.txt', 'r')

    name_lib = {}

    i = 0
    for line in file_var:
        if comment_char in line[0]:
            continue
        else:
            line = line.split()
            name_libtemp = {
                i: line[0]+line[1]
                }
            i = i + 1
            name_lib.update(name_libtemp)

    file_var.close()

    return(name_lib)

# Reverses keys and values from index so dictionary is
#  searchable by isotope
def inv_index():
    comment_char = '#'
    file_var = open('../datalib/isolist.txt', 'r')

    name_lib = {}

    i = 0
    for line in file_var:
        if comment_char in line[0]:
            continue
        else:
            line = line.split()
            name_libtemp = {
                line[0]+line[1]: i
                }
            i = i + 1
            name_lib.update(name_libtemp)

    file_var.close()
```

```
    return(name_lib)

# Reads in lambda values from isotope list
def decay_data():
    comment_char = '#'

    # Open and read file
    lib_filename = r'../datalib/isolist.txt'
    file_var = open(lib_filename, 'r')

    # Initialize the dictionary
    decay_lib = {}

    # Ignore commented lines. Map values in file lines to dictionary
    #  keys. Read in lambda
    for line in file_var:
        if comment_char in line[0]:
            continue
        else:
            line = line.split()
            decay_libtemp = {
                line[0]+line[1]: float(line[4])
                }
            decay_lib.update(decay_libtemp)

    return(decay_lib)

    # Close the file
    file_var.close()

# Reads initial concentration data from isotope list
def init_conc():
    comment_char = '#'
    file_var = open('../datalib/isolist.txt', 'r')

    name_lib = index()
    IC_lib = {}

    # Read initial conc. values from isolist.txt
    for line in file_var:
        if comment_char in line[0]:
            continue
        else:
            line = line.split()
            IC_libtemp = {
                line[0]+line[1]: float(line[5])
                }
            IC_lib.update(IC_libtemp)

    isosize = len(IC_lib)

    file_var.close()

    # Initialize the matrix
    IC = numpy.zeros(shape=(isosize,1))

    # Define the decay terms on the diagonal
    for i in range(isosize):
```

```
        IC[i] = IC_lib[name_lib[i]]    # Populate IC values

    return(IC)
```

dep_mtx.py

The dep_mtx routine is responsible for construction of the coefficient matrix $[C]$ for the system of buildup and decay equations. The contents of $[C]$ are detailed in Section 3.1.1. The decay terms are retrieved from a user-created input file and assigned to the appropriate matrix elements for loss of parent species and buildup of daughter species in the `build_decay()` routine. The `build_XS()` routine determines the appropriate matrix element for the neutron interactions (radiative capture, alpha production, neutron production, etc) then calls `rxr_calc.calc()` to retrieve the value for the element. The `build()` routine retrieves the matrix populated by decay terms from `build_decay()` and the matrix populated by neutron interaction terms from `build_XS`, then submits the complete depletion matrix to the `eig_solve` routine.

```
#!/user/bin/python
#
# Dependencies
import numpy
import data_read
import math
import os
import njoy
import rxr_calc

# Wrapper for all other depletion matrix construction routines
def build():

    diag_mat = build_decay()
    offdiag_mat = build_XS()

    matrix = diag_mat + offdiag_mat

    # Write coefficient matrix to text file for diagnostics
    out_name = '/Users/agfay/Documents/UT/PhD/code/python/matrix.txt'
    numpy.savetxt(out_name, matrix, fmt='%1.7e')
```

```
    return(matrix)

# Builds decay information into diagonal terms
def build_decay():

    # Recall isotope list, decay constants, and decay modes
    isolist = data_read.index()
    decay_data = data_read.decay_data()
    mode_lib = data_read.decay_mode()
    inv_name_lib = data_read.inv_index()

    # Open isotable, read into actual table
    table_dir = '/Users/agfay/Documents/UT/PhD/code/datalib/isotable.txt'
    isotable = numpy.loadtxt(table_dir, dtype=numpy.str)

    # Calculate number of isotopes to be treated
    num_iso = len(isolist)

    # Initialize decay matrix
    matrix = numpy.zeros(shape=(num_iso,num_iso))


    # Iterate through by index value
    for i in range(num_iso):
        isoname = isolist[i]

        # Pull decay mode from mode_lib
        dec_mode = mode_lib[isoname]
        dec_cons = decay_data[isoname]

        # If it's a stable specie, write 0.0 to on-diagonal and be done
        if dec_mode == 'stable':
            matrix[i][i] -= dec_cons      # On-diagonal, loss by decay
            if dec_cons != 0:
                print 'error stable isotope lamda != 0'

        # If it's a branching decay, do some crazy shit
        elif dec_mode == 'branch':        # Branching decays
            # Read in branching modes and ratios
            branch_lib = data_read.branch(isoname)

            # For each mode, contribute the fractional part of lambda
            #  value to the on-diagonals and appropriate off-diagonals
            for k in range(len(branch_lib)):

                dec_mode = branch_lib[k][0]
                dec_ratio = float(branch_lib[k][1])

                # Get table displacement values for decay mode of interest
                decay_var = open('../datalib/rx_list.txt', 'r')
                comment_char = '#'
                for line in decay_var:
                    if comment_char in line[0]:
                        continue
                    else:
                        line = line.split()
                        if dec_mode in line[0]:
```

```
                    del_row = int(line[1])
                    del_col = int(line[2])
                    #print isoname, dec_mode, dec_cons
            decay_var.close()

            # Find table index of parent isotope
            tar_row, tar_col = numpy.where(isotable==isoname)
            tar_row = int(tar_row)
            tar_col = int(tar_col)

            # Find table index and name of daughter isotope
            #  using del_row and del_col
            prod_row = tar_row + del_row
            prod_col = tar_col + del_col
            prod_name = isotable[prod_row][prod_col]

            # Find name_lib index of daughter isotope
            #  using inv_name_lib. If daughter is not
            #  tracked, only write -lambda to on-diagonal
            #  If daughter is tracked, write +lambda to
            #  off-diagonal element for daughter and
            #  -lambda to on-diagonal elements.
            if prod_name not in inv_name_lib:
                #print 'Daughter isotope not tracked in
                                        depletion calculation.'
                matrix[i][i] -= dec_cons*dec_ratio
            else:
                prod_index = inv_name_lib[prod_name]
                if i == prod_index:
                    print 'Indexing error.'
                    return (0)
                matrix[prod_index][i] += dec_cons*dec_ratio
                matrix[i][i] -= dec_cons*dec_ratio

    # If it's a standard single-mode decay,
    #  assign the on- and off- diagonals
    else:
        # Get table displacement values for decay mode of interest
        decay_var = open('../datalib/rx_list.txt', 'r')
        comment_char = '#'
        for line in decay_var:
            if comment_char in line[0]:
                continue
            else:
                line = line.split()
                if dec_mode in line[0]:
                    del_row = int(line[1])
                    del_col = int(line[2])
                    #print isoname, dec_mode, dec_cons
        decay_var.close()

        # Find table index of parent isotope
        tar_row, tar_col = numpy.where(isotable==isoname)
        tar_row = int(tar_row)
        tar_col = int(tar_col)

        # Find table index and name of daughter
        #  isotope using del_row and del_col
        prod_row = tar_row + del_row
```

```
            prod_col = tar_col + del_col
            prod_name = isotable[prod_row][prod_col]

            # Find name_lib index of daughter isotope using inv_name_lib
            #  If daughter is not tracked, only write -lambda to
            #  on-diagonal. If daughter is tracked, write +lambda
            #  to off-diagonal element for daughter and -lambda
            #  to on-diagonal elements.
            if prod_name not in inv_name_lib:
                matrix[i][i] -= dec_cons      # On-diagonal, loss by decay
            else:
                prod_index = inv_name_lib[prod_name]
                if i == prod_index:
                    print 'Indexing error.'
                    return (0)
                matrix[prod_index][i] += dec_cons   # Daughter buildup
                matrix[i][i] -= dec_cons                    # Parent loss
                #print 'lambda assigned to element ', prod_index, ',', i

    # Matrix as output
    return(matrix);

# Builds XS info into off-diagonal terms and absorption into on-diagonal
def build_XS():

    # Get isotope list and index values
    name_lib = data_read.index()
    inv_name_lib = data_read.inv_index()
    num_iso = len(name_lib)

    # Initialize matrix
    matrix = numpy.zeros(shape=(num_iso,num_iso))

    # Loop over list of isotopes
    for i in range(len(name_lib)):

        isoindex = i
        isoname = name_lib[isoindex]

        # Find all NJOY-processed XS files for the isotope of interest
        #  Grab the MT number from the end of the filename, pass that
        #  as the reaction number
        XSdir = '/Users/agfay/Documents/UT/PhD/code/
                                njoy99/wrkdir/processed'
        njoy_list = os.listdir(XSdir)
        #print isoname
        for file in njoy_list:
            if isoname in file:
                filename = file
                rxn_num = filename.split('_')[2]
                #print 'Processing MT', rxn_num, 'for ' + isoname + '...'

                # Reference rx_list to get table displacement
                rx_var = open('../datalib/rx_list.txt', 'r')
                comment_char = '#'
                for line in rx_var:
                    if comment_char in line[0]:
                        continue
                    else:
```

```
                        line = line.split()
                        if rxn_num in line[0]:
                            del_row = int(line[1])
                            del_col = int(line[2])
                rx_var.close()

                # Open isotable, read into actual table
                table_dir = '/Users/agfay/Documents/UT/
                                        PhD/code/datalib/isotable.txt'
                isotable = numpy.loadtxt(table_dir, dtype=numpy.str)

                # Find table index of target isotope
                tar_row, tar_col = numpy.where(isotable==isoname)
                tar_row = int(tar_row)
                tar_col = int(tar_col)

                # Find table index and name of product isotope
                #  using del_row and del_col
                prod_row = tar_row + del_row
                prod_col = tar_col + del_col
                prod_name = isotable[prod_row][prod_col]

                # Find name_lib index of product isotope using
                #  inv_name_lib. If product is not tracked, only
                #  assign S-value for on-diagonal. If product is
                #  tracked, assign off-diagonal and on-diagonal
                #  elements.
                if prod_name not in inv_name_lib:
                    S_value = rxr_calc.calc(isoname, rxn_num)
                    matrix[isoindex][isoindex] -= S_value
                else:
                    prod_index = inv_name_lib[prod_name]
                    if isoindex == prod_index:
                        print 'Indexing error.'
                        return (0)
                    S_value = rxr_calc.calc(isoname, rxn_num)
                    matrix[prod_index][isoindex] = S_value
                    matrix[isoindex][isoindex] -= S_value

    return(matrix)
```

rxr_calc.py

The `rxr_calc` routine is written to calculate the total group constant that is written to each element of the depletion matrix. It is called by the `dep_mtx` routine for each reaction in each tracked isotope for which cross-section data exists in the data library. The `rxr_calc` routine calculates the group constant for each

energy bin of the NJOY99-processed cross-section files by multiplying the cross-section against the MCNPX-calculated group flux and normalizing by the lethargy of the cross-sections bins. The total group constant is returned to the `dep_mtx` routine for assignment to the appropriate matrix element.

```
#!/user/bin/python

import numpy
import data_read
import math
import os
import njoy

def calc(isoname, rxn):

    # Define some things
    comment_char = '#'
    fluxdir = '/Users/agfay/Documents/UT/PhD/code/datalib/'
    XSdir = '/Users/agfay/Documents/UT/PhD/code/njoy99/wrkdir/processed/'

    # Read in flux, write to numpy array
    fluxname = fluxdir + 'flux.txt'
    flux_var = open(fluxname, 'r')
    flux_array = numpy.loadtxt(fluxname)

    # Read in XS data
    XSname = XSdir + 'proc_' + isoname + '_' + rxn
    XS_array = numpy.loadtxt(XSname)

    # Convert to XS energies to MeV, XSs to barns
    XS_array[:,0] *= 1e-6
    XS_array[:,1] *= 1e-6
    XS_array[:,2] *= 1e-24

    #print 'Calculating rate for MT' + rxn + ' in ' + isoname + '...'

    # Add up differential contributions to RXR
    # Algorithmically this relies on a specific energy group structure
    #  for both the flux and cross-section, not portable to other
    #  group structures.
    k = 0
    z = 0
    diff_RR = []
    for i in range(len(flux_array)):
        if i == 0:
            Ebin_size = flux_array[i,0] - XS_array[i,0]
        else:
            Ebin_size = flux_array[i,0] - flux_array[i-1,0]
        for k in range(3):
            diff = XS_array[3*i+k,2]*flux_array[i,1]\
                    *(XS_array[3*i+k,1] - XS_array[3*i+k,0])/Ebin_size
            diff_RR.append(diff)

    diff_RR = numpy.asarray(diff_RR)
```

```
    #print 'Done...'

    #print diff_RR
    #print sum(diff_RR)
    return(sum(diff_RR))
```

eigd_solve.py

The `eigd_solve` routine executes the solution of the eigenvalue decomposition of the depletion matrix $[C]$. For a given time step, the routine returns the concentration vector of tracked isotopes. The concentration can either be printed directly to the terminal for single time intervals, or returned to a wrapping routine to iterate over time steps.

```
#!/user/bin/python

import numpy.linalg
import dep_mtx
import math
import data_read

def solve(t):
    # Build the depletion matrix and decompose into eigenvalues and
    #  eigenvectors
    dep_matrix = dep_mtx.build()
    L, V = numpy.linalg.eig(dep_matrix)

    # Inverse of eigenvector matrix
    Vi = numpy.linalg.inv(V)

    # Initialize eigenvalue step matrix, build it
    Le = numpy.zeros(shape=(len(L),len(L)))
    for i in range(len(L)):
        Le[i,i] = math.exp(float(t*L[i]))

    # Import the initial concentration vector
    IC = data_read.init_conc()

    # Solve for the time step. In numpy, the * operator multiplies arrays
    #  element-wise, so the numpy.dot() function must be used.
    step1 = numpy.dot(V,Le)
    step2 = numpy.dot(step1,Vi)
    step3 = numpy.dot(step2,IC)

    conc_vec = step3
```

```
    out_name = '/Users/agfay/Documents/UT/PhD/code/python/outvec.txt'
    numpy.savetxt(out_name, conc_vec, fmt='%1.7e')
```

solver.py

The `solver` routine exists as a wrapper to `eigd_solve`. The total irradiation time is passed as an input parameter, and the time resolution of the concentration of tracked isotopes is defined in the routine. The routines writes to a file the concentration of each tracked isotope at each time step.

```
#!/user/bin/python

import numpy
import numpy.linalg
import dep_mtx
import math
import data_read
import eigd_solve

def output(t):

    step = t/100

    # Import list of readout isotopes
    name_lib = data_read.index()

    # Initialize arrays
    out_lib = numpy.zeros(shape=(1,len(name_lib)+1))
    conc_vec_time = numpy.zeros(shape=(1,len(name_lib)+1))

    # Iterate over eigd_solve to build matrix of concentrations
    for i in range(0,t+1,step):
        conc_vec = eigd_solve.solve(i)
        conc_vec_trans = numpy.reshape(conc_vec, (1,len(conc_vec)))
        conc_vec_time = numpy.insert(conc_vec_trans,0,i,axis=1)
        print 'Iterating on t=',i
        out_lib = numpy.append(out_lib, conc_vec_time, axis=0)

    # Format and write to output file as numpy array
    out_name = '/Users/agfay/Documents/UT/PhD/code/python/outfile.txt'
    numpy.savetxt(out_name, out_lib, fmt='%1.7e')

    # Create header line with isotope name library
    header_line = 'time [s]      '
    for i in range(len(name_lib)):
        header_line = header_line + name_lib[i] + '          '
    header_line = header_line + '\n'
```

```
    # Open output file, rewrite first line, rewrite file
    lines = open(out_name, 'r').readlines()
    lines[0] = header_line
    file = open(out_name, 'w')
    for line in lines:
        file.write(line)
    file.close()
```

activity.py

The `activity` routine is written to process the complete output file from `solver`, which is in the same dimensions as the initial concentrations defined in `isolist.txt` (number density), and return a matrix of the activity of the isotopes of interest. The routine relies on user-definition of the irradiation volume and isotopes of interest within the routine. The routine also includes options for plotting the output of the tracked isotopes.

```
#!/user/bin/python

import numpy as np
import matplotlib.pyplot as plt
from matplotlib.ticker import MaxNLocator
from matplotlib.ticker import FormatStrFormatter
from matplotlib import rc, rcParams
import data_read
import solver
import pylab

def test(t):

    # Manually set isotopes to output
    plot_list = ['Ar37', 'Ar39', 'Ar41']

    # Set volume for activity calculation
    volume = 1439.29

    # Run the solver
    solver.output(t)

    # Read solver output
    data = np.loadtxt('outfile.txt',skiprows=1)

    # Read index data and decay data
    inv_index = data_read.inv_index()
```

```
    decay_lib = data_read.decay_data()

    # Build time column of activity array, in hours
    act_array = np.zeros(shape=(len(data),1))
    for i in range(len(data)):
        act_array[i][0] = data[i][0]/3600

    # Get decay constant and index for isotope
    #  Assign number density*volume*lambda to temporary column
    #  and append column to array
    temp = np.zeros(shape=(len(data),1))
    for i in range(len(plot_list)):
        lamb = decay_lib[plot_list[i]]
        index = inv_index[plot_list[i]]

        for k in range(len(data)):
            temp[k,0] = volume*lamb*data[k,index+1]

        act_array = np.append(act_array,temp,axis=1)

    out_name = '/Users/agfay/Documents/UT/PhD/code/python/out_act.txt'
    np.savetxt(out_name, act_array, fmt='%1.11e')

    # Create header line with isotope name library
    header_line = 'time [s]          '
    for i in range(len(plot_list)):
        header_line = header_line + plot_list[i] + '             '
    header_line = header_line + '\n'

    # Open output file, rewrite first line, rewrite file
    lines = open(out_name, 'r').readlines()
    lines.append(header_line)
    file = open(out_name, 'w')
    for line in lines:
        file.write(line)
    file.close()

# Plot it up
#     plt.close('all')
#     plt.rc('text', usetex=True)
#     plt.rcParams['font.family'] = 'Charter BT'
#     plt.rcParams['axes.formatter.limits'] = [20, -20]
#     plt.rcParams['font.size'] = 12
#     fig = plt.figure(figsize=[5,6.5], dpi=120)
#
#    # ax4 = fig.add_subplot(414)
#    # ax4.plot(act_array[:,0], act_array[:,4], linewidth=1.5)
#    # ax4.xaxis.set_label_text('Time [h]')
#    # ax4.yaxis.set_major_locator(MaxNLocator(4))
#    # ax4.set_ylim(bottom=0)
#    # ax4.text(1, 0.025, r'$^{42}$Ar', fontsize=12)
#
#     ax3 = fig.add_subplot(313)
#     ax3.plot(act_array[:,0], act_array[:,3], linewidth=1.5)
#     ax3.xaxis.set_label_text('Time [h]')
#     #plt.setp(ax3.get_xticklabels(), visible=False)
#     ax3.yaxis.set_major_locator(MaxNLocator(4))
#     ax3.set_ylim(bottom=0)
```

```
#     ax3.text(1, 3.8e5, r'$^{41}$Ar', fontsize=12)
#
#     ax2 = fig.add_subplot(312, sharex=ax3)
#     ax2.plot(act_array[:,0], act_array[:,2], linewidth=1.5)
#     plt.setp(ax2.get_xticklabels(), visible=False)
#     ax2.yaxis.set_major_locator(MaxNLocator(4))
#     ax2.set_ylim(bottom=0)
#     ax2.yaxis.set_label_text('Activity [Bq]')
#     ax2.yaxis.labelpad = 5
#     ax2.text(1, 6e3, r'$^{39}$Ar', fontsize=12)
#
#     ax1 = fig.add_subplot(311, sharex=ax3)
#     ax1.plot(act_array[:,0], act_array[:,1], linewidth=1.5)
#     plt.setp(ax1.get_xticklabels(), visible=False)
#     ax1.yaxis.set_major_locator(MaxNLocator(4))
#     ax1.set_ylim(bottom=0)
#     ax1.text(1, 1.4e8, r'$^{37}$Ar', fontsize=12)
#
#
    #plt.savefig('../../Dissertation/TeX/Figures/figxx_xx.png', dpi=800)
```

njoy.py

The `njoy.input_run()` routine is run independently of the rest of the code used to solve the differential equations detailed in Section 3.1.1. For a specified isotope and reaction, `njoy.input_run()` retrieves the associated raw ENDF file, rewrites the template NJOY99 input file for the specific reaction, runs NJOY99, then parses the NJOY99 output as a simple text file for later use by `rxr_calc.calc()`.

```
#!/user/bin/python

import numpy
import math
import os
import fileinput
import subprocess
import re

def input_run(isotope, rxn):
    comment_char = '#'

    # Determine full path of relevant ENDF file
    XSdir = '/Users/agfay/Documents/UT/PhD/code/datalib/ENDF/'
    NJOYdir = '/Users/agfay/Documents/UT/PhD/code/njoy99/wrkdir/'
    ENDF_list = os.listdir(XSdir)
    for file in ENDF_list:
        if isotope in file:
```

```
        filename = file

# Copy ENDF file into temp20
fullname = XSdir + filename
cmd = 'cp ' + fullname + ' ' + NJOYdir + 'tape20'
subprocess.call(cmd, shell=True)

print '  ENDF file for ' + isotope +
   ' copied to tape20 in /njoy99/wrkdir'

# Read isolist to get material number.
file_var = open('../datalib/isolist.txt', 'r')

MATN_lib = {}

# Write material number dictionary
for line in file_var:
    if comment_char in line[0]:
        continue
    else:
        line = line.split()
        MATN_libtemp = {
            line[0]+line[1]: line[2]
            }
        MATN_lib.update(MATN_libtemp)

file_var.close()

# Assign MATN
MATN = MATN_lib[isotope]
print '  ENDF material number for ' + isotope + ': ' + MATN

# Read in NJOY input file template. Open input file to write.
file_varR = open('../njoy99/wrkdir/template.txt', 'r')
file_varW = open('../njoy99/wrkdir/inputPY.txt', 'w')


print '  Writing NJOY99 input deck for ' + isotope + ' MT ' + rxn
# Read each line. Replace MATN or MT placeholder
#  with actual material/rxn number.
for line in file_varR:
    lineS = line.split()
    if 'MATN' in lineS[0]:
        line = line.replace('MATN', MATN)
        file_varW.write(line)
    elif 'MT' in line:
        line = line.replace('MT', rxn)
        file_varW.write(line)
    else:
        file_varW.write(line)

# Add a blank line because NJOY99 is cool
file_varW.write('\n')

# Close 'em up
file_varR.close()
file_varW.close()
```

```
print '  Executing NJOY99...'
# Move to NJOY dir, run NJOY, clean the dir, return to python dir
path = '../njoy99/wrkdir'
os.chdir(path)
cmd = '../xnjoy<inputPY.txt'
subprocess.call(cmd, shell=True)
cmd = 'rm tape21 tape22 tape23 tape24 tape25'
subprocess.call(cmd, shell=True)
cmd = 'cp output ./raw_output/raw_' + isotope + '_' + rxn
subprocess.call(cmd, shell=True)
path = '../../python'
os.chdir(path)

print '  NJOY99 groupr output written to /njoy99/wrkdir/raw_output/'
print '  Parsing NJOY99 output file ' + isotope + '_' + rxn + '...'

# Open output file for parsing
out_filename = NJOYdir + 'raw_output/raw_' + isotope + '_' + rxn
file_var0 = open(out_filename, 'r')

# Initialize target lists for data extraction
energy_list = []
XS_list = []

# Extract neutron groups and cross-sections
for line in file_var0:
    if 'epri-cpm' in line:
        for i in range(69):
            row = file_var0.next()
            temp = row.split()
            energy_list.append([temp[1], temp[3]])
file_var0.seek(0)
for line in file_var0:
    if 'infinite dilution' in line:
        file_var0.next()
        for k in range(69):
            row = file_var0.next()
            temp = row.split()
            temp[1] = re.sub(r'-', r'E-',temp[1])
            temp[1] = re.sub('\+', r'E+',temp[1])
            XS_list.append([temp[1]])

# Tag the XS_list as third column, write to new list
out_array = []
for m in range(len(energy_list)):
    out_array.append([energy_list[m][0],
       energy_list[m][1], XS_list[m][0]])

# Convert to numpy array, write to file
out_array = numpy.asarray(out_array)
out_array = out_array.astype(numpy.float)
proc_filename = NJOYdir + 'processed/proc_' + isotope + '_' + rxn
numpy.savetxt(proc_filename, out_array, fmt='%1.5e')

print '  NJOY99 groupr output processed to /njoy99/wrkdir/processed/'

file_var0.close()
return()
```

```
    #return(MATN_lib)
```

NJOY99 Input File Template

This is the template for the NJOY99 input file used to calculate group cross-sections necessary for solving the buildup and decay equations described in Section 3.1.1. The `moder` module converts the ASCII-formatted ENDF file to a binary package that decreases NJOY99 processing time. The `reconr` module reconstructs pointwise cross-section data for resonances using the appropriate interpolation methods, then the `broadr` module applies temperature-dependent Doppler broadening to resonances. The `groupr` module calculates the multigroup cross-sections according to the user-specified flux profile and energy regime. The final call to `moder` converts the binary package back to human-readable ASCII formatting.

The values `MATN` and `MT` are placeholders that the NJOY99 processing script replaces with the appropriate material number and reaction number depending on the cross-sections being collapsed.

The 69-group energy regime was used for EPRI-CPM calculations and is specifically tailored for high resolution in the energy regions of interest for water-moderated, thermal-reactor applications.

```
moder
20 -21
reconr
-21 -22
'pendf tape for isotope'/
MATN 1/
.005/
'isotope from endf'/
0/
broadr
```

```
20 -22 -23
MATN 1/
.005/
300
0/
groupr
-21 -23 0 -24
MATN 9 0 4 3 1 1 1
'groupr collapse'/
300.
1.e10
.1 0.025 0.8209e6 1.4e6
3 MT 'capture'/
0/
0/
moder
-24 25
stop
```

C | Research Reactor Utilization

This appendix includes a table of the research reactors used to estimate the global ^{37}Ar source term. Data was collected from the International Atomic Energy Agency Research Reactor Database [72]. Only reactors reported as operational as of November 2013 are listed. Categories describe the utilization of the reactor based on full-power operation days.

HIGH and MED utilization reactors with no reported utilization value in kWh·yr^{-1} were assigned on estimate based on the minimum full-power operation time defined for each category. Definitions of each category can be found in Section 6.3.

Country	Name	Type	Power [kW]	Utilization [kWh·yr^{-1}]	Category
Algeria	Es Salam	HEAVY WATER	1.50E+04	1.440E+06	LOW
Algeria	Nur	POOL	1.00E+03	2.400E+05	LOW
Argentina	RA-0	TANK	1.00E-02	0.000E+00	LOW
Argentina	RA-6	POOL	5.00E+02	8.064E+06	MED
Argentina	RA-3	POOL	1.00E+04	2.952E+07	HIGH
Argentina	RA-1	TANK	4.00E+01	3.226E+06	HIGH
Argentina	RA-4	HOMOG (S)	1.00E-03	0.000E+00	LOW
Australia	OPAL	POOL	2.00E+04	1.320E+08	HIGH
Austria	Atominstitut	TRIGA	2.50E+02	2.400E+05	MED
Bangladesh	Savar	TRIGA	3.00E+03	2.400E+06	MED
Belgium	BR-1	GRAPHITE	4.00E+03	8.400E+05	MED

Belgium	BR-2	TANK	1.00E+05	1.560E+08	MED
Brazil	IPR-R1	TRIGA	1.00E+02	2.400E+04	LOW
Brazil	ARGONAUTA	ARGONAUT	2.00E-01	3.226E+03	MED
Brazil	IPEN	POOL	1.00E-01	0.000E+00	LOW
Brazil	IEA-R1	POOL	5.00E+03	1.260E+07	MED
Canada	EP de Montreal	SLOWPOKE-2	2.00E+01	3.226E+05	MED
Canada	Royal Mil. Col.	SLOWPOKE-2	2.00E+01	3.226E+05	MED
Canada	U. of Alberta	SLOWPOKE-2	2.00E+01	0.000E+00	LOW
Canada	Saskatch. Res. Co.	SLOWPOKE-2	1.60E+01	9.600E+04	LOW
Canada	ZED-2	TANK	2.00E-01	0.000E+00	LOW
Canada	NRU	HEAVY WATER	1.35E+05	7.752E+08	HIGH
Canada	McMaster Univ.	POOL, MTR	3.00E+03	6.840E+06	HIGH
Chile	RECH-1	POOL	5.00E+03	6.000E+06	MED
China	SPR IAE	POOL	3.50E+03	8.160E+06	MED
China	CEFR	FAST BREEDER	6.50E+04	0.000E+00	LOW
China	CARR	TANK IN POOL	6.00E+04	0.000E+00	LOW
China	HTR-10	HIGH TEMP GAS	1.00E+04	0.000E+00	LOW
China	SPRR-300	POOL	3.00E+03	1.440E+05	LOW
China	ESR-901	POOL	1.00E+03	2.400E+05	LOW
China	HFETR	TANK	1.25E+05	7.913E+07	MED
China	MJTR	POOL	5.00E+03	1.080E+07	MED
China	NHR-5	HEATING PROT	5.00E+03	7.200E+05	MED
China	PPR PULSING	POOL, UZRH	1.00E+03	0.000E+00	LOW
China	IHNI-1	POOL	3.00E+01	0.000E+00	LOW
China	MNSR-SZ	MNSR	3.00E+01	0.000E+00	LOW
China	MNSR IAE	MNSR	2.70E+01	0.000E+00	LOW
Czech Rep.	VR-1	POOL	5.00E+00	8.064E+04	MED

Czech Rep.	LVR-15	TANK WWR	1.00E+04	4.452E+07	HIGH
Czech Rep.	LR-0	POOL	5.00E+00	8.064E+04	MED
North Korea	IRT-DPRK	POOL, IRT	8.00E+03	1.680E+06	LOW
Egypt	ETTR-2	POOL	2.20E+04	2.208E+07	MED
Finland	Espoo	TRIGA	2.50E+02	1.200E+05	MED
France	ORPHEE	POOL	1.40E+04	6.720E+07	HIGH
France	EOLE	TANK	1.00E-01	1.613E+03	MED
France	HFR	HEAVY WATER	5.83E+04	3.120E+08	HIGH
France	MINERVE	POOL	1.00E-01	1.613E+03	MED
France	OSIRIS	POOL	7.00E+04	3.600E+08	HIGH
France	ISIS	POOL	7.00E+02	1.680E+05	MED
France	CABRI	POOL	2.50E+04	0.000E+00	LOW
Germany	BER-II	POOL	1.00E+04	6.000E+07	HIGH
Germany	FRM II	POOL	2.00E+04	1.152E+08	HIGH
Germany	FRMZ	TRIGA	1.00E+02	9.600E+04	MED
Germany	AKR	HOMOG (S)	2.00E-03	3.226E+01	MED
Ghana	GHARR-1	MNSR	3.00E+01	4.838E+05	MED
Hungary	Budapest RR	TANK WWR	1.00E+04	3.480E+07	MED
Hungary	0	POOL	1.00E+02	0.000E+00	LOW
India	FBTR	FAST BREEDER	4.00E+04	3.226E+09	HIGH
India	DHRUVA	HEAVY WATER	1.00E+05	8.064E+09	HIGH
India	KAMINI	U-233 FUELLED	3.00E+01	6.000E+06	LOW
India	Crit.	TANK	1.00E-01	0.000E+00	LOW
Indonesia	KARTINI	TRIGA	1.00E+02	1.613E+06	MED
Indonesia	RSG-GAS	POOL, MTR	3.00E+04	5.184E+07	HIGH
Iran	TRR	POOL	5.00E+03	7.200E+06	MED
Iran	ENTC MNSR	MNSR	3.00E+01	0.000E+00	LOW

Israel	IRR-2	HEAVY WATER	2.60E+04	0.000E+00	LOW
Israel	IRR-1	POOL	5.00E+03	2.400E+06	LOW
Italy	RSV TAPIRO	FAST SOURCE	5.00E+00	0.000E+00	LOW
Italy	LENA	TRIGA	2.50E+02	9.600E+04	MED
Italy	RC-1	TRIGA	1.00E+03	3.360E+05	LOW
Italy	AGN 201	HOMOG (S)	2.00E-02	0.000E+00	LOW
Jamaica	UWI CNS	SLOWPOKE	2.00E+01	9.600E+04	MED
Japan	STACY	HOMOG	2.00E-01	0.000E+00	LOW
Japan	UTR KINKI	ARGONAUT	1.00E-03	1.613E+01	MED
Japan	JRR-4	POOL	3.50E+03	1.680E+06	MED
Japan	TRACY	PULSING	1.00E+01	0.000E+00	LOW
Kazakhstan	WWR-K	POOL	6.00E+03	3.360E+06	HIGH
Kazakhstan	EWG 1	TANK	3.50E+04	0.000E+00	LOW
South Korea	HANARO	POOL	3.00E+04	1.613E+08	HIGH
South Korea	AGN-201K	HOMOG (S)	1.00E-02	0.000E+00	LOW
Malaysia	PUSPATI	TRIGA	1.00E+03	6.720E+05	MED
Mexico		TRIGA	1.00E+03	6.000E+05	MED
Morocco	MA-R1	TRIGA	2.00E+03	3.600E+05	LOW
Netherlands	Delphi			0.000E+00	LOW
Netherlands	HOR	POOL	2.00E+03	7.680E+06	HIGH
Netherlands	LFR	ARGONAUT	3.00E+01	4.838E+05	MED
Nigeria	NIRR-0001	MNSR	3.00E+01	9.600E+04	LOW
Norway	JEEP II	TANK	2.00E+03	1.224E+07	HIGH
Norway	HBWR	HEAVY WATER	2.00E+04	9.600E+07	HIGH
Pakistan	PARR-1	POOL	1.00E+04	3.600E+06	LOW
Pakistan	PARR-2	MNSR	3.00E+01	7.200E+04	LOW
Peru	RP-10	POOL	1.00E+04	3.744E+06	MED

Poland	MARIA	POOL	3.00E+04	7.200E+07	HIGH
Portugal	RPI	POOL	1.00E+03	1.080E+06	HIGH
Romania	PITESTI	TRIGA DUAL	5.00E+02	4.032E+07	HIGH
Romania	PITESTI	TRIGA DUAL	1.40E+04	0.000E+00	LOW
Russia	IR-8	POOL, IRT	8.00E+03	2.040E+07	MED
Russia	IRT	POOL, IRT	2.50E+03	1.080E+07	HIGH
Russia	WWR-M	TANK WWR	1.80E+04	5.669E+07	HIGH
Russia	WWR-TS	TANK WWR	1.50E+04	1.255E+07	LOW
Russia	BOR-60	FAST BREEDER	6.00E+04	2.760E+08	HIGH
Russia	GAMMA	TANK	1.50E+02	3.600E+05	LOW
Russia	F-1	GRAPHITE PILE	2.40E+01	3.871E+05	MED
Russia	ARGUS	HOMOG (L)	2.00E+01	0.000E+00	LOW
Russia	GIDRA	HOMOG (L)	1.00E+01	0.000E+00	LOW
Russia	VK-50	BWR-PROTO	2.00E+05	1.248E+09	HIGH
Russia	SM-3	PRESSURE	1.00E+05	5.520E+08	HIGH
Russia	MIR-M1	POOL	1.00E+05	1.548E+08	HIGH
Russia	IVV-2M	POOL	1.50E+04	1.109E+08	HIGH
Russia	RBT-6	POOL	6.00E+03	4.608E+07	HIGH
Russia	RBT-10/2	POOL	7.00E+03	4.104E+07	HIGH
Russia	IRT-T	POOL, IRT	6.00E+03	2.100E+07	HIGH
Russia	IBR-2M	FAST, PULSED	2.00E+03	5.184E+06	HIGH
Russia	OR-M	TANK WWR	3.00E+02	1.200E+05	MED
Serbia	RB	HEAVY WATER	0.00E+00	0.000E+00	LOW
Slovenia	LJUBLJANA	TRIGA	2.50E+02	2.880E+05	MED
South Africa	SAFARI-1	TANK IN POOL	2.00E+04	1.454E+08	HIGH
Switzerland	AGN 211 P	HOMOG (S)	2.00E+00	0.000E+00	LOW
Syria	SRR-1	MNSR	3.00E+01	2.400E+04	LOW

Taiwan, China	THOR	TRIGA	2.00E+03	3.120E+07	MED
Thailand	TRR-1/M1	TRIGA	2.00E+03	1.200E+06	MED
Turkey	ITU-TRR	TRIGA	2.50E+02	0.000E+00	LOW
Ukraine	WWR-M	TANK WWR	1.00E+04	2.880E+06	MED
Ukraine	SNI, IR-100	POOL, IRT	2.00E+02	3.226E+06	MED
UK	NEPTUNE	POOL	1.00E-01	0.000E+00	LOW
USA	Idaho State U.	HOMOG (S)	5.00E-03	0.000E+00	LOW
USA	NBSR	HEAVY WATER	2.00E+04	1.200E+08	HIGH
USA	Wash. State U.	TRIGA	1.00E+03	8.160E+05	MED
USA	NTR GE	GRAPHITE	1.00E+02	7.200E+04	MED
USA	HFIR	TANK	8.50E+04	3.427E+08	HIGH
USA	ARRR	TRIGA	2.50E+02	7.200E+05	HIGH
USA	Oregon State U.	TRIGA	1.10E+03	9.600E+05	MED
USA	NRAD	TRIGA	2.50E+02	1.440E+05	MED
USA	U. of Florida	ARGONAUT	1.00E+02	2.400E+04	MED
USA	Texas A&M U.	HOMOG (S)	5.00E-03	0.000E+00	LOW
USA	Ohio St. U.	POOL	5.00E+02	1.680E+05	MED
USA	NC State U.	POOL, PULSTAR	1.00E+03	6.000E+06	MED
USA	U. of New Mexico	HOMOG (S)	5.00E-03	0.000E+00	LOW
USA	ATR	TANK	2.50E+05	2.016E+10	HIGH
USA	MURR	TANK IN POOL	1.00E+04	7.884E+07	HIGH
USA	Mass. Inst. Tech.	TANK	6.00E+03	2.880E+07	HIGH
USA	U. of Texas	TRIGA	1.10E+03	4.800E+06	MED
USA	Texas A&M U.	TRIGA	1.00E+03	2.160E+06	MED
USA	U. of Cal. Davis	TRIGA	2.00E+03	1.440E+06	MED
USA	U. of Mass. Lowell	POOL	1.00E+03	9.600E+05	MED
USA	Penn. State U.	TRIGA MARK	1.00E+03	7.680E+05	MED

USA	U of Wisconsin	TRIGA	1.00E+03	5.520E+05	MED
USA	U. of Missouri	POOL, MTR	2.00E+02	2.400E+05	MED
USA	ACRR	TRIGA	4.00E+03	9.600E+04	MED
USA	DOW Chemical	TRIGA	3.00E+02	4.800E+04	MED
USA	U of Maryland	TRIGA	2.50E+02	4.032E+06	MED
USA	Rhode Island NSC	POOL	2.00E+03	8.400E+05	LOW
USA	GSTR	TRIGA	1.00E+03	6.000E+05	LOW
USA	AFRRI	TRIGA	1.00E+03	4.800E+04	LOW
USA	Kansas State Univ.	TRIGA	2.50E+02	4.800E+04	LOW
USA	Reed College	TRIGA	2.50E+02	1.200E+06	LOW
USA	U. of Cal. Irvine	TRIGA	2.50E+02	4.800E+04	LOW
USA	U. of Utah	TRIGA	1.00E+02	2.400E+05	LOW
USA	ATRC	POOL	5.00E+00	0.000E+00	LOW
USA	Purdue U.	POOL	1.00E+00	0.000E+00	LOW
Uzbekistan	WWR-SM	TANK WWR	1.00E+04	1.067E+09	HIGH
Uzbekistan	IIN-3M	HOMOG PUL	2.00E+01	0.000E+00	LOW
Vietnam	DALAT	POOL	5.00E+02	6.000E+05	MED

References

[1] "Comprehensive Nuclear-Test-Ban Treaty." http://www.state.gov/t/avc/trty/16411.htm, 1996.

[2] "The Test Ban Treaty," *IAEA Bulletin*, no. 154, 1973.

[3] "Treaty Between The United States of America and The Union of Soviet Socialist Republics on the Limitation of Underground Nuclear Weapon Tests." http://www.state.gov/t/isn/5204.htm.

[4] "The final verification measure: CTBTO Preparatory Commission." http://www.ctbto.org/verification-regime/on-site-inspection/, 2013.

[5] B. Kennett and F. Ringdal, "Locating seismic events in the CTBT context," *Pure and Applied Geophysics*, vol. 158, pp. 7–18, Feb. 2001.

[6] M. Lawrence, "Acoustic Monitoring of the Global Ocean for the CTBT," in *Proc. of Acoustics*, pp. 455–460.

[7] D. Christie, B. Kennett, and C. Tarlowski, "Detection of regional and distant atmospheric explosions at IMS infrasound stations," in *27th Seismic Research Review: Ground-Based Nuclear Explosion Monitoring Technologies*, pp. 817–827, 2005.

[8] C. Smith, "Utilization of the Noble Gases in Studies of Underground Nuclear Detonations," in *Noble Gases* (R. E. Stanley and A. A. Moghissi, eds.), pp. 540–543, 1975.

[9] J. J. Zucca, C. Carrigan, P. Goldstein, S. P. Jarpe, J. Sweeney, W. L. Pickles, and B. Wright, "Signatures of Testing: On-Site Inspection Technologies," 1995.

[10] P. R. J. Saey, "Ultra-Low-Level Measurements of Argon , Krypton and Radioxenon for Treaty Verification Purposes," *ESARDA BULLETIN*, no. 36, pp. 42–56, 2007.

[11] D. Haas, J. L. Orrell, T. W. Bowyer, J. I. McIntyre, H. S. Miley, C. E. Aalseth, and J. C. Hayes, "The Science Case for 37Ar as a Monitor for Underground Nuclear Explosions," Tech. Rep. PNNL-19458, Pacific Northwest National Laboratory, 2010.

[12] C. Carrigan, R. Heinle, G. Hudson, J. Nitao, and J. Zucca, "Barometric Gas Transport Along Faults and Its Application to Nuclear Test-Ban Monitoring," Tech. Rep. UCRL-JC-127585, Lawrence Livermore National Laboratory, 1997.

[13] H. H. Loosli and H. Oeschger, "37Ar and 81Kr in the Atmosphere," *Earth and Planetary Science Letters*, vol. 7, pp. 67–71, 1969.

[14] H. H. Loosli, H. Oeschger, and W. Wiest, "Argon 37, Argon 39, and Krypton 81 in the Atmosphere and Tracer Studies Based on These Isotopes," *Journal of Geophysical Research*, vol. 75, no. 15, pp. 2895–2900, 1970.

[15] J. Matuszek, C. Paperiello, and C. Kunz, "Reactor Contributions to Atmospheric Noble Gas Radioactivity Levels," in *Noble Gases* (R. Stanley and A. A. Moghissi, eds.), pp. 360–364, 1975.

[16] S. Qaim, A. Rusheed, G. Stocklin, and Wolf, "37Ar Formation from Calcium in Fission Reactors," *International Journal of Applied Radiation and Isotopes*, vol. 28, pp. 585–589, 1977.

[17] H. H. Loosli, H. Oeschger, R. Studer, M. Wahlen, and W. Wiest, "Atmospheric Concentrations and Mixing of Argon-37," in *Noble Gases* (R. E. Stanley and A. A. Moghissi, eds.), pp. 24–39, 1975.

[18] Y. Yokoyama, J.-L. Reyss, and F. Guichard, "Production of Radionuclides by Cosmic Rays at Mountain Altitudes," *Earth and Planetary Science Letters*, no. 36, pp. 44–50, 1977.

[19] R. Riedmann and R. Purtschert, "Natural (37)Ar concentrations in soil air: implications for monitoring underground nuclear explosions.," *Environmental Science & Technology*, vol. 45, pp. 8656–64, Oct. 2011.

[20] C. R. Carrigan and Y. Sun, "Issues Involving The OSI Concept of Operation For Noble Gas Radionuclide Detection," Tech. Rep. LLNL-TR-467731, Lawrence Livermore National Laboratory, 2011.

[21] C. Anderson, G. Wheeler, and W. Watson, "Inner Bremsstrahlung Associated with K Capture in A37," *Physical Review*, vol. 90, no. 4, pp. 606–608, 1953.

[22] C. M. Egnatuk, J. Lowrey, S. R. Biegalski, T. Bowyer, D. Haas, J. Orrell, V. Woods, and M. Keillor, "Production of 37Ar in The University of Texas TRIGA reactor facility," *Journal of Radioanalytical and Nuclear Chemistry*, vol. 291, pp. 257–260, June 2011.

[23] C. Aalseth, A. Day, D. Haas, and E. Hoppe, "Measurement of 37Ar to support technology for On-site Inspection under the Comprehensive Nuclear-Test-Ban Treaty," *Nuclear Instruments and Methods in Physics Research Section A*, vol. 652, no. 1, pp. 58–61, 2011.

[24] H. Michael, R. Wolfle, and S. Qaim, "Production of 37Ar," *International Journal of Applied Radiation and Isotopes*, vol. 35, no. 8, pp. 813–815, 1984.

[25] L. A. Currie and R. M. Lindstrom, "The NBS Measurement System for Natural Argon-37," in *Noble Gases* (R. E. Stanley and A. A. Moghissi, eds.), pp. 40–57, 1975.

[26] C. Paperiello, "Internal Gas-Proportional Beta-Spectrometry for Measurement of Radioactive Noble Gases in Reactor Effluents," in *Noble Gases* (R. Stanley and A. A. Moghissi, eds.), pp. 239–248, 1975.

[27] B. Saraf, "Inner Bremsstrahlung Emitted in Electron Capture Decay of Ni59, A37, and Fe55," *Physical Review*, vol. 102, no. 3, pp. 466–473, 1956.

[28] W. Bambynek, H. Behrens, M. Chen, B. Crasemann, M. Fitzpatrick, K. Ledingham, H. Genz, M. Mutterer, and R. Intemann, "Orbital electron capture by the nucleus," *Reviews of Modern Physics*, vol. 49, pp. 77–221, Oct. 1977.

[29] J. Vanhaverbeke and N. Severijns, "Asymmetry of the Internal Bremsstrahlung of 37Ar," *Hyperfine Interactions*, vol. 43, pp. 373–378, 1988.

[30] V. Barsanov, A. Dzhanelidze, A. Zamyatina, S. Zlokazov, A. Korenkova, N. Kotelnikov, S. Markov, V. Selin, Z. Shakirov, D. Abdurashitov, E. Veretenkin, V. Gavrin, I. Mirmov, and V. Yantz, "A technology and facility for extraction, purification, and collection of 37Ar from calcium oxide," *Instruments and Experimental Techniques*, vol. 49, no. 4, pp. 454–460, 2006.

[31] T. San-Tsiang, H. Zah-Wei, R. Chastel, and L. Vigneron, "On the new fission processes of uranium nuclei," *Physical Review*, pp. 382–383, 1947.

[32] L. Rosen and A. Hudson, "Symmetrical Tripartition of U235 by Thermal Neutrons," *Physical Review*, vol. 78, no. 5, pp. 533–538, 1950.

[33] C. Weaver, E. Harward, and H. Peterson, "Tritium in the environment from nuclear powerplants.," *Public Health Reports*, vol. 84, no. 4, pp. 363–71, 1969.

[34] F. Luykx and G. Fraser, "Tritium releases from nuclear power plants and nuclear fuel reprocessing plants," *Radiation Protection Dosimetry*, vol. 16, no. 1-2, pp. 31–36, 1986.

[35] R. Stoenner and M. Hillman, "Search for Radiochemical Evidence for Ternary Fission of 235U by Thermal Neutrons," *Physical Review*, vol. 142, no. 3, 1966.

[36] G. Kugler and W. Clarke, "Mass-Spectrometric Search for Neon and Argon Isotopes in Ternary Fission of^{235} U," *Physical Review C*, vol. 3, no. 2, pp. 849 – 853, 1971.

[37] "Table of Nuclides." `http://atom.kaeri.re.kr/ton/nuc7.html`, 2013.

[38] L. Moral and A. F. Pacheco, "Algebraic approach to the radioactive decay equations," *American Journal of Physics*, vol. 71, no. 7, p. 684, 2003.

[39] C. Moler and C. Van Loan, "Nineteen Dubious Ways to Compute the Exponential of a Matrix, Twenty-Five Years Later," *SIAM Review*, vol. 45, pp. 3–49, Jan. 2003.

[40] S. M. Whitney, R. G. Downing, S. Biegalski, and D. S. O Kelly, "Advancement of light-element neutron depth profiling at the University of Texas," *Journal of Radioanalytical and Nuclear Chemistry*, vol. 276, pp. 257–261, Nov. 2007.

[41] S. M. Whitney, *Neutron Depth Profiling Benchmarking and Analysis of Applications to Lithium Ion Cell Electrode and Interfacial Studies Research*. Phd dissertation, University of Texas at Austin, 2008.

[42] M. Saglam, *Alpha Radiation Effects on Weapon Grade Plutonium Encapsulating Materials*. Phd dissertation, University of Texas at Austin, 2000.

[43] E. Alvarez, *Characterization of the University of Texas Nuclear Engineering Teaching Laboratory Beam Port 3 Texas Cold Neutron Source Prompt Gamma-Ray Activation Analysis Facility*. Ms thesis, University of Texas at Austin, 2005.

[44] L. Cao, *Development of a High Spatial Resolution Neutron Imaging System and Performance Evaluation*. Phd dissertation, University of Texas at Austin, 2007.

[45] O. Doron, *Development of a transport system for the copper source of the Texas Intense Positron Source facility*. Phd dissertation, University of Texas at Austin, 2004.

[46] J. Peterson and G. Ilas, "Calculation of Heating Values for the High Flux Isotope Reactor," in *PHYSOR 2012 - Advances in Reactor Physics*, (Knoxville, TN), 2012.

[47] M. Chadwick, M. Herman, P. Obložinský, M. Dunn, Y. Danon, A. Kahler, D. Smith, B. Pritychenko, G. Arbanas, R. Arcilla, R. Brewer, D. Brown, R. Capote, A. Carlson, Y. Cho, H. Derrien, K. Guber, G. Hale, S. Hoblit, S. Holloway, T. Johnson, T. Kawano, B. Kiedrowski, H. Kim, S. Kunieda, N. Larson, L. Leal, J. Lestone, R. Little, E. McCutchan, R. MacFarlane, M. MacInnes, C. Mattoon, R. McKnight, S. Mughabghab, G. Nobre, G. Palmiotti, A. Palumbo, M. Pigni, V. Pronyaev, R. Sayer, A. Sonzogni, N. Summers, P. Talou, I. Thompson, A. Trkov, R. Vogt, S. van der Marck, A. Wallner, M. White, D. Wiarda,

and P. Young, “ENDF/B-VII.1 Nuclear Data for Science and Technology: Cross Sections, Covariances, Fission Product Yields and Decay Data,” *Nuclear Data Sheets*, vol. 112, no. 12, pp. 2887–2996, 2011.

[48] A. Koning, R. Forrest, M. Kellett, R. Mills, H. Henriksson, and Y. Rugama, “The JEFF-3 . 1 Nuclear Data Library,” Tech. Rep. 6190, Organisation for Ecnomic Cooperation and Development: Nuclear Energy Agency, 2006.

[49] K. Shibata, T. Kawano, T. Nakagawa, O. Iwamoto, J.-i. Katakura, T. Fukahori, S. Chiba, A. Hasegawa, T. Murata, H. Matsunobu, T. Ohsawa, Y. Nakajima, T. Yoshida, A. Zukeran, M. Kawai, M. Baba, M. Ishikawa, T. Asami, T. Watanabe, Y. Watanabe, M. Igashira, N. Yamamuro, H. Kitazawa, N. Yamano, and H. Takano, “Japanese Evaluated Nuclear Data Library Version 3 Revision-3: JENDL-3.3,” *Journal of Nuclear Science and Technology*, vol. 39, no. 11, pp. 1125–1136, 2002.

[50] S. Zabrodskaya, A. Ignatyuk, V. Koscheev, V. Manokhin, M. Nikolaev, and V. Pronyaev, “Rosfond-russian national library of neutron data,” *Voprosy Atomnoj Nauki i Techniki, Seriya: Nuclear Constants*, vol. 1, p. 2, 2007.

[51] J. Colt, *Dissolved Gas Concentration in Water, Second Edition: Computation as Functions of Temperature, Salinity and Pressure*. Elsevier, 2012.

[52] R. Weiss, “The solubility of nitrogen, oxygen and argon in water and seawater,” *Deep Sea Research and Oceanographic Abstracts*, vol. 17, pp. 721–735, 1970.

[53] W. Aeschbach Hertig, “Interpretation of dissolved atmospheric noble gases in natural waters,” *Water Resources Research*, vol. 35, no. 9, pp. 2779–2792, 1999.

[54] R. C. Hamme and S. R. Emerson, "The solubility of neon, nitrogen and argon in distilled water and seawater," *Deep Sea Research Part I: Oceanographic Research Papers*, vol. 51, pp. 1517–1528, Nov. 2004.

[55] L. Merlivat and L. Memery, "Gas exchange across an air-water interface: Experimental results and modeling of bubble contribution to transfer," *Journal of Geophysical Research*, vol. 88, no. C1, p. 707, 1983.

[56] D. Himmelblau, "Diffusion of dissolved gases in liquids," *Chemical Reviews*, pp. 527–550, 1964.

[57] R. Draxler and G. Hess, "Description of the HYSPLIT 4 modeling system," Tech. Rep. August 2002, NOAA, Silver Spring, MD., 1997.

[58] C. M. Egnatuk, *Radioargon Production at The University of Texas at Austin*. Phd dissertation, University of Texas at Austin, 2012.

[59] S. Aghara, *Characterization of an In-Core Irradiator for Testing of Microelectronics in a Mixed Radiation Environment*. Phd dissertation, University of Texas at Austin, 2008.

[60] J. Graham, S. Landsberger, P. J. Ferreira, J. Ihlefeld, and G. Brennecka, "Neutron flux characterization techniques for radiation effects studies," *Journal of Radioanalytical and Nuclear Chemistry*, vol. 291, pp. 503–507, June 2011.

[61] J. Braisted, *Design and characterization of an irradiation facility with real-time monitoring*. Phd dissertation, University of Texas at Austin, 2008.

[62] D. Madland, "Total prompt energy release in the neutron-induced fission of 235U, 238U, and 239Pu," *Nuclear Physics A*, vol. 772, pp. 113–137, June 2006.

[63] R. Little, T. Kawano, G. Hale, M. Pigni, M. Herman, P. Obložinský, M. Williams, M. Dunn, G. Arbanas, D. Wiarda, R. McKnight, J. McKamy, and J. Felty, "Low-fidelity Covariance Project," *Nuclear Data Sheets*, vol. 109, pp. 2828–2833, Dec. 2008.

[64] D. F. R. Mildner and G. P. Lamaze, "Neutron Transmission of Single-Crystal Sapphire," *Journal of Applied Crystallography*, vol. 31, pp. 835–840, Dec. 1998.

[65] S. Merz, M. Djuricic, M. Villa, H. Böck, and G. Steinhauser, "Neutron flux measurements at the TRIGA reactor in Vienna for the prediction of the activation of the biological shield.," *Applied Radiation and Isotopes*, vol. 69, no. 11, pp. 1621–4, 2011.

[66] K. Hover, "Air Content and Unit Weight of Hardened Concrete," in *Significance of Tests and Properties of Concrete and Concrete-Making Materials* (P. Klieger and J. Lamond, eds.), no. 169, pp. 296–314, ASTM International, 1994.

[67] G. Steinhauser, M. Lechermann, A. Axelsson, H. Böck, A. Ringbom, P. R. J. Saey, C. Schlosser, and M. Villa, "Research reactors as sources of atmospheric radioxenon," *Journal of Radioanalytical and Nuclear Chemistry*, Sept. 2012.

[68] J. Sercombe, R. Vidal, C. Galle, and F. Adenot, "Experimental study of gas diffusion in cement paste," *Cement and Concrete Research*, vol. 37, no. 4, pp. 579–588, 2007.

[69] F. Fournier, J. E. Groetz, F. Jacob, J. M. Crolet, and H. Lettner, "Simulation of Radon Transport through Building Materials: Influence of the Water Content on Radon Exhalation Rate," *Transport in Porous Media*, vol. 59, no. 2, pp. 197–214, 2005.

[70] C. Cosma, F. Dancea, T. Jurcut, and D. Ristoiu, "Determination of 222Rn emanation fraction and diffusion coefficient in concrete using accumulation chambers and the influence of humidity and radium distribution.," *Applied Radiation and Isotopes*, vol. 54, no. 3, pp. 467–73, 2001.

[71] A. G. Fay and S. R. Biegalski, "Contributions to the 37Ar background by research reactor operations," *Journal of Radioanalytical and Nuclear Chemistry*, vol. 296, no. 1, pp. 273–277, 2013.

[72] "IAEA Research Reactor Database." `http://nucleus.iaea.org/RRDB/RR/ReactorSearch.aspx`, 2013.